Master's thesis

2020

Adrian Golten Eikevik

NTNU
Norwegian University of
Science and Technology
Faculty of Engineering
Department of Mechanical and Industrial Engineering

Adrian Golten Eikevik

Design and Optimization for Additive Manufacturing of Steering Head and Handlebar Bracket for Ducati Multistrada 1260 S

June 2020

NTNU
Norwegian University of
Science and Technology

NTNU
Norwegian University of
Science and Technology

NTNU
Norwegian University of
Science and Technology

Design and Optimization for Additive Manufacturing of Steering Head and Handlebar Bracket for Ducati Multistrada 1260 S

Adrian Golten Eikevik

Mechanical Engineering
Submission date: June 2020
Supervisor: Filippo Berto
Co-supervisor: Terje Rølvåg

Norwegian University of Science and Technology
Department of Mechanical and Industrial Engineering

Abstract

In this master's thesis, the steering arrangement for a Ducati Multistrada 1260S is further developed, focusing on additive manufacturing as the production method. This method has fewer geometric limitations than traditional manufacturing methods have. Optimization methods such as topology optimization have been used for that reason to detect smart designs. The steering arrangement currently consists of three main components, the *steering head,* which is the upper part of a triple tree clamp, the *handle holder lower,* which is the holder of the handlebar and *handlebar bracket upper,* which is the bracket that holds the handlebar down to the holder. In the new design, *steering head* and *handle holder lower* has become one part that in this report is called *steering head bracket* (SHB). This saves Ducati for bolts, washers, and sleeves. By using topology optimization, the total weight has been reduced by 36 %, from 1304 g to 830 g without losing noticeable stiffness. Where a deflection of 0.15 mm was previously achieved, there is now a deflection of 0.41 mm during maximum braking.

Along the way towards the new design, four different topology optimization software, as well as some CAD reconstruction methods, are evaluated. These software are Siemens NX Topology Optimization for Designers, SolidWorks Simulations, Fusion360 Generative Design, and Abaqus CAE Tosca. They are compared in several areas, both on optimization opportunities and time.

Sammendrag

I denne masteroppgaven videreutvikles styrekronen på en Ducati Multistrada 1260S, med fokus på additiv tilvirkning som produksjonsmetode. Denne metoden har langt mindre geometriske begrensninger som tradisjonelle tilvikningsmetoder har. Optimaliseringsmetoder som topologi optimalisering er av den grunn blitt anvendt for å oppdage smarte design. Styrekronen består i dag av tre hovedkomponenter, *steering head* som er den øvre delen av en trippel tre klemme, *handle holder lower* som er holderen til styret og *handlebar bracket upper* som er braketten som holder styret nedtil holderen. I det nye designet er *steering head* og *handle holder lower* blitt til èn del som i denne rapporten blir kalt *steering head bracket* (SHB). Dette sparer Ducati for bolter, skiver og hylser. Ved hjelp av topologi optimalisering har total vekten blitt redusert med 36%, fra 1304 g til 830 g uten for stor betydning på stivheten. Der man tidligere oppnådde en utbøyning på 0,15 mm har man nå en utbøyning på 0,41 mm under maksimal nedbremsning.

På veien mot det nye designet evalueres også fire forskjellige topologi optimaliseringsprogrammvarer samt noen metoder for rekonstruksjon av CAD. Disse programvarene er *Siemens NX Topology Optimization for Designers*, *SolidWorks Simulations, Fusion360 Generative Design* og *Abaqus CAE Tosca.* De blir sammenlignet på flere områder, både på optimaliseringsmuligheter og tidsbruk.

.

Preface

This master's thesis is written at Norwegian University of Science and Technology (NTNU) in the spring of 2020 as the answer to the subject TMM4960 *Produktutvikling og materialer, masteroppgave.* The project is given by the Department of Mechanical and Industrial Engineering with Professor Filippo Berto as supervisor and Professor Terje Rølvåg as co-supervisor.

The topic of the thesis is design and optimization for additive manufacturing parts for Ducati Multistrada 1260 S.

I would like to thank Prof. Berto and Prof. Rølvåg for knowledgeable guidance. I would also like to thank Ducati for providing us with this interesting and challenging task. Last but not least, I would like to thank Kjetil Ødegård and Per Kristian Garnes for professional conversations regarding topology optimization and FEA in NX Nastran.

Table of Contents

List of Figures x
List of Tables xii
Abbreviations xiii
1 Introduction 14
1.1 Background and Objectives 14
1.2 Steering arrangement 15
2 Theory 16
2.1 Structural Optimization 16
2.2 Topology Optimization 17
2.3 Generative Design 18
2.4 Additive manufacturing 18
2.5 Fatigue 26
3 Methods and Procedure 27
3.1 Steering Head Bracket (SHB) and Handlebar Bracket Upper (HBU) 27
3.2 Evaluation of Tools and Methods for Topology Optimization 27
3.3 Re-construction of CAD 32
3.4 Load Scenario 36
3.5 Fatigue 38
4 Results 39
4.1 Topology Optimization with different tools and methods 39
4.2 FEM Verification 43
4.3 Manufacturing Process 50
4.4 Final Design 51
5 Discussion and Conclusion 54
5.1 Tools and Methods 54
5.2 Steering Head and Handlebar Bracket Upper 55
5.3 Conclusion 56
References 58
Appendix 61

List of Figures

Figure 1.1 - Ducati Multistrada 1260 S 2019 (Ducati, 2019) 14
Figure 1.2 – Explode view of steering arrangement for Multistrada (Ducati, 2020b). 15
Figure 2.1 - Two-dimensional topology optimization. The box is to be filled to 50% by material. In the upper picture, we see the load case and boundary condition at the start. The result is shown in the second picture. 17
Figure 2.2 - Schematics of an LBM machine (left), and the three process steps iterated during the build (right)(Herzog et al., 2016). 19
Figure 2.3 - Schematics of an EBM machine, 1: electron gun, 2: lens system, 3: deflection lens, 4: powder cassettes with feedstock, 5: rake, 6: building component, 7: build table (Herzog et al., 2016) 19
Figure 2.4 - Schematics of an LMD set-up (Herzog et al., 2016) 20
Figure 2.5 - Common defects in the selective laser sintering process (Malekipour and El-Mounayri, 2018) 21
Figure 2.6 - Cost comparison of different AM materials 23
Figure 2.7 - (a) Concave radii. Titanium: (b) overhang 9 mm, (d) overhang 15 mm. Aluminum: (c) overhang of 9 mm, (e) overhang of 15 mm. 24
Figure 2.8 - (a) Convex radii and (b) overhang of 15 mm. Overhang of 9 mm: (c) titanium and (d) aluminum. 24
Figure 2.9 - Measured roughness of the full-circle at different positions, by Q. Han, H.G. Shwe Soe et.al 2018. 25
Figure 2.10 - Flowchart of optimization of orientation and support by F.Calignano. 26
Figure 3.1 - Optimization process for NX TOD 27
Figure 3.2 - Optimization process for SW 28
Figure 3.3 - Optimization process for Generative Design 29
Figure 3.4 - Optimization process for Abaqus Tosca 29
Figure 3.5 - Re-construction procedure of CAD in NX. From STL to modeling stage in *Realize shape* application to meshed FEM-model. 33
Figure 3.6 - Re-construction procedure of CAD in SolidWorks. From STL to modeling stage in *Mesh modeling* application to meshed FEM-model. 34
Figure 3.7 - Re-construction procedure of CAD with Abaqus optimized result in NX. From unsmoothed ODB-file in Abaqus to STL in NX to meshed FEM-model. 35
Figure 3.8 - Re-construction procedure of CAD with Abaqus optimized result in SolidWorks. From point cloud (XYZ-file) in MeshLab to graphics body in SolidWorks to meshed FEM-model. 36
Figure 3.9 - Lateral displacement. Picture from *Motorcycle Handling and Chassis Design* (Foale, 2006) 37
Figure 3.10 - Illustration to show which direction the loads point. Blue are bump loads, red are deceleration load, and green are acceleration. 38
Figure 4.1 - Set-up that is used in the TO 39
Figure 4.2 - Design space and result of optimization in NX TOD 40
Figure 4.3 - Design space and result of optimization in SW simulations 41
Figure 4.4 - Design space and result of optimization in Fusion360 41
Figure 4.5 - Design space and result of optimization in ABAQUS Tosca 42
Figure 4.6 - Key points in a diamond diagram to compare software tools 43
Figure 4.7 - FEA-1 set-up 44
Figure 4.8 - FEA-1 maximum stress 45
Figure 4.9 - FEA-1 average maximum stress 45
Figure 4.10 - FEA-1 displacement. Visually exaggerated by 10 %. 45
Figure 4.11 - FEA-2 set-up 46
Figure 4.12 - FEA-2 maximum stress (handlebar is hided) 46
Figure 4.13 - FEA-2 average stress in the HBU (handlebar is hided) 47
Figure 4.14 - FEA-2 average stress in SHB (handlebar is hided) 47
Figure 4.15 - FEA-2 displacement. Visually exaggerated by 0.5 % 47
Figure 4.16 - FEA-3 average stress 48
Figure 4.17 - FEA-3 displacement. Visually exaggerated 10 % 48
Figure 4.18 - FEA-4 set-up 49
Figure 4.19 - FEA-4 average stress 49
Figure 4.20 - FEA-4 displacement. Visually exaggerated 10 % 50
Figure 4.21 - Illustration of SHB in EOSINT M280 with support 51
Figure 4.22 - Original design. 52
Figure 4.23 - New design seen from the front. 52

Figure 4.24 - New design seen from the side. 52
Figure 4.25 - SHB and HBU seen from behind. 53
Figure 4.26 - SHB and HBU seen from the front. 53
Figure 0.1 - Staircase effect 62
Figure 0.2 - Close up picture of balling 62
Figure 0.3 – Defects, delamination and lack of fusion in AM (Milewski, 2017) 63
Figure 0.4 - Motorcycle under braking, from Motorcycle dynamics 64
Figure 0.5 - Front-wheel vertical acceleration 65
Figure 0.6 - Triple tree simulation 67
Figure 0.7 - Acceleration limited by wheelie, from motorcycle dynamics. 68
Figure 0.8 - Steering torque for a motorcycle in a turn 70
Figure 0.9 - NX TOD result and convergence diagram. 71
Figure 0.10 - Result NX TOD. The transition between the suspension clamp and struts are exposed. Hints of stresses in the transition between the headstock connection ring and struts. 72
Figure 0.11 - Result NX TOD. Maximum displacement in the suspension clamps. 72
Figure 0.12 – NX TOD. Solid properties check of the re-constructed CAD. 72
Figure 0.13 - NX TOD re-constructed model with 167 MPa legend limit 73
Figure 0.14 - NX TOD re-constructed model maximum stress. 73
Figure 0.15 - NX TOD re-constructed model convergence check medium mesh. 74
Figure 0.16 - NX TOD re-constructed model convergence check fine mesh. 74
Figure 0.17 - NX TOD re-constructed model average stress. 74
Figure 0.18 - NX TOD re-constructed model maximum displacement 75
Figure 0.19 - Fusion360 TO result 75
Figure 0.20 - Fusion360 Stress indication 76
Figure 0.21 - Fusion360. Solid properties check for the exported CAD. 76
Figure 0.22 - Fusion360 Stress on the exported CAD. 76
Figure 0.23 - Fusion 360 close up of stress 77
Figure 0.24 - Fusion360 average stress 77
Figure 0.25 - Fusion360 maximum displacement. 78
Figure 0.26 - Result from SW. Material missing between critical regions. 78
Figure 0.27 - Convergence diagram from Abaqus results 79
Figure 0.28 - Abaqus maximum stress re-constructed model. 79
Figure 0.29 - Abaqus close up maximum stress re-constructed model. 80
Figure 0.30 - Abaqus maximum displacement re-constructed model. 80
Figure 0.31 - Solid properties check of re-constructed model from Abaqus 80
Figure 0.32 - S-N curve for AlSi10Mg printed with EOSINT M-280. 83
Figure 0.33 - S-N curve in log-log plot 84
Figure 0.34 - A presumed stress history per 10 km. 85
Figure 0.35 - OEM FEA-1 set-up 86
Figure 0.36 - Result OEM FEA-1 87
Figure 0.37 - Displacement OEM FEA-1. Visually exaggerated 10 %. 87
Figure 0.38 - Result OEM FEA-3 88
Figure 0.39 - Displacement OEM FEA-3. Visually exaggerated 10 %. 88
Figure 0.40 - Result OEM FEA-4 89
Figure 0.41 - Displacement OEM FEA-4. Visually exaggerated 10 %. 89

List of Tables

Table 1 - Summary of pros and cons for AM (Bandyopadhyay and Bose, 2015). 18
Table 2 - Common AM alloys and application (Milewski, 2017) 21
Table 3 - Comparing LBM, LMD, and EBM from Michael Schmidt's articles (Schmidt et al., 2017). 22
Table 4 - Cost comparison of AM material for 403 cm3 (AMPOWER, 2019) 22
Table 5 - Design constraints available in NX TOD 27
Table 6 - Manufacturing constraints available in SW 28
Table 7 - Manufacturing constraints available in Fusion360 29
Table 8 - Geometric restriction available in Abaqus Tosca 30
Table 9 - Comparing the different topology optimization software 30
Table 10 - Loads utilized in TO, FEM verifications and fatigue calculations 37
Table 11 - Material properties for AlSi10Mg 39
Table 12 - Material properties for AlSi10Mg in Fusion360 39
Table 13 - Description of different Finite Element Analysis 43
Table 14 - Weight comparing OEM and new design 51
Table 15 - Values that are crucial for maximum deceleration and acceleration 65
Table 16 - Values for the tensile load calculation 69
Table 17 - Load caused by accelerations and decelerations from 10 to 100 % 82
Table 18 - Stresses in the transition corner between the headstock ring and the struts during acceleration and deceleration. Positive stress for tension and negative stress for compression. 82
Table 19 - Values from S-N curve 83
Table 20 – Summary table of required values for Palmgren-Miner rule 85

Abbreviations

AM	Additive Manufacturing
CAE	Computer-Aided Engineering
CAD	Computer-Aided Design
EBM	Electron Beam Melting
FEA	Finite Element Analysis
FEM	Finite Element Method
HBU	Handlebar Bracket Upper
HHL	Handle Holder Lower
LMD	Laser Metal Deposition LMD
NTNU	Norwegian University of Science and Technology
NX TOD	NX Topology Optimization for Designers
OEM	Original Equipment Manufacturer
RBE2	Rigid Body Element 2
SHB	Steering Head Bracket
STL	Stereolithography
SW	SolidWorks
TO	Topology Optimization
UTS	Ultimate Tensile Strength

1 Introduction

In this master's thesis, a new innovative and optimized solution for the Ducati Multistrada steering arrangement has been explored. Different tools and methods for optimizing and re-construction of the model have been compared and evaluated. Figure 1.1 is obtained from Ducati's webpage (Ducati, 2019) and shows the Multistrada.

Figure 1.1 - Ducati Multistrada 1260 S 2019 (Ducati, 2019)

1.1 Background and Objectives

Ducati wants to see how the performance and weight of the steering arrangement could be if it were to be produced with more advanced technology such as additive manufacturing (AM). Traditional manufacturing methods have certain limits that AM does not have. To gain the advantage of this, the steering arrangement could have high geometrical complexity. When the geometrical complexity is not an obstacle for manufacturing, the use of intelligent optimization methods such as topology optimization (TO) can be used. More benefits of using AM for the production method are discussed in chapter 2.4

Tasks given from Ducati:

1. Evaluate and select tools and methods for topology optimization, e.g. weight reduction without compromising the strength requirements.

2. Identify load cases, constraints, weight, and stiffness targets for the steering arrangement.

3. Study the selected software tool and methods for steering arrangement optimization based on outputs from tasks 1 and 2.

4. Optimize the steering arrangement and benchmark the new design versus the original OEM design.

5. Reverse engineer the optimized design solution (create a CAD model).

6. Mesh and evaluate the structural performance and fatigue of the final CAD design.

Based on this, it has been established two primary goals for this thesis.

- Evaluate tool for topology optimization.
- Develop an additive manufacturing compatible lightweight steering arrangement that meets the strength requirements.

1.2 Steering arrangement

The Multistrada uses a triple tree steering arrangement with upside-down telescopic forks. The forks consist of hydraulic shock absorbers with internal coil spring to give the optimal steering and driving qualifications (Bhanage et al., 2015). With an upside-down fork, the inner fork tube (stanchion) is connected to the front wheel axle, and the outer fork tube (slider) is connected to the triple tree clamps. The outer fork tube is just referred to as suspension fork in this thesis.

Figure 1.2 from *Bike Parts Ducati* (Ducati, 2020b) shows an exploded view of the steering arrangement with its associated parts. This arrangement consists of six components: handlebar, handlebar bracket upper (nr.17 in Figure 1.2), holder handle lower (nr.14), steering head (nr.18), steering head base (nr.3) and steering stem (nr.3). The steering stem is rigidly connected to the steering head base. The suspensions are clamped in both the steering head base and the steering head. The steering stem is attached to the headstock[1] via steering head bearings, which allow the triple tree to move and steer the motorcycle. This arrangement is known to have low inertia around the steering head axis (Cossalter, 2006b).

The handlebar bracket is connected to the steering head with two bolts (nr.15). The handlebar bracket consists of holder handle lower (HHL)(nr.14) and handlebar bracket upper (HBU)(nr.17).

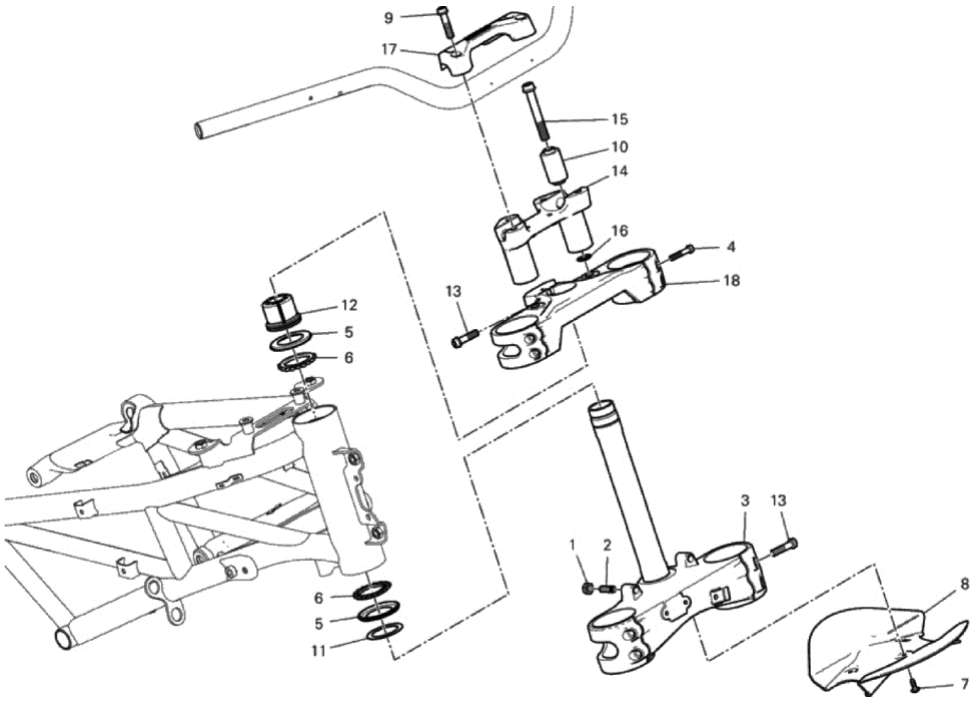

Figure 1.2 – Explode view of steering arrangement for Multistrada (Ducati, 2020b).

In this master's thesis, it has been examined the possibility of creating one single part consisting of HHL and steering head. This part will from here on be called *Steering Head Bracket* (SHB) or just referred to as the new design.

The middle hole on the steering head has been called headstock connection hole for the original design and headstock connection ring for the new design. The two clamps on the steering head are called suspension clamps, and where the handlebar lie is called the handlebar holder.

[1] The interface in frame

2 Theory

To better understand the work done in this master thesis, it is essential to have some knowledge about the methods and technology used to design and produce the SHB. Some underlying theory of structural optimization, generative design, AM, and fatigue is therefore presented in this chapter. The subsection structural optimization and some parts of additive manufacturing are obtained from the pre-study done autumn 2019.

2.1 Structural Optimization

Structural optimization can be split into three different optimization methods, sizing, shape, and topology optimization, depending on the geometric feature. All these methods are mathematical methods to find the optimal solutions, either thickness, form, or connectivity of nodes (13).

Christensen, Klarbring and Gladwell describe structural optimization as a function f(x,y) as shown in equation eq. (1) (Christensen et al., 2008).

Objective function (f): This is the function that classifies designs. Function f returns a number that tells how good the design is. It often measures displacement in a certain direction, weight, stress, or even cost of production.

Design variable (x): x is the variable that describes the design. When it represents a geometry, it could be the thickness of a sheet, area of a bar, or even interpolation of shape. It could also be a choice of material. This variable can be changed during optimization.

State variable (y): y is the variable that represents the response of the structure. This response could be displacement, stress, strain, or force.

A general structural optimization takes this form:

$$SO = \begin{cases} minimize\ f\ (x, y)\ with\ respect\ to\ x\ and\ y \\ subject\ to \begin{cases} behavioral\ constraints\ on\ y \\ design\ constraints\ on\ x \\ equilibrium\ constraint. \end{cases} \end{cases} \tag{1}$$

In eq. (1) there are three types of constraints. *Behavioral constraints* on the state variable y, which is a function g(y) that represents, e.g., displacement in a particular direction. Often these constraints are written g(y) ≤ 0. This state function can also be represented by a displacement vector g(u(x)).

Design constraints on the design variable x. Behavioral constraints and design constraints can be combined. *Equilibrium constraints* in discrete linear problem looks like

$$K(x)u = F(x) \tag{2}$$

where *K(x)* is the stiffness matrix of the structure. The displacement vector is *u*. And the force vector is *F*(*x*).

If we isolate u on left-hand side equation (2) can be rewritten to

$$u = u(x) = K(x)^{-1}F(x) \tag{3}$$

This results in the removal of the equilibrium constraint from eq. (1) and we have a so-called nested formulation as in eq.(4).

$$SO_{nf} = \begin{cases} minimize\ f\ (x, u(x))\ with\ respect\ to\ x\ and\ u(x) \\ subject\ to\ g(x, u(x)) \leq 0 \end{cases} \tag{4}$$

Multiple criteria or multi objectives are when a problem has several objective functions. This can be formulated like

$$minimize\ f_1(x, y), f_2(x, y), \ldots, f_n(x, y) \tag{5}$$

n is the number of objective functions. The constraints are the same as in eq. (1).

The objective can be to minimize the strain energy (U), also called compliance. The strain energy is given by equation

$$U = \frac{1}{2} V \sigma \varepsilon \tag{6}$$

where V is the volume of the object, σ is the stress, and ε is the strain.

When using minimize strain energy as an objective function, it also maximizes the structural stiffness. Combination of strain energy as the objective function and volume or weight fraction as the constraint is common.

2.2 Topology Optimization

Topology optimization finds the optimal layout of a solid structure, with determinations of features such as shape, number, and location of holes. Such optimal Lay-out could be minimum weight/volume or maximum stiffness. The only known parameters are the applied load, boundary condition, the original volume, and the design restriction you may have. An example is given in Figure 2.1.

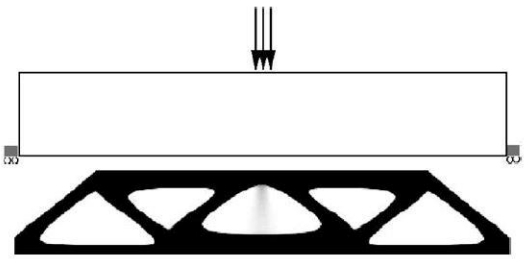

Figure 2.1 - Two-dimensional topology optimization. The box is to be filled to 50% by material. In the upper picture, we see the load case and boundary condition at the start. The result is shown in the second picture.

To topology optimize, we start with a part like the box in Figure 2.1, this part contains a design space and a non-design space. It is from the design space material is being removed until a final shape is reached during optimization. It is not favorable to apply loads and support directly on a design space, as this often leads to incorrect results. Non-design space is the area of the model that is not favorable to remove material from. Typical non-design space could be constrained areas and load areas.

2.3 Generative Design

Generative design uses a powerful artificial algorithm to generate thousands of designs in a short amount of time. Every design iterations structure is tested, and the generative design is learning from each step. It applies changes in all steps, and then it part by part reaches the optimal solution (Matthew, 2017).

2.4 Additive manufacturing

In contrast to machining (subtractive manufacturing), and forging (formative manufacturing), AM is a technology where 3D designs can be produced directly from a CAD file without any part-specific tools or dies. The CAD model is being divided into thin slices of cross-section profiles. These cross-sections are being traced and filled or partly filled by a laser beam, electron beam, extrusion nozzle, or jetting nozzle. This is done by adding layers in the X-Y plane, and then multiple layers are built on top of these layers generating the third dimension (Bandyopadhyay and Bose, 2015).

At the start of AM, most of these technologies made only polymeric objects only suitable for rapid prototyping and visualization of the model. Later it becomes possible to 3D print ceramics and metals parts that had much greater strength, and this resulted in end-usable parts directly from the printer (Bandyopadhyay and Bose, 2015).

AM allows you to produce optimized products with geometries that were too expensive or impossible to produce with traditional manufacturing methods. It is possible to redesign several components and make them into one single part. This reduces complexity and the final assembly time. AM makes it easier to create optimum strength-to-weight ratio while minimizing material volume. It reduces material waste in production, which leads to a reduction in cost and energy (Huang et al., 2016). With the design freedom AM gives you, it is possible to achieve intelligent design based on topology optimization methods. Table 1 shows the pros and cons of AM

Table 1 - Summary of pros and cons for AM (Bandyopadhyay and Bose, 2015).

Pros	*Cons*
Design freedom: AM can make essentially any geometry with no restriction	Surface finish: Post-processing is needed for optimal surface finish
No tooling: AM can make parts from start to finish with no other tooling required	Slower build rates for high volume manufacturing
Save material: Due to near net shape processing, it creates less waste than machining	High printer cost: Large capital investment is needed for high-end printers
Versatility: Easy to change design and complexity	Material and size restrictions: Limited versatility among different 3D printers makes them material-specific and has a limited build volume
Part optimization: Minimal design restriction means parts can be made lighter and stronger	

For metal AM, the most common methods are Laser Beam Melting (LBM), Electron Beam Melting (EBM), and Laser Metal Deposition (LMD). LBM is also known as Selective Laser Melting (SLM), Direct Metal Laser Sintering (DMLS), Laser Metal Fusion (LMF), or industrial 3D printing. LMD also has several know synonyms, such as Direct Metal Deposition (DMD) and Laser Engineered Net Shaping (LENS). These methods have different names because of the different machine manufacturers (Herzog et al., 2016).

Both LBM and EBM are powder bed-based processes, which means that metal powder is spread in thin layers across the work area. Figure 2.2 shows a sketch of how a typical LBM system could be. EBM systems are shown in Figure 2.3. For LBM the layer thickness is typical 20 μm – 100 μm and for EBM it is 50 μm – 200 μm. Then for LBM, it is used a laser beam to melt the powder, and an electron beam is used for the same purpose

for EBM. After a layer is melted, the bed is lowered. Another powder layer is applied, and the process repeat, layer by layer the model is being created see Figure 2.2 LBM Process (Herzog et al., 2016).

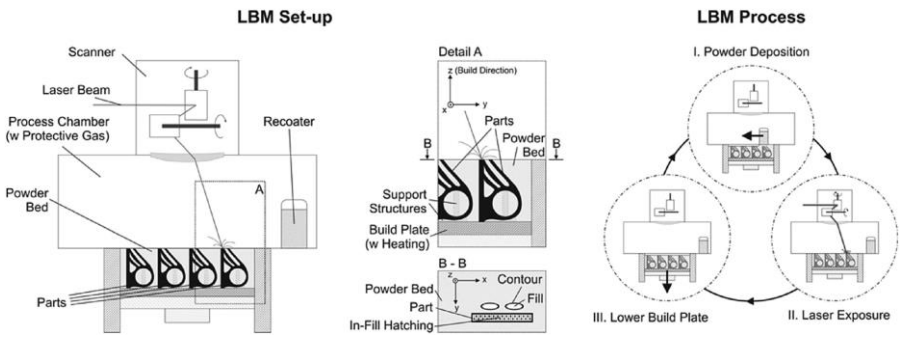

Figure 2.2 - Schematics of an LBM machine (left), and the three process steps iterated during the build (right)(Herzog et al., 2016).

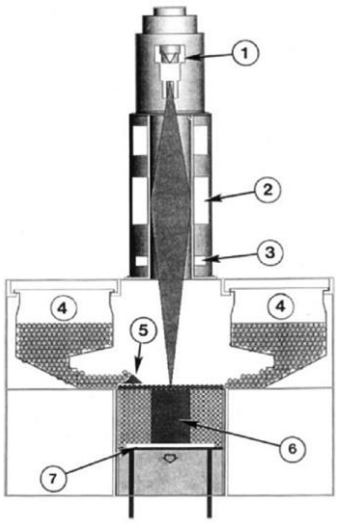

Figure 2.3 - Schematics of an EBM machine, 1: electron gun, 2: lens system, 3: deflection lens, 4: powder cassettes with feedstock, 5: rake, 6: building component, 7: build table (Herzog et al., 2016).

LMD uses another technology to build the model. By melting a surface and simultaneously applying the powder, the model is build up bit by bit. In some systems, the part is being moved under a stationary deposition head, and in other systems, the deposition head is repositioned by a 5-axis Cartesian gantry system or a robotic arm (Herzog et al., 2016). Figure 2.4 shows how a typical LMD set-up could be.

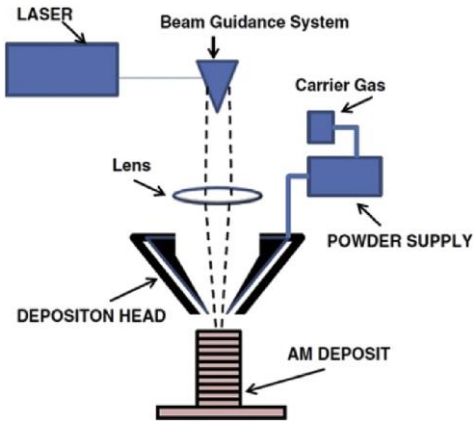

Figure 2.4 - Schematics of an LMD set-up (Herzog et al., 2016)

Materials in Additive Manufacturing

Today it is possible to 3D-print many different metals. Table 2 shows the common AM alloys and applications. There are several types of metallic material usable for AM. The most common are steel, aluminum alloys, titanium alloys, nickel-based superalloys, and cobalt chrome. These come in a metal powder that has been pulverized. Table 2 from Milewski, 2017 (Milewski, 2017) shows applications for these materials.

Aluminum, Stainless steel and Titanium are the most common alloy in the automotive industry.

Steel

The most common steel used in LBM methods are austenitic stainless steel, maraging steel, and precipitation hardenable stainless steel. For EBM, the most used steel is tool steel and austenitic stainless steel 316L (Herzog et al., 2016).

Aluminum

Aluminum is very easy to machine, and the cost of aluminum parts are cheap compared with other material such as Titanium. Many aluminum alloys are known to be hardly weldable. The number of different available aluminum alloys is still somewhat limited. Most commonly aluminum alloys are AlSi10Mg and the eutectic ALSi12. LBM and AlSi10Mg is to date the most common combination (Herzog et al., 2016).

Titanium

Because of titanium's high cost of machining and high performance, the interest regarding AM has been significant (Herzog et al., 2016). Most commonly titanium alloy used is Ti-6Al-4V. It is the most tested and explored titanium alloy with desirable properties, such as low density, ductility, and oxidation resistance (Uhlmann et al., 2015).

Other Metallic Materials

For other metallic materials, nickel-based superalloys such as Inconel 625 and Inconel 718 are used in LBM and EBM. Cobalt Chrome is used for biomedical applications (Herzog et al., 2016).

Table 2 - Common AM alloys and application (Milewski, 2017)

	Aluminum	*Maraging steel*	*Stainless steel*	*Titanium*	*Cobalt Chrome*	*Nickel-based superalloy*	*Precious metals*
Aerospace	X		X	X	X	X	
Medical			X	X	X		X
Energy, oil, and gas			X				
Automotive	X		X	X			
Marine			X	X		X	
Machinability and weldability	X		X	X		X	
Corrosion resistance			X	X	X	X	
High temperature			X	X		X	
Tools and molds		X	X				
Consumer products	X		X				X

Defects in Powder Bed Fusion AM

According to Malekipour and El-Mounayri (Malekipour and El-Mounayri, 2018), there are four categories for defects in LBM and EBM, geometry and dimension, surface quality, microstructure, mechanical properties, see Figure 2.5. All these defects are essential to be aware of. They are briefly explained in Appendix A . Defects for LMD are not presented.

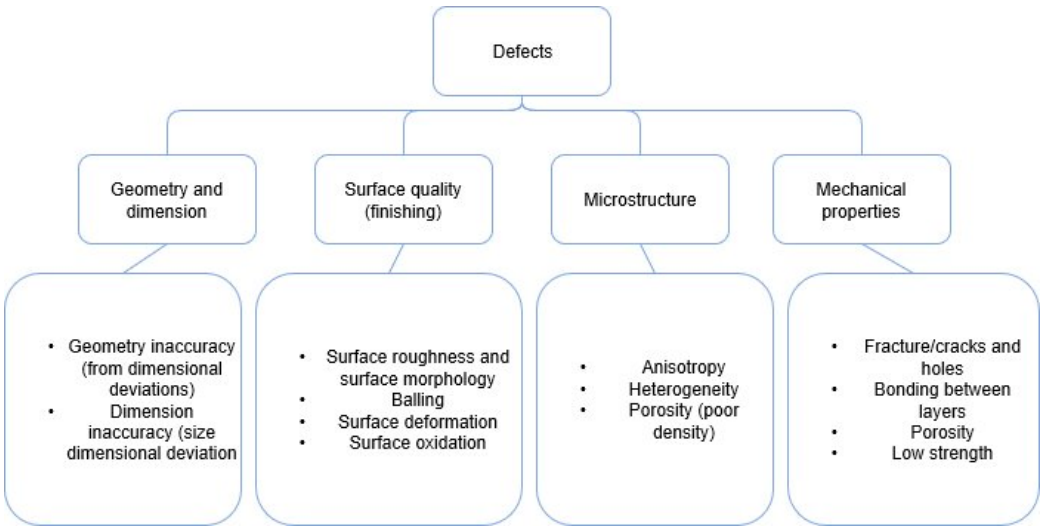

Figure 2.5 - Common defects in the selective laser sintering process (Malekipour and El-Mounayri, 2018)

2.4.1 Material and Additive Manufacturing Method

The correct combination of material and AM method is essential for the result when it comes to cost, performance, and look. For Ducati, these are all high-ranged factors.

In this subsection, cost and comparing of material and method are done. In Table 3 (Schmidt et al., 2017), LBM, LMD, and EBM are compared. Inconel is one of the materials compared in this table, but that is not a considered material for the SHB.

Table 3 - Comparing LBM, LMD, and EBM from Michael Schmidt's articles (Schmidt et al., 2017).

Process	LBM			LMD			EBM		
Energy source	Fiber laser			Fiber laser			Electro gun		
Resolution	Very high			Low			High		
Material providing mechanism	Powder bed			Powder nozzle			Powder bed		
Atmosphere	Inert gas			Inert gas supplied by nozzle			Vacuum		
Support structure requirement	Yes			No (5-axis motion)			Yes (less)		
Common materials	316L, 1.2709, AlSi10Mg, IN718, Ti6Al4V, Al, Ti			316L, H13, IN718, Ni-based alloys, Ti6Al4V			TiAl, Co-Cr-Mo, Fe, H13, IN718, Ti6Al4V		
Material manufactured	IN718	Ti6Al4V	316L	IN718	Ti6Al4V	316L	IN718	Ti6Al4V	CoCrMo
UTS [MPa]	1400	1250	740	828	1163	640	1108	1200	1450
Yield strength [MPa]	1180	1125	580	473	1105	473	869	1150	510
Elongation to failure in %	20,4	6	49,5	28	4	36	22,1	25	3,6

It is desirable to use a corrosion-resistant, light, and strong material for the SHB. The cost is also an important factor. Titanium, Stainless Steel, and Aluminum are good candidates, and these are to be considered.

Prices:

All prices are gathered from AM-POWER and may differ from other suppliers. These prices are therefore only used as a guideline.

Increasing volume means increasing of machine time and increasing of metal powder. Figure 2.6 shows how the price of different materials will decrease with a bigger volume (Insights, 2017). Parts that accommodate as much as possible of the 3D-printing machine are cheaper to print when we look at the cost per volume.

To compare prices of different AM methods, AM-POWER's estimating calculator has been used (AMPOWER, 2019). Select a material and volume of the part, and then it estimates the inhouse manufacturing cost. This is only for guidance. The original volume of the HHL and steering head are 403 cm^3. Table 4 shows the cost range of different materials. It shows maximum and minimum prices, and that is because of the support. Some parts need more support than others.

Table 4 - Cost comparison of AM material for 403 cm3 (AMPOWER, 2019)

Material	*Method*	*Cost range in €*		
		Minimum	*Maximum*	*Mean*
AlSi10Mg	LBM	1014.12	1415.12	1214.62
Ti-6Al-4V	LBM	2154.00	2605.00	2379.5
Ti-6Al-4V	EBM	1332.57	1432.57	1382.57
316 L	LBM	1521.90	1922.90	1722.40

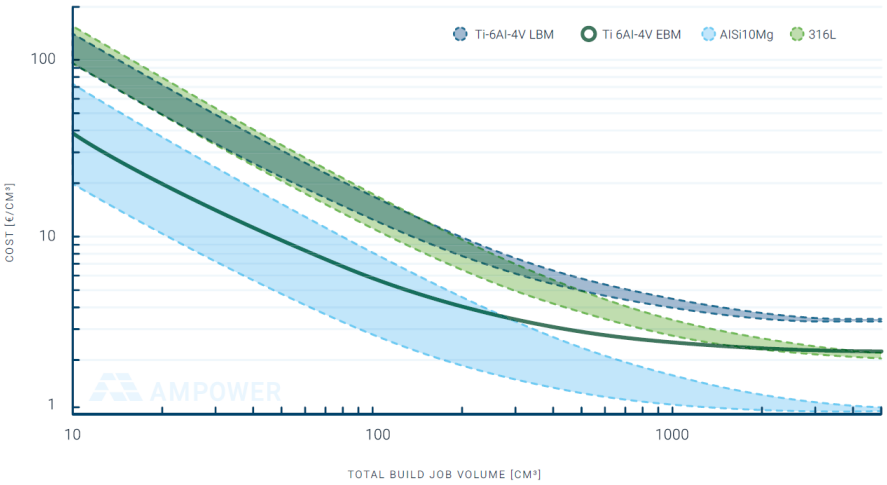

Figure 2.6 - Cost comparison of different AM materials

On the original design, it is used aluminum. It is a good reason to continue with this material for a better comparison basis. In the cost check, AlSi10Mg is the cheapest material with LBM method. Both Titanium and 316 L is more expensive than Aluminum.

LDM is not commonly used with Aluminum, and the finished parts with this method do have a low resolution. It is a method of growth, but not favorable in this situation. EBM does not have an as high resolution as LBM, and the mechanical properties are not that great either. AM-POWER only offered EBM for Ti-6Al-4V, so the price difference is unknown.

LBM method is a well-tested and established method for AM, and in the comparison table, we see that the mechanical properties are the greatest. The resolution is very high, and that is important for TO parts.

The material to use will be AlSi10Mg with LBM as the manufacturing method.

2.4.2 Design for Additive Manufacturing

According to Hallgren and Pejryd (Hällgren et al., 2016), there are two different ways to design for AM. That is process-driven and designer-driven. Process-driven design is when the part itself is in focus. The performance of the part or the time it takes to produce it is the primary concern. With the designer-driven process, the engineer's knowledge of manufacturing capabilities are what makes the decisions. The TO step of this thesis is mainly process-driven design but also designer-driven when printing direction is decided. A combination of the two design methods is important to minimize the cost and maximize the performance.

Even if the AM method provides opportunities for various new and innovative designs, it still has some boundary constraints that need to be considered. It is known that for LBM, angles greater than 45° is self-supporting, and angles smaller needs support (Vandenbroucke and Kruth, 2007). Today it is possible to print 30° without support, and it still does not collapse, but the surface roughness is high, and it will have distortions in the flatness of the bottom face (Calignano, 2014).

Here are some findings from F.Calignano (Calignano, 2014) on concave and convex radii:

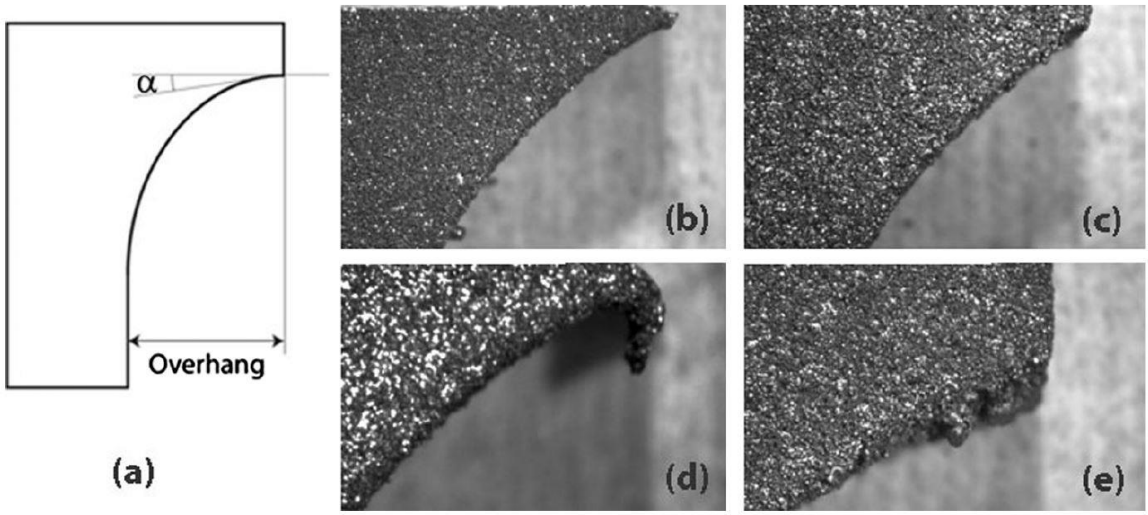

Figure 2.7 - (a) Concave radii. Titanium: (b) overhang 9 mm, (d) overhang 15 mm. Aluminum: (c) overhang of 9 mm, (e) overhang of 15 mm.

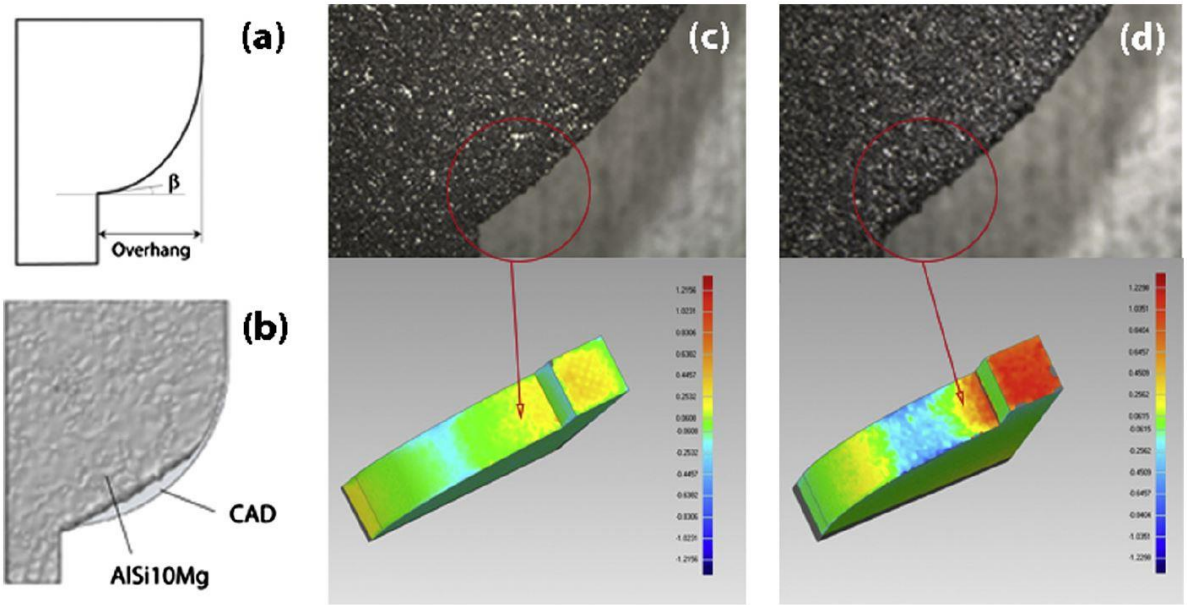

Figure 2.8 - (a) Convex radii and (b) overhang of 15 mm. Overhang of 9 mm: (c) titanium and (d) aluminum.

In Figure 2.7 (a), there is a tangent angle α, this decrease to 0° as the printing goes. Closer to 0° the warping distortion increase. By increasing the α-angle, the curve was improved. It is also shown that aluminum (e) does not collapse like titanium (d) when the overhang is at 15 mm.

Figure 2.8 shows the convex situation. The lowest region in the convex is most exposed to warping. When the β-angle (a) is lower than 40°, the accuracy for aluminum is poor. The shape of the model is not how the original CAD was (b). The maximum deviation from the model to the CAD for aluminum is 1.23 mm (d), and for titanium, it was 0.9 mm.

This shows that printing with some overhang is manageable, but the roughness must then be considered. In *Manufacturability of AlSi10Mg overhang structures fabricated by laser powder bed fusion,* authored by Han Q et al. (Han et al., 2018), the surface roughness is measured over an increased degree of overhang. The result is shown in Figure 2.9. From region III and higher, the surface roughness exhibited a significant increase. This is a result of the staircase effect, which again results in dross defects. In that article, they checked the displacement caused by the dross effect on circles with diameter from 10 mm to 30 mm with and without part support. The

part support was built inside the circle to support the overhang. With increasing the diameter, the dross effect tends to be more present on the part without support, this is not so noticeable for the part with support. No dross effect was found in areas with overhang angles smaller than 45°. The displacement for the 10 mm circle was 0.11 mm for the part without support and 0.10 mm with support. For the circle with a 30 mm diameter, this displacement was 0.28 mm without support and 0.11 mm with support.

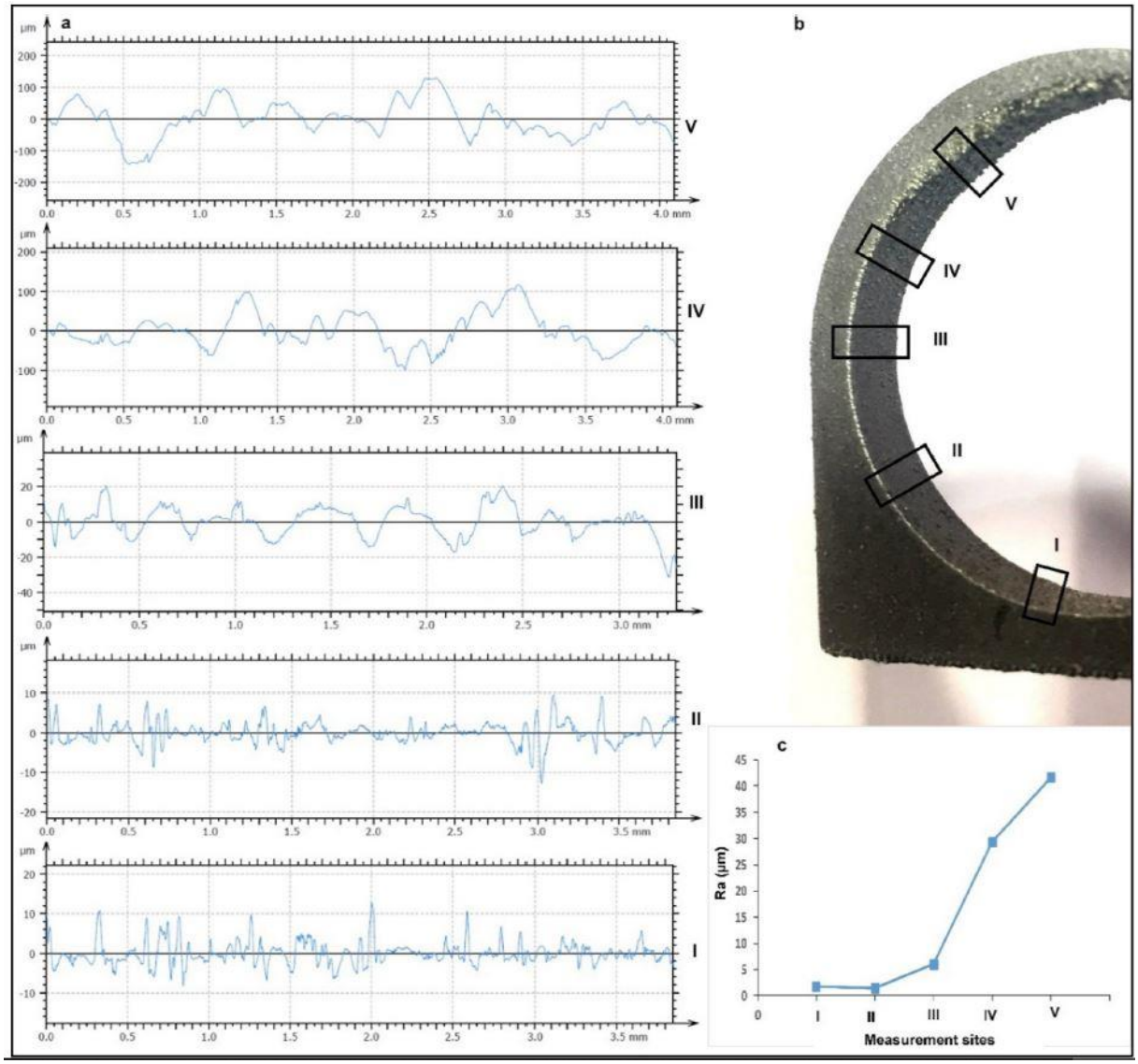

Figure 2.9 - Measured roughness of the full-circle at different positions, by Q. Han, H.G. Shwe Soe et.al 2018

F.Calignano presented a flowchart in his article (Calignano, 2014) that is useful when optimizing the orientation and support for the part that is going to be 3D printed. This flowchart is shown in Figure 2.10.

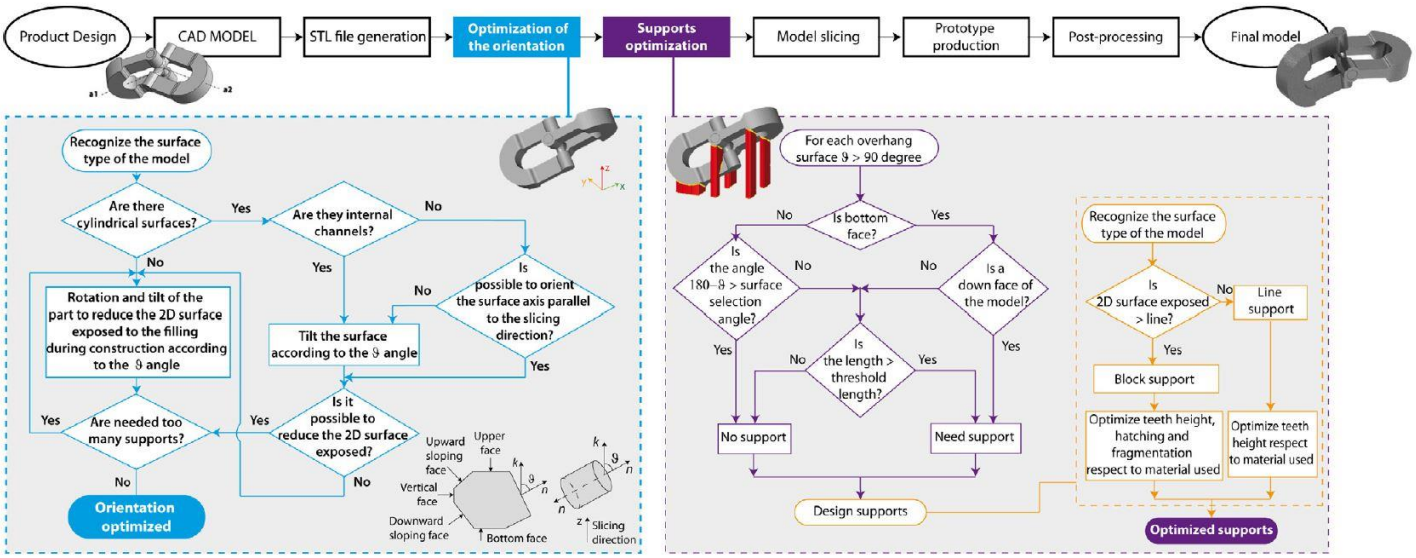

Figure 2.10 - Flowchart of optimization of orientation and support by F.Calignano.

Reducing the amount of support is important because the supports deforms the surface area and makes the printing time and cost to go up (Calignano, 2014). By having this, the surface roughness caused by overhang, and optimizing the orientations and support in mind when designing, the result will be improved.

2.5 Fatigue

Fatigue is a failure or damage that is caused by cyclic loading and is a well-discussed subject in material science. In engineering design, fatigue failure is a major concern and a common cause of fracture (Downling, 2012). Even stresses below the ultimate tensile strength (UTS), that are repeatedly experienced are enough to make the component to fail. High cycle fatigue is when the number of load repetitions are large, millions. Low cycle fatigue is when the number of load repetitions are small, tens, hundreds, or thousands (Downling, 2012).

Microscopic damage accumulates with frequent cyclic into a crack that can cause the component to fail (Downling, 2012). For material with no porosity or no surface defect, the crack propagates from dislocation gathering and growth toward the surface until fracture (DebRoy et al., 2018).

For AM, there are internal defects and surface defects that acts like stress concentrations, and this significantly reduces the number of cycles before fracture. Parameters such as powder depositions, pits, cracks, and staircase effect can cause surface defects (Malekipour and El-Mounayri, 2018). The most common internal defects are porosity and lack of fusion (DebRoy et al., 2018). In Appendix A , defects for AM are described.

The fine microstructure, high hardness, and poor ductility of AM parts are results of rapid cooling in the build process. With heat treatment, the microstructure of the material is altered, the ductility and the fatigue performance are significantly improved (Maskery et al., 2015). According to the authors in that article, they claim that the fatigue strength was increased from 85 MPa to 134 MPa at 10^6 cycles. Another post-process that improves the fatigue strength is sandblasting and shot peeing (Bagherifard et al., 2018).

3 Methods and Procedure

In this chapter, the different TO tools are described, evaluated, and compared. The load scenarios that SHB and HBU are exposed to are defined and the fatigue calculation process is described.

3.1 Steering Head Bracket (SHB) and Handlebar Bracket Upper (HBU)

The SHB is as described earlier, the part that consists of the steering head and HHL. This part is to be 3D-printed in AlSi10Mg in an EOSINT M-280 machine. HBU will be machined in Aluminum 6061-T6. In Appendix F, the material datasheet for both AlSi10Mg associated with EOSINT M-280 and Aluminum 6061-T6 can be found.

3.2 Evaluation of Tools and Methods for Topology Optimization

In this subsection, some of the TO tools available at NTNU will be briefly described and evaluated. These tools are NX Topology Optimization for Designers (NX TOD), SolidWorks simulation (SW), Fusion360 Generative Design, and Abaqus Tosca Structure.

3.2.1 Siemens NX

In NX, there are two solvers for TO, NX Topology Optimization for Designers (NX TOD), and NX Nastran Optimization SOL200. The last one is not evaluated in this thesis. NX TOD is not as complicated and advanced as the Nastran solver SOL200.

The optimization process for NX TOD is shown in Figure 3.1. From Manage bodies, most of the design criteria are defined, such as; design space, optimization features, keep out/in zones, loads, and constraints. With several different design constraints (listed in Table 5), it is possible to steer the optimization in the desired direction. AlSi10Mg is not an option in NX TOD, the material must be manually created. NX TOD does not operate with mesh and elements. In order to select the global resolution (minimum geometry size), it is a tab to slide, or it could be filled out manually.

A significant benefit with NX is that CAD, TO, reversed engineering, and FE-analysis can be done in the same software. This makes it smoother since you do not have to go from program to program. It recognizes sketches and features, which makes the operations much more time effective.

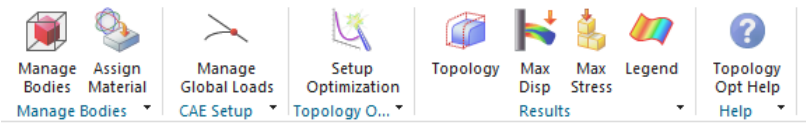

Figure 3.1 - Optimization process for NX TOD

Table 5 - Design constraints available in NX TOD

Design Constraints
Void-Fill
Material Spreading
Extrude Along a Vector
Overhang Prevention
Draft
Planar Symmetry
Rotational Symmetry
Self-Support

3.2.2 SolidWorks

SolidWorks Simulation add-in offers several solvers, including *Topology Study*. Figure 3.2 shows the optimization process for SW. It is straightforwardly and easy to set-up the optimization. Choose material from SW material library or create a material with desired specifications. AlSi10Mg is not an option, but a comparable material has been created and used. Remote loads are possible to use, which makes it easy to set up moments. Hex mesh is not possible, but tetrahedron four and ten are options. SW is caching during the optimization and this allows it to fill up free space on the computer. Therefore, it is crucial to have much free space before starting the optimization. Some manufacturing constraints are possible and are helpful when you want to steer the optimization in a more desired direction. These are listed in Table 6.

Before generating the STL-file, the part needs to be smoothed. Mesh modeling is an accurate CAD re-construction tool, especially when the STL-file is generated in SW, as the modeling commands recognize curves, lines, and surfaces.

In the same way as NX, it is possible to do all operations in SW. The results from the TO is not that trustworthy (this is more discussed in Appendix C) and are challenging to get right. The CAE-environment is not as advanced and opportunity-rich as NX Nastran.

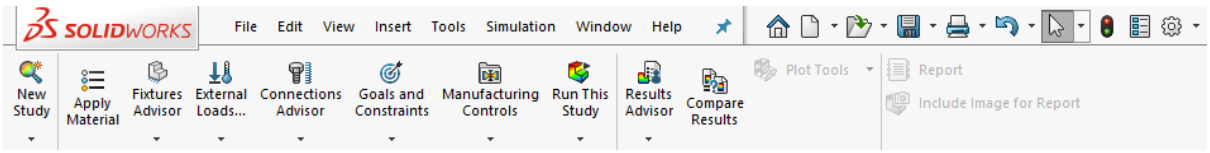

Figure 3.2 - Optimization process for SW

Table 6 - Manufacturing constraints available in SW

Manufacturing constraints
Thickness Constraint
De-mold Direction
Planar symmetry
Preserved regions

3.2.3 Fusion360

In Fusion360, it is Generative Design that is used to obtain a solution for an optimized design. Generative design gives affordable (free for students) access to powerful cloud computing, which empowers it to be very fast and generate several outcomes in one run (Matthew, 2017). Several manufacturing methods/constraints (listed in Table 7) are available, and all can be run at the same time. This makes the part optimized for a specific manufacturing method. When such optimization is finished, it is possible to use a comparison tool that shows all different features and makes it easy to compare the different solutions from each manufacturing method.

Figure 3.3 shows the optimization process from start to stop. It is an option to start with an explanatory guide. Loads and constraints opportunities are few and simple and this makes it difficult to set up a real and correct situation. However, generative design is a simple and straightforwardly tool to use. Before running the optimization, a checklist tells if all necessary setups are set, and it is possible to preview the result. It is not possible to choose mesh elements. Only options are coarse or fine resolution, and no indication how coarse or how fine. AlSi10Mg is an option in the material library, but it does not have anisotropic material properties such as AM material usually have.

Fusion360 generates several outcomes from one optimization depending on what manufacturing constraints and material that is selected. With only AM constraints and one material selected, it gives us four different outcomes, dependent on the printing direction, X, Y, and Z. The last one is unrestricted, meaning no AM rule applies.

Fusion360 estimates manufacturing cost.

Figure 3.3 - Optimization process for Generative Design

Table 7 - Manufacturing constraints available in Fusion360

Manufacturing Constraints
Additive Manufacturing
Tree and Five-Axis Milling
Two-Axis Cutting
Die Casting

3.2.4 Abaqus

Tosca structure is a plug-in to Abaqus CAE 2017 and is used for TO. Abaqus Tosca is a much more advanced optimization tool than the others that are discussed in this chapter. Figure 3.4 shows the dropdown menu that must be worked through to set up an optimization. This is more time consuming than all the other TO tools explained earlier. The CAD environment in Abaqus is outdated and inadequate. It is therefore to recommend doing CAD in another software and import the STEP-file to Abaqus. There is no material library, so the material must be manually filled in. All sorts of mesh are possible to use. A ton of options for the load and constraint setup. Many options in all parts of the optimization set-up, this is more explained in the next chapter. To steer the optimization in the desired direction, the geometric restriction in Table 8 are options. When the optimization is finished, smoothening must be done before extracting the STL-file.

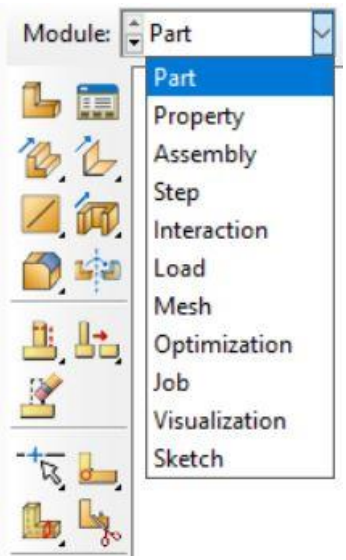

Figure 3.4 - Optimization process for Abaqus Tosca

Table 8 - Geometric restriction available in Abaqus Tosca

Geometric Restriction
Frozen Area
Member Size
Demold Control
Planar Symmetry
Rotational Symmetry
Cyclic Symmetry
Point Symmetry

3.2.5 Comparing Topology Optimization Tool

To understand what basis of comparison to use to achieve the best evaluation of the different software, the intention of the TO must be understood. In this case, the intention is not to achieve the most correct solution from the TO. The are several other load cases that the steering arrangement is exposed to, so the one used in the TO is not the whole solution. The intention is therefore to use TO as a tool to reveal solutions that is most likely to withstand the other load cases as well as the one given.

New software editions are constantly emerging. The editions utilized here are SolidWorks 2019, Abaqus 2017, Fusion360 2019, NX 12 for TO, and NX 1911 for CAD re-construction.

In Table 9, 24 key-features are listed as the basis of this comparison. These features are essential to get good results and roughly tells how many different opportunities each solver has.

Table 9 - Comparing the different topology optimization software

	SolidWorks	Abaqus	NX	Fusion360
Import of files STEP/IGES	Yes	Yes	Yes, need to use copy face for TO recognize features	Yes
Modify imported files	Yes	Yes	Yes	Yes
Material options	Library, not AlSi10Mg	No. Material manually added	Library, not AlSi10Mg	Library, with AlSi10Mg
Several design space	No	Yes	Yes	Yes
Non-design space	Yes, preserved regions	Yes, frozen areas	Yes, no design space	Yes, preserve geometry
Type of mesh and elements	Tetrahedron with 4, 16 or 29 Jacobian points	- Tetrahedron linear and quadratic - Hex linear and quadric - Wedge linear and quadric	No mesh	No mesh
Size of elements	Choose between coarse and fine. No value	Type any value	N/A	N/A
Several meshes in the same model	No. But possibility of local mesh control.	Yes.	N/A	N/A
Rigid element	No. However, remote load/mass, advanced fixtures, and several connections setting give more options.	Yes.	No.	No.
If not mesh, the possibility to change resolution scale	N/A	N/A	Yes. Coarse – Fine. Manual override possible	No.

Several load cases	Yes.	Yes.	Yes.	Yes.
Design objectives and constraints	-Best stiffness to weight ratio. -Minimize maximum displacement. -Minimize mass. Constraints: Mass, displacement, stress, and frequency	A long list, most common, is presented here. -Maximize strain energy. -Minimize volume. -Minimize mass. -Maximize frequency Constraints: mass, strain energy, volume, stress, eigenfrequency from modal analysis, displacement.	-Minimize strain energy and mass value as a constraint. -Minimize volume with constraints on safety factor. -Maximize natural frequency and mass value as a constraint.	-Minimize mass with a constraint on material safety factor. -Maximize stiffness with constraints on mass and safety factor.
Manufacturing constraints	Member size (min and max thickness) De-mold direction	Member size (min and max thickness) De-mold control	-Overhang prevention -Self-supporting -Void fill -Extrude along a vector -Draft	-AM constraints (overhang angle and min. thickness) -Milling constraint (2.5 – 3 and 5 axes, tool direction, min. tool diameter, tool shoulder-length, head diameter) -2 axis cutting direction -Die casting (Min. draft angle, ejection direction, min. and max. thickness)
Constraints to steer the optimization apart from manufacturing constraints	-Planar symmetry	-Planar symmetry -Rotational symmetry -Cyclic symmetry -Point symmetry	-Planar symmetry -Rotational symmetry -Material spreading	No.
Possibility to change parameters of optimization law	No.	Yes. SIMP or RAMP	No.	No.
Change convergence criteria	No.	Yes. Either objective function delta criterion or element density criterion or both can be adjusted.	No.	No.
Change the amount of optimization iterations	No.	Yes. A maximum cycle can be set	No.	No.
Change computing resource	No.	Yes.	No.	No. Optimization is done on the cloud.

Graph or report from optimization	Yes.	Yes.	Yes.	No.
Preview of result	No.	No.	No.	Yes. Not accurate
Result from each cycle	No. However, able to adjust material mass and mesh smoothing.	Yes.	No.	Yes.
Max stress and displacement on the result	No. Only from the entire model. Not reliable.	Yes. Roughly estimate.	Yes. Roughly estimate.	Only values in the report. No location for displacement. Poor indication for stress, shows only high or low.
Export to solid	No.	No.	No.	Yes.
Guided optimization	No. But a simple task list is available.	No.	Yes.	Yes.

3.3 Re-construction of CAD

The result file from the TO is an STL-file which can be directly printed, but it is a problematic file type to do further work on. The TO results in this thesis needs to be further investigated in the form of FE-analysis, and therefore a CAD must be modeled. Today there is no gold standard on how to create a CAD from an STL-file, and this can sometimes be the most time-consuming bit of the TO process.

Mainly different options for re-construction of CAD

1. Modeling upon the STL by eye.
2. Steel geometry from STL. Use that for extrude, hole, loft, etc.
3. Software recognizes surfaces.

Options in NX for re-construct CAD

- Realize shape 1, 2 & 3.
- Reversed engineering and use of convergent technology 1, 2 & 3.

Options in SolidWorks for re-construct CAD

- Mesh Prep Wizard in ScanTo3D (SW professional add-in) 1, 2 & 3.
- Mesh Modelling 2 & 3.
- Geomagic for SolidWorks (separately purchased add-in).

Options in Fusin360

- T-spline plane wrapped around mesh 1 & 3.

Methods used in this master thesis are NX realize shape, mesh modeling in SW, and mesh prep wizard in SW. The last one was done from an optimization completed in Abaqus in the project thesis, autumn 2019.

CAD re-construction in NX realize shape

1. Import STL and change transparency.
2. Extrude the cylindrical zones in modeling application.
3. Use section tube command to fill the inside of the STL-surface with solid.
4. Adjust the cage, so it fits.
5. Unite subdivision body and solid body.
6. Add fillets and chamfer and a small adjustment in the modeling application.

The process is illustrated in Figure 3.5.

Note: Section tube command is only available in NX 1872 series and newer.

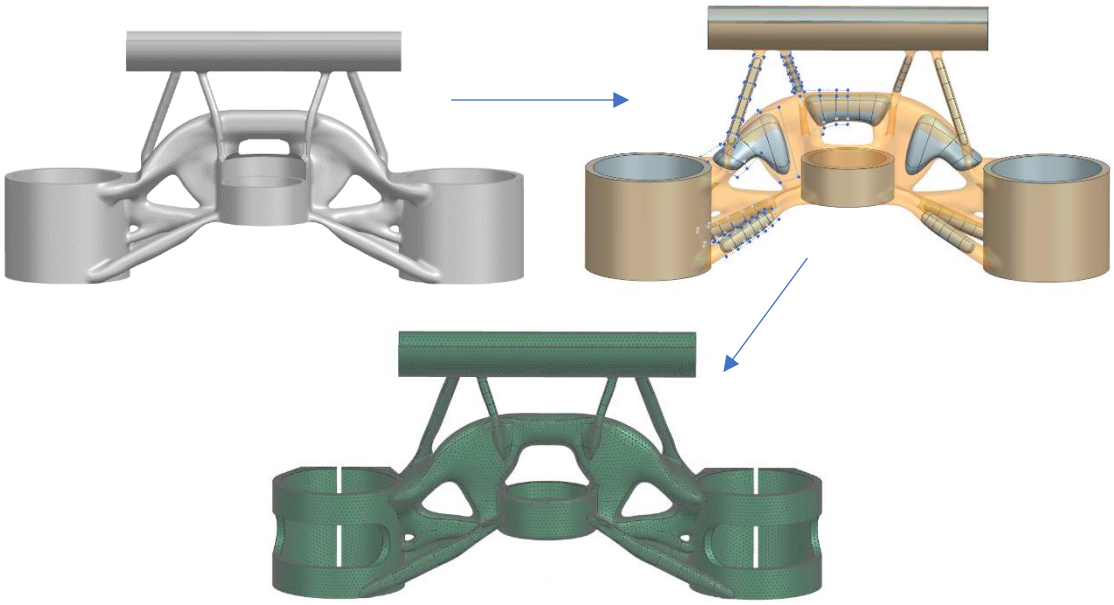

Figure 3.5 - Re-construction procedure of CAD in NX. From STL to modeling stage in *Realize shape* application to meshed FEM-model.

CAD re-construction in SolidWorks

1. Import STL to graphic body.
2. Convert to MeshBody.
3. Extrude the cylinder zones.
4. Slice facet body and loft.
5. Adjust the loft, so it fits.
6. Add fillets and chamfer and small adjustments.
7. Suppress facet body.

The process is illustrated in Figure 3.6.

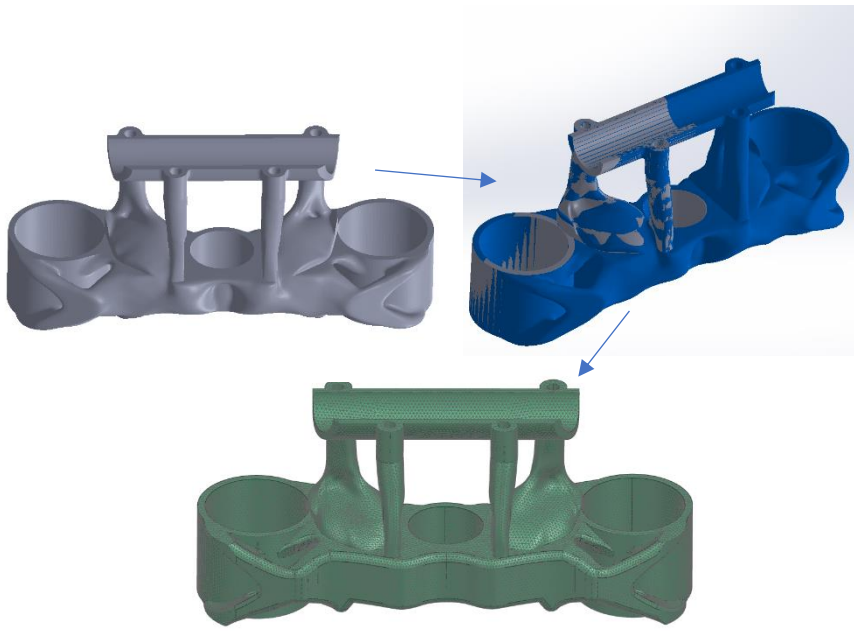

Figure 3.6 - Re-construction procedure of CAD in SolidWorks. From STL to modeling stage in *Mesh modeling* application to meshed FEM-model.

CAD re-construction in Fusion360

One massive benefit in Fusion360 is that after a TO it is just one click, and then you have a solid model.

1. Export solid

The solid will have strange faces and curves, and it can be difficult to adjust such a part.

In Abaqus, there are no good options for the re-construction. Therefore the actual re-construction with Abaqus result is done in separate CAD-software, NX, and SW.

CAD re-construction in NX with Abaqus result

1. Smooth and extract STL from Abaqus and import this to NX
2. Mirror feature
3. Extrude the cylindrical zones in modeling application.
4. Start symmetric modeling and use section tube command to fill the inside of the STL-surface with solid.
5. Adjust the cage, so it fits.
6. Unite subdivision body and solid body
7. Add fillets and chamfer and small adjustments in the modeling application.

The process is illustrated in Figure 3.7.

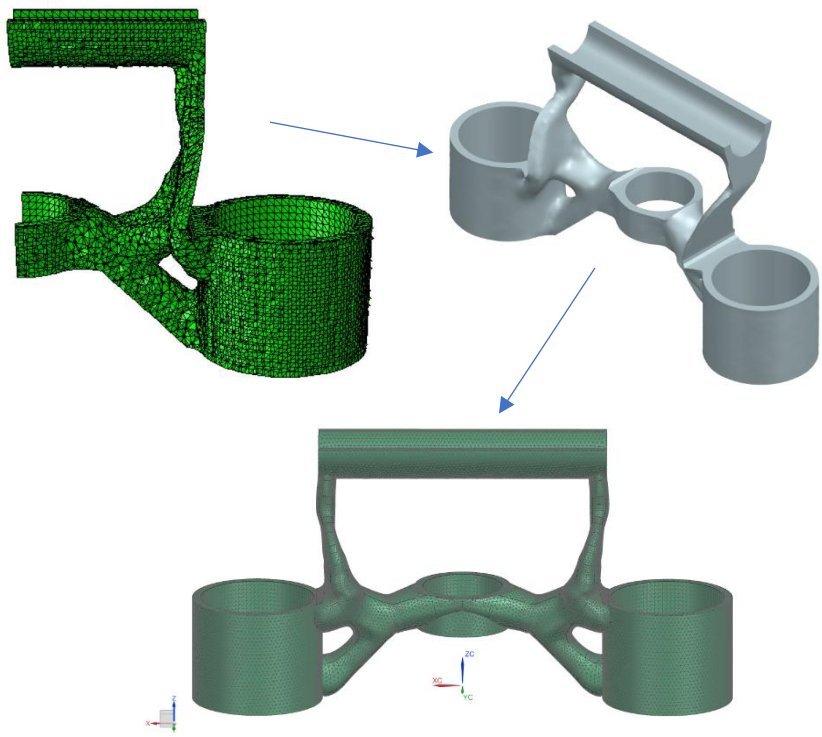

Figure 3.7 - Re-construction procedure of CAD with Abaqus optimized result in NX. From unsmoothed ODB-file in Abaqus to STL in NX to meshed FEM-model.

CAD re-construction in SW with Abaqus results

This was done in the project thesis and has not been done in the master thesis. Figure 3.8 shows HBU after optimizing (nr 17 in Figure 1.2). The mesh file from Abaqus needs to be smoothed in order to create a good solid. This is done in a separate software called MeshLab. In this software, a point cloud is created, and that makes the modeling easier.

1. Import to Meshlab
2. Create point cloud and smooth the mesh
3. Import point cloud to SolidWorks
4. MeshPrep Wizard in ScanTo3D add-in was used to create surfaces
5. Thicken surfaces

The process is illustrated in Figure 3.8.

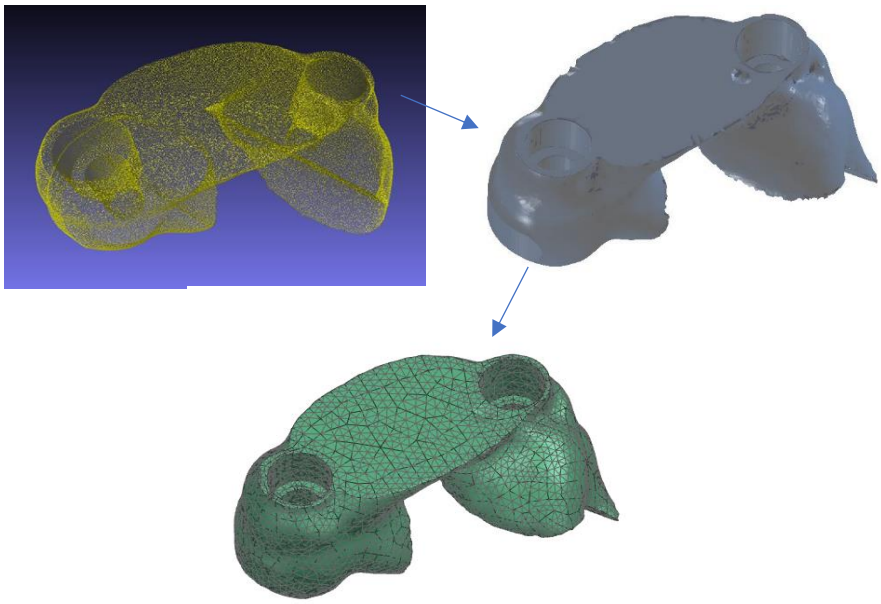

Figure 3.8 - Re-construction procedure of CAD with Abaqus optimized result in SolidWorks. From point cloud (XYZ-file) in MeshLab to graphics body in SolidWorks to meshed FEM-model.

3.4 Load Scenario

To develop a steering arrangement that is lighter than the one Ducati have on their Multistrada today without compromising the required strength, it is necessary to understand how it is assembled and what it is being exposed to. The assembly is shown in an exploded view in Figure 1.2.

In this master's thesis, no external load scenario has been given from Ducati. The only load case given from Ducati was the internal loads for tightening the handlebar. All external loads are therefore presumed by the help of sensibilities and reason.

Only the most critical external loads are utilized in the TO. Other load scenarios will be checked for stresses and displacements in a separate FE-analysis on a re-constructed model.

According to Ducati, this bike is built to maximize the concept of versatility (Ducati, 2020a), this entails that it is supposed to withstand all kinds of roads in any condition. It will experience shock loads, acceleration loads, deceleration loads and vibration, and all this over a longer period, which means that it is prone to fatigue.

Drivers and engineers agree that the braking phase is the most critical and sensitive maneuver. Optimal braking can make the difference (Corno et al., 2008), this is also one of the most stressful situations for the SHB and is therefore used in the TO. From the TO result, a CAD model was made, and the other load scenarios were simulated and checked in NX Nastran.

The pre-loads for the tightening of the handlebar are calculated to be 22 740 N, see Appendix B.

The maximum possible deceleration without a flip over on the Multistrada is 1.39 G, and this results in a force F_H acting on the handlebar. This force is calculated to be 1 534 N and points in the driving direction, see Appendix B.

Lateral displacement is the distance the wheel has offset from the steering axis. This can happen with motorcycles with a triple tree suspension setup when it experiences bumps or other imperfections in the road. This causes axial forces in each suspension fork and in opposite directions. See Figure 3.9 from *Motorcycle Handling and Chassis Design* (Foale, 2006). The force F_L caused by this is calculated to be 7 602 N, see Appendix B. To avoid asymmetry in the TO, both F_L are applied in the same direction.

Acceleration can be wheeling-limited and traction-limited. In this case, wheeling-limited acceleration is what exerts the highest load on the SHB. This load is calculated in Appendix B to be 740 N and point in the opposite way of the driving direction.

It is important to keep in mind that maximum acceleration and maximum deceleration are exaggerated and rarely occur.

The fatigue loads are based on the acceleration and deceleration load. 30 % of maximum acceleration load is used in all cycles, this is a load of 222 N. Loads from 100 % (1534 N), 80% (1228 N), 60% (920 N), 40% (614 N), 30% (460 N), 20% (307 N) and 10 % (153 N) of the maximum deceleration are also utilized. The lowest deceleration fraction is more frequently used. The steering torque that occurs when turning in high speed is low compared to those mentioned above and are therefore neglected in fatigue calculation. The same applies to vibrations.

All loads are listed in Table 10, and the load's directions are illustrated in Figure 3.10.

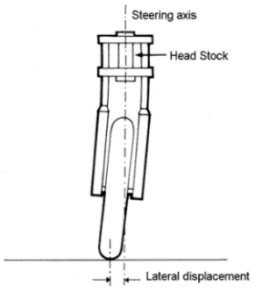

Figure 3.9 - Lateral displacement. Picture from *Motorcycle Handling and Chassis Design* (Foale, 2006)

Table 10 - Loads utilized in TO, FEM verifications and fatigue calculations

Description	*Load, [N]*
Bolt pre-load on the bracket to hold the handlebar in place.	22 740
Maximum deceleration load.	1 534
Bump load in suspension clamps.	7 602
Maximum acceleration load.	740
Fatigue load acceleration.	222
Fatigue load deceleration.	1 534, 1228, 920, 614, 460, 307 & 153

As illustrated in Figure 3.10, the acceleration and deceleration loads are tilted 25°. That is due to the rake angle[2]. All drivers are different, so the angle between the rake angle and the shoulder/overarm has not been included in the assessment. This is a more conservative solution, with an increased angle, the bending moment exerted on the SHB would be decreased.

[2] The angle the headstock is tilted back from vertical

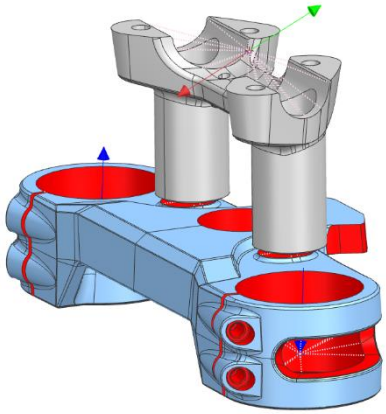

Figure 3.10 - Illustration to show which direction the loads point. Blue are bump loads, red are deceleration load, and green are acceleration.

3.5 Fatigue

The fatigue limit[3] given in the material data sheet[4] is 97 MPa. Chances that some substantial deceleration causes the stress to rise above 97 MPa is present. A further investigation was therefore preferable. There has been no statistic available on how often and how much the motorcycle is exposed to acceleration and deceleration, and no experiment or measurement has been performed. This is critical to predict the life but has been presumed based on own experience and reason. Therefore, may the fatigue limit presented here vary from the realistic fatigue limit.

Palmgren-Miner rule (eq.(7)) and a Smith, Watson, and Topper (SWT) correction have been used to make this prediction, see Appendix D . Since there was not attached an S-N curve to the material datasheet, the S-N curve (Figure 0.32 in Appendix D) are obtained from a Science Direct article (Uzan et al., 2017) which is about the fatigue resistance of AM-SLM AlSi10Mg. The specimens that the S-N curve is based on are printed in Z-direction in an EOSINT M-280 machine.

Palmgren-Miner rule consists of N_j, N_{fj}, and B_f, where N_j is the number of reputations, N_{fj} is the number of reputations to failure, and B_f is the number of 10 kilometers before failure. The failure occurs if;

$$B_f \sum_{j=1}^{N} \frac{N_j}{N_{fj}} \geq 1 \tag{7}$$

[3] Stress level below which fatigue failure does not occur. Where the S-N curve becomes flat (20).
[4] Material Data sheet, EOS Aluminium AlSi10Mg are in Appendix F

4 Results

4.1 Topology Optimization with different tools and methods

All TO results from the different software are presented in this chapter. In every software, the same load and constraints set-up is used. Fully fixed constraints in headstock connection hole. The force from the handlebar point straight forward minus the rake angle, which is 25°. Upward force in both suspension clamps. Values are in Table 10. An illustration of the load directions are shown on the OEM-part in Figure 4.1.

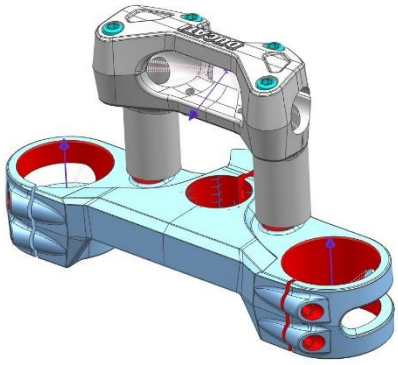

Figure 4.1 - Set-up that is used in the TO

AlSi10Mg is an anisotropic material with different properties in horizontal direction compared to the vertical direction. The material datasheet is found in Appendix F. The mechanical properties and density used in the TO are listed in Table 11. Fusion360 was the only software that had AlSi10Mg in its library, and this was used. It is not anisotropic and had slightly different properties, see Table 12.

Table 11 - Material properties for AlSi10Mg

Material Properties for AlSi10Mg		
	Horizontal direction (XY)	Vertical direction (Z)
Tensile strength	345 MPa	350 MPa
Yield strength (Rp 0.2 %)	230 MPa	230 MPa
Modulus of elasticity	70 GPa	60 GPa
Poisson's ratio	0.33	0.33
Density	2.67 g/cm^3	2.67 g/cm^3

Table 12 - Material properties for AlSi10Mg in Fusion360

Material Properties for AlSi10Mg in Fusion360	
Tensile strength	460 MPa
Yield strength (Rp 0.2 %)	240 MPa
Modulus of elasticity	71 GPa
Poisson's ratio	0,33
Density	2.67 g/cm^3

4.1.1 Siemens NX TOD

From Table 5, all design constraints available in NX TOD are listed. In this set-up, *Planar Symmetry*, *Void-Fill,* and *Overhang Prevention* were selected. The objective was to minimize the strain energy subject to mass target, and the optimization constraint was a mass target of 0.5 kg. The global resolution was set to 6 mm. The optimization took 7 308 s, which is approximately 2 hours. In Figure 4.2, the design space and the result are shown. The pink transparent body is set to design space, and the gray extruded box inside it are non-design space. Surfaces in the handlebar holder, suspension clamp, and headstock connection hole are set to *keep out*, and offset thickness to 4 mm, this is to keep these regions out of the optimization.

From the optimization result, the maximum stress is allegedly 167 MPa in the transition between the struts and suspension clamps and in the transition between the headstock connection ring and the struts. The maximum displacement is 0.77 mm in the suspension clamps. In Appendix C , these values are compared to the re-constructed CAD, maximum stress was 166 MPa, and maximum displacement was 0.47 mm. The final weight was 0.546 kg.

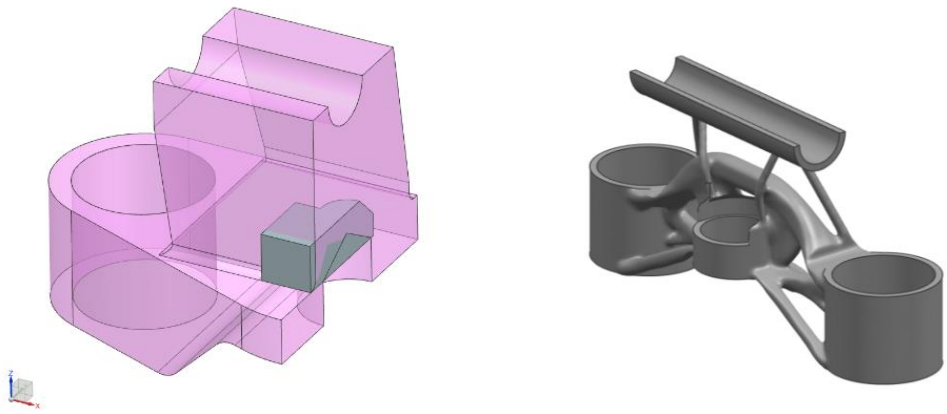

Figure 4.2 - Design space and result of optimization in NX TOD

4.1.2 SolidWorks

In Figure 4.3, the design space and the result are shown. The same design space and keep out regions as in NX TOD was used. The best stiffness to weight ratio and a mass constraint on 0.5 kg was selected. Linear tetrahedron element was used in the mesh, and the mesh global size was set to 3 mm with a tolerance of 0.2 mm. From Table 6, planar symmetry and thickness constraints are used. The minimum thickness is set to 3 mm. After the optimization, an isovalue slider[5] can be adjusted, and a smoothening operation can be done. Figure 0.26 in Appendix C shows how the default result looks like. Critical material between the handlebar holder and the fixed constraints are missing. Therefore, the isovalue slider had to be adjusted to gain material in this region. That results in a much heavier part. The optimized part in Figure 4.3 is approximately 0.7 kg. SW tends to keep material in areas that are not contributing to the stiffness or strength of the part. It was not made a solid out of this result due to high mass.

[5] Slider to add or remove material from optimized model. Default position closely matches the mass constraints.

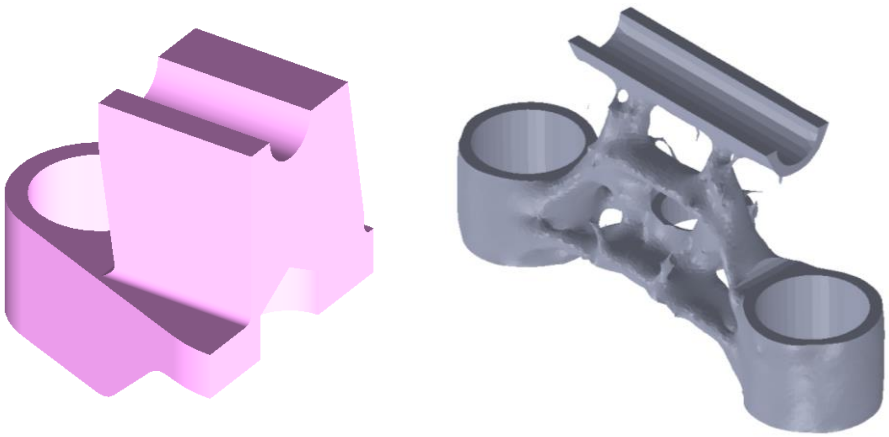

Figure 4.3 - Design space and result of optimization in SW simulations

4.1.3 Fusion360

In Fusion360, the design space contains *Starting Shape, preserved geometry*[6] , and *obstacle geometry*[7]. It is possible to use a *Starting Shape* (a kind of Design space), but it is not as effective as in the other software. Sometimes Fusion360 allows the optimized part to build outside the starting shape. To prevent this, obstacle geometry has to be used. Therefore only obstacle geometry and preserved geometry were used as the starting design. In Figure 4.4, the start design is shown, preserved geometry in green and obstacle geometry in red. Fusion360 generates several outcomes from the optimization. In this optimization, only the AM from Table 7 was selected, and then four outcomes are generated. One outcome for printing direction in X-axis, one for Y-axis and one for Z-axis and one unrestricted. The result shown in Figure 4.4 is restricted for printing in the Z-direction (standing direction).

The objective was maximizing the stiffness with a mass target on 0.5 kg. The safety factor was set to 1. The optimization resolution was set to the finest. The result does not show displacement, and the stresses are only shown in colors and not values. In Appendix C , an FE-analysis is performed on the exported solid. The maximum stress was 228 MPa in the transition between the headstock connection ring and the suspension clamps. The maximum displacement was 0.79 mm and in the handlebar holder and not in the suspension clamps like the others TO. In this, it was approximately 0.6 mm displacement in the suspension clamps.

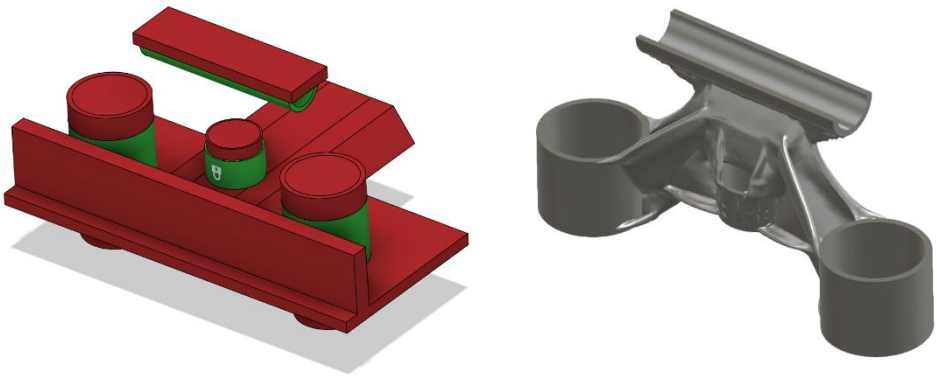

Figure 4.4 - Design space and result of optimization in Fusion360

[6] Bodies that incorporate in the final design and does not change during the optimization.
[7] Bodies with this geometry is represented as empty space where material is not distributed.

4.1.4 Abaqus

To maintain the same keep out regions in Abaqus, the part must be partitioned, and the desired regions must be set a geometric restriction (found in Table 8). Planar symmetry and frozen areas are the two geometric restrictions used in the optimization. In Figure 4.5, the design space and TO result is shown. The pink circles on the design space represent the frozen areas. The planar symmetry was set normal to the Y-Z plane. In the optimization, C3D4[8] elements with a global size of 3 mm are used.

The objective function was to minimize the strain energy, and the optimization constraint was set to a weight equal or below 0.520 kg. After CAD re-construction, the part was 0.617 kg, maximum displacement was 1.5 mm in the suspension clamps, and maximum stress was 385 MPa underneath the headstock connection ring.

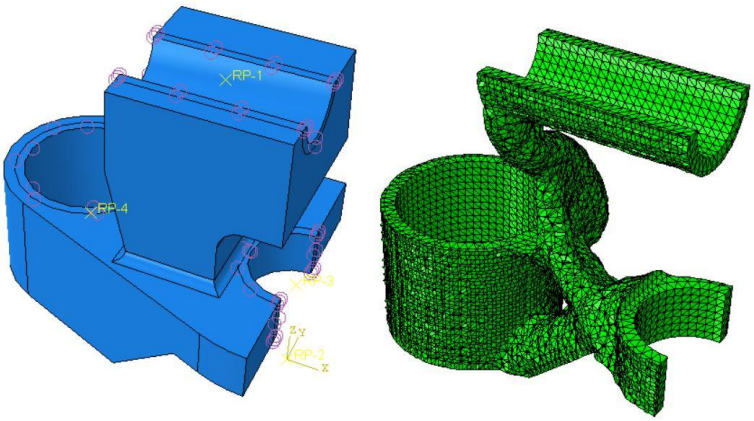

Figure 4.5 - Design space and result of optimization in ABAQUS Tosca

4.1.5 Choice of Topology Optimization Tool

The SHB will experience several other load scenarios, and it is not possible to meet all these requirements in one TO. Only the most significant load scenario was used in the TO. The result from the TO is therefore not the final solution. Modifications are needed to withstand other load scenarios. The TO is used as a tool to find smart and stylish solutions that withstand the most significant load scenario. It is also preferable that it is easy to do further work on to meet all the other requirements.

An evaluation to get a better overview of benefits in the different software tools has been done. In this evaluation, five key points have been rated from one to six, where six is the best result. This is based on results from the comparison of TO result with the FEA result in Appendix C and personal experience from the use of each software. The key points are:

Solving Time: The time used for the solver to run the optimization.

Set-up Time: The time used to set up each optimization.

Set-up Possibilities: Possibilities for design criteria, constraints, objectives, loads, mesh, etc.

CAD Re-construction: How easy is the CAD re-construction when given software are used for TO. Not necessarily re-constructed in the given software.

Usable Results: Are the requirements maintained? Structural analyzes have been run to ensure the necessary strength.

The results are shown in Figure 4.6.

[8] Linear tetrahedron elements

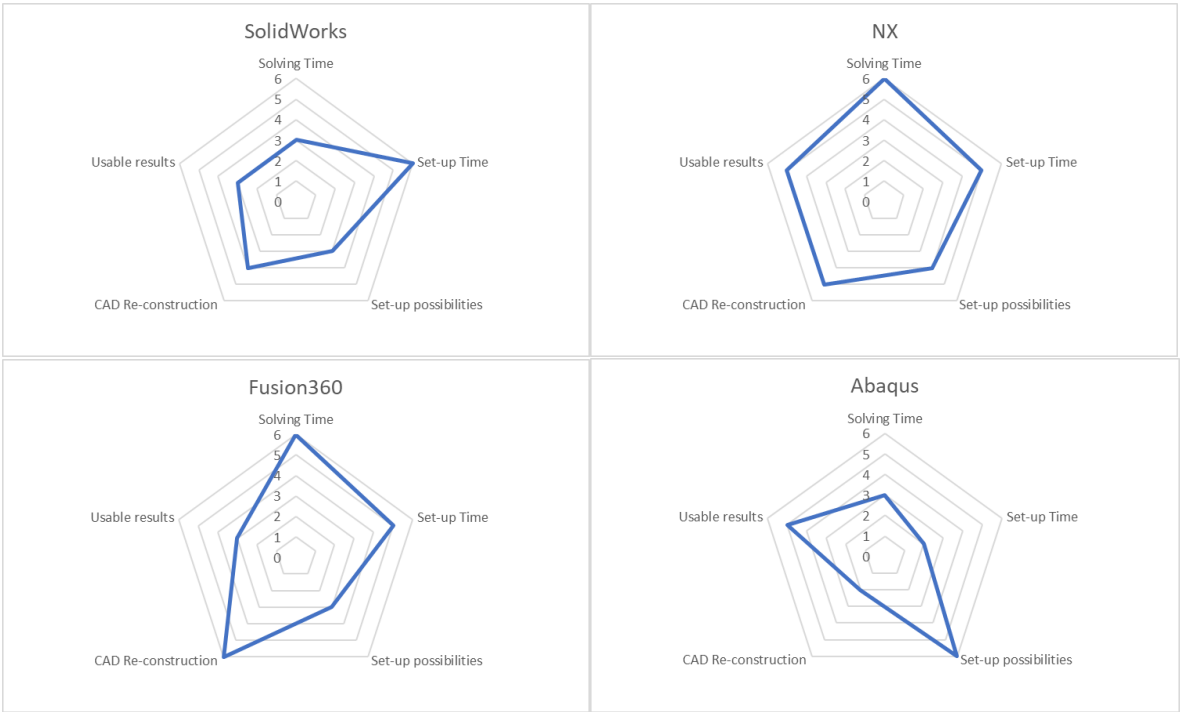

Figure 4.6 - Key points in a diamond diagram to compare software tools

NX TOD is in this case, the best software tool. The solving time and set-up time are short. It provides reliable results, so no modification in the CAD re-construction is needed to meet the requirements of the TO load scenario. All necessary operations are within the same software, this makes it easier to go between the different platforms. The realize shape application makes the CAD re-construction and further modification easy and fast. It has a wide range of design constraints, and this is helpful, especially when the outcome must be not only strong enough but also stylish with a selling design.

4.2 FEM Verification

Some FE-analysis has been completed to validate the model in situations it will experience, these are listed in Table 13 below. The calculations of all loads used in these analyses are presented in Appendix B. Mechanical properties for the material used are listed in Table 11. All stresses mentioned in this chapter are Von mises stresses.

The HBU are to be made in Aluminum 6061-T6, material property for this is found in Appendix F.

Table 13 - Description of different Finite Element Analysis

	Description
FEA-1	The set-up which the TO is based on. Extreme situation that rarely occurs.
FEA-2	Tightening of M8 bolts in handlebar holder
FEA-3	Maximum deceleration
FEA-4	Maximum acceleration

Several places in this chapter singularities are mentioned. In Appendix C , a convergence check is described. In FEA-1, FEA-3 and FEA-4, especially one inside corner and one element, always had significantly higher stress then its neighbor elements, and every investigation showed that this was a singularity.

For all analyses, there was used a linear static solver (SOL 101) in NX Nastran. FEA-2 has a non-linear solution, but with the help of bolt connection elements and surface to surface contact, it is possible to perform such an analysis in SOL101 and receive reliable results.

The original design has also been subjected to the same analyses except for FEA-2. This can be found in Appendix E . It helps the reader to read this subsection parallel with Appendix E .

FEA-1

Figure 4.7 shows how FEA-1 is set up. In the center of the headstock connection ring, handlebar holder, and both suspension clamp, there is a 1D collector with an RBE2 element. This means that all nodes on the surface are following the master node in the center. To simulate the handlebar, only half of the surface in the handlebar holder is connected to an RBE2 element. There has been used a 2 mm CTETRA(10)[9] element.

The master node in the headstock connection is fully fixed. In the left suspension clamp, the force of 7 602 N is applied on the master node in positive Z-direction, and the other clamp with the same force in negative Z-direction. The master node is not allowed to rotate about X- or Y-axis due to the stiffness of the suspension fork. The force of 1 534 N from the handlebar is applied in Y-direction minus the rake angle of 25°.

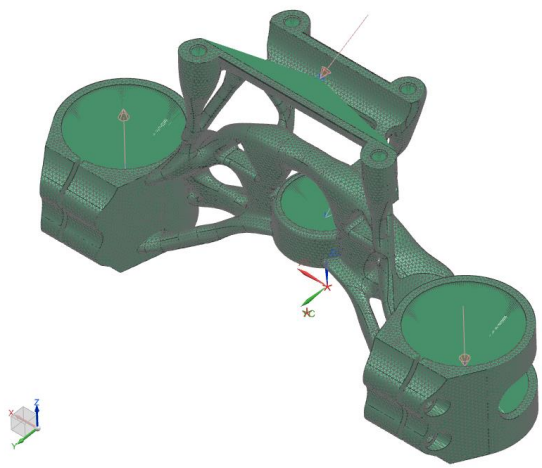

Figure 4.7 - FEA-1 set-up

Result FEA-1

The situation simulated in FEA-1 is an extreme situation that rarely occurs. All assumptions done for this load scenario are conservative. It is therefore accepted with stresses close to the yield strength of the material. The maximum stress of 291 MPa was in the transition between the headstock connection ring and the structure, see Figure 4.8. The mesh in this region was refined, and a new analysis was completed and showed significantly increased stress. The stress raised toward infinite. After this investigation, it was concluded that the maximum stress must be a singularity. Then the stress in this region is based on the average stress of the elements around the maximum element, shown in Figure 4.9. The average stress is 218 MPa, which is just below the yield strength of the material with a safety factor of 1.06. For comparing, the same scenario for the original design was approximately 400 MPa in the steering head around the headstock connection hole.

The displacement is shown in Figure 4.10, maximum deflection 0.42 mm is in the corner of the handlebar holder. The suspension clamps are approximately deflected 0.20 mm. In the original design, the maximum displacement is 1.3 mm in the suspension clamps and 0.15 mm in the handlebar holder.

[9] Quadratic tetrahedron elements

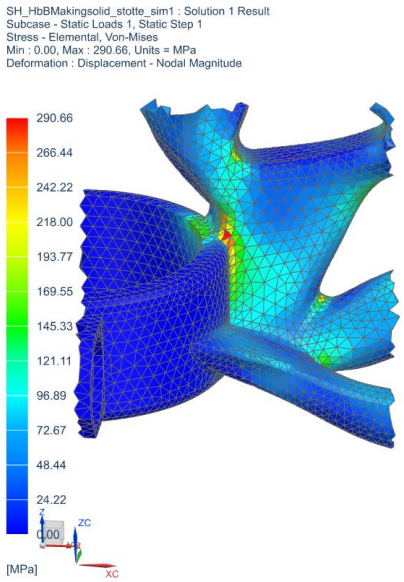

Figure 4.8 - FEA-1 maximum stress

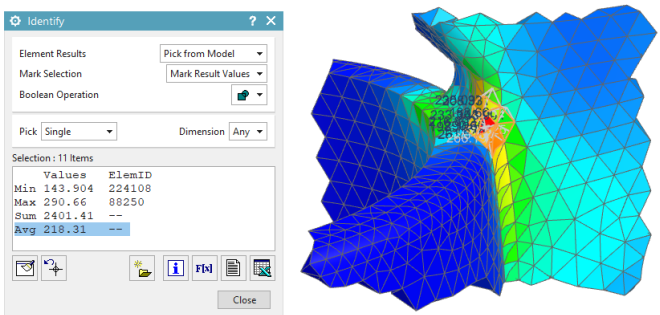

Figure 4.9 - FEA-1 average maximum stress

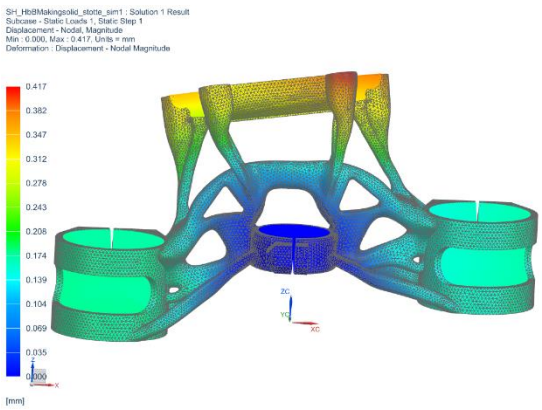

Figure 4.10 - FEA-1 displacement. Visually exaggerated by 10 %.

FEA-2

From Ducati, a tightening torque of 25 Nm ± 5 % on each M8 bolts on the handlebar holder was given. This torque results in a bolt pre-load of 22 740 N, see Appendix B. An assembly FEM was created and meshed. SHB is meshed with a 2 mm CTETRA(10) element, and contact surfaces are refined to 1 mm of the same element. HBU are meshed with a 1 mm CTETRA(10) element, and the handlebar is meshed with a 5 mm CHEXA(20) element. A surface-to-surface contact is used, and the correct friction coefficient for the contact is obtained from Engineering ToolBox (ToolBox, 2004). Respectively 0.6 between aluminum and steel, 1.2 between aluminum and

aluminum. The assembly is fixed in the headstock connection ring in the same node as in FEA-1. 1D bar collectors are used to simulate the bolted connections, and the pre-loads are applied to these. The set-up is shown in Figure 4.11.

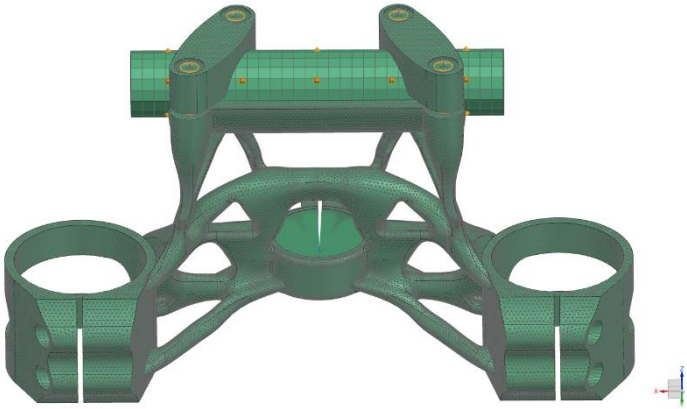

Figure 4.11 - FEA-2 set-up

Result FEA-2

Adjustment on the thickness to the handlebar holder, and below on the struts had to be done to reduce the stresses. The original clearance gap between HBU and SHB was 3 mm, this is reduced to 1.5 mm to reduce stresses on the HBU. The maximum stress is shown in Figure 4.12 and had a value of 767 MPa. It is concluded to be a singularity and is ignored. Then the maximum stress is reduced to 355 MPa on the edge of HBU, and average stress along the edge of 300 MPa, see Figure 4.13. On the edge of SHB, the stresses are around 250 MPa, and with average stress on 201 MPa, see Figure 4.14. Both these stresses are above the yield strength of the material. There will always be sharp contact points when two circular object meets, and this results in high stresses and cannot be prevented in this situation. When the material reaches the yield strength, it deforms and creates a better fit. The rest of HBU and SHB holds a stress far below the yield. The maximum displacement is obviously in the HBU on the gap side, this is 0.41 mm, see Figure 4.15.

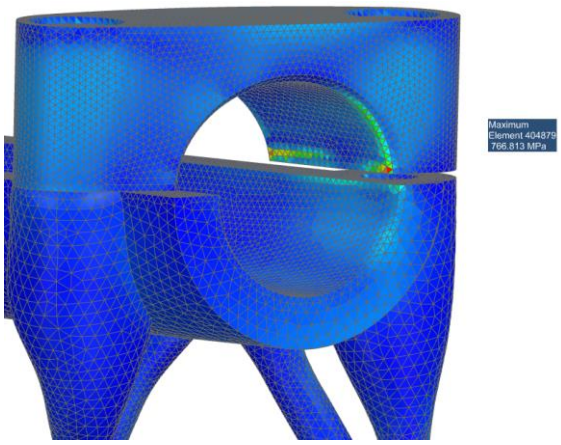

Figure 4.12 - FEA-2 maximum stress (handlebar is hided)

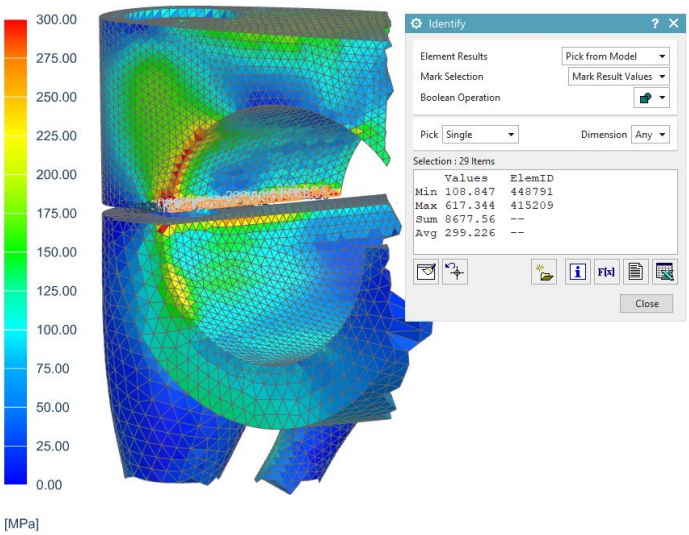

Figure 4.13 - FEA-2 average stress in the HBU (handlebar is hided)

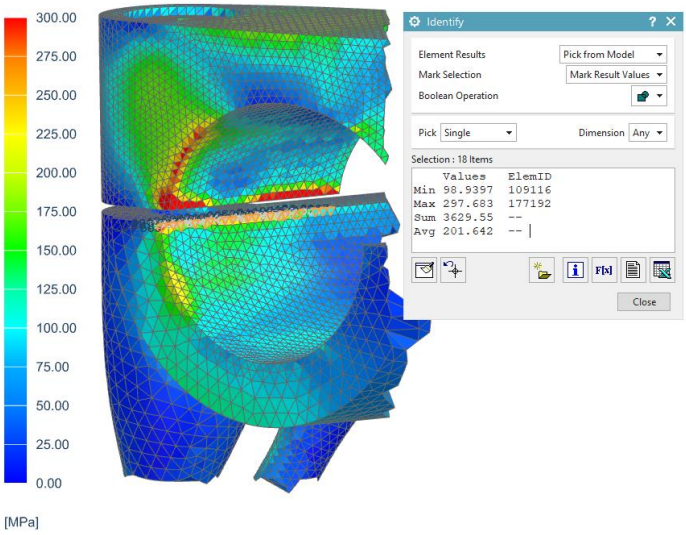

Figure 4.14 - FEA-2 average stress in SHB (handlebar is hided)

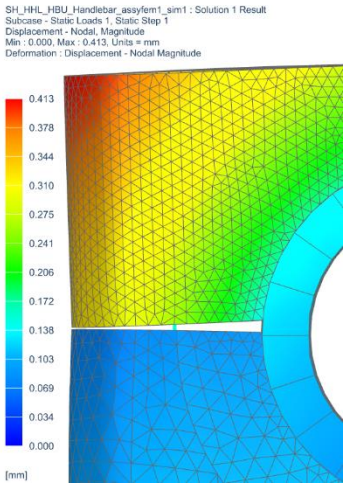

Figure 4.15 - FEA-2 displacement. Visually exaggerated by 0.5 %

FEA-3

CTETRA(10) elements with 2 mm size were used in this analysis. Maximum deceleration load of 1 534 N in y-direction minus the rake angle of 25°. Without the bump loads in the suspension clamps, the set-up is identical as in FEA-1.

FEA-3 Result

There was a singularity in the same corner as in FEA-1. By ignoring this, the maximum stress is reduced to approximately 178 MPa, see Figure 4.16. That is a safety factor of 1.29 to the yield strength of the material. In the original design, the stress was 70 MPa in the connection between HHL and the steering head. The maximum displacement is in the handlebar holder and is 0.41 mm, and in the suspension clamp, it is 0.20 mm, see Figure 4.17. For the original design, this displacement is 0.15 mm on the edge of HHL.

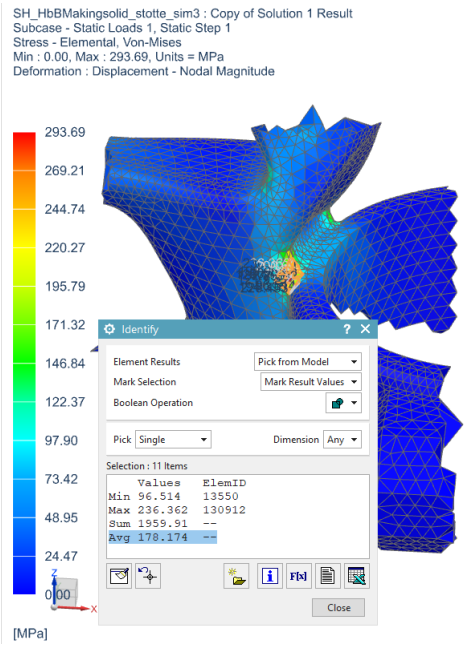

Figure 4.16 - FEA-3 average stress

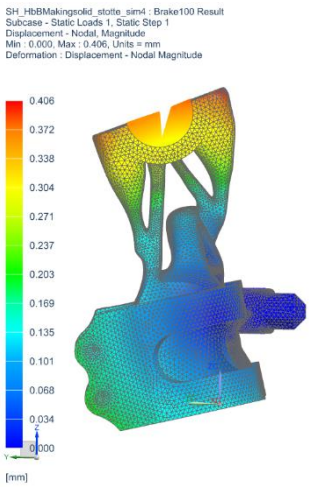

Figure 4.17 - FEA-3 displacement. Visually exaggerated 10 %

FEA-4

CTETRA(10) elements with 2 mm size were used in this analysis.

For maximum acceleration, the force points in negative Y-direction plus the rake angle of 25°. It is applied to the master node of an RBE2 element linked to one half of the handlebar holder surface to simulate the handlebar.

From Appendix B, the force magnitude is set to 740 N. SHB is fully fixed in the master node of the RBE2 element in the headstock connection ring. Figure 4.18 shows the set-up.

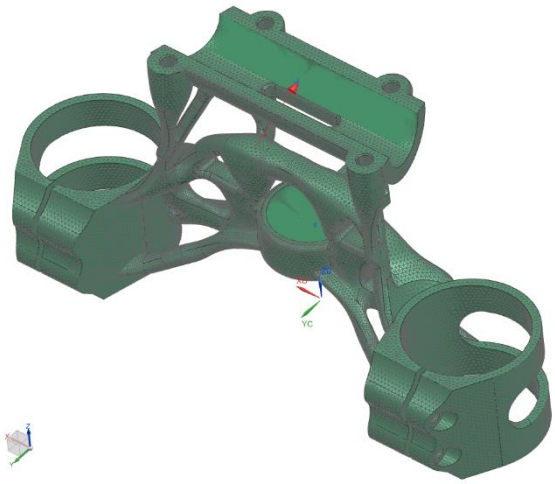

Figure 4.18 - FEA-4 set-up

FEA-4 Result

Singularity in the same corner as in FEA-1. By ignoring this, the maximum stress is reduced from 274 MPa to approximately 155 MPa, see Figure 4.19. That is a safety factor of 1.48 to the yield strength of the material. In the original design, the maximum stress was 34 MPa in the connection between HHL and the steering head. The maximum displacement is 0.19 mm in the handlebar holder, and the displacement in the suspension clamps is 0.08 mm, see Figure 4.20. For the original design, the maximum displacement was 0.07 mm in the handlebar holder.

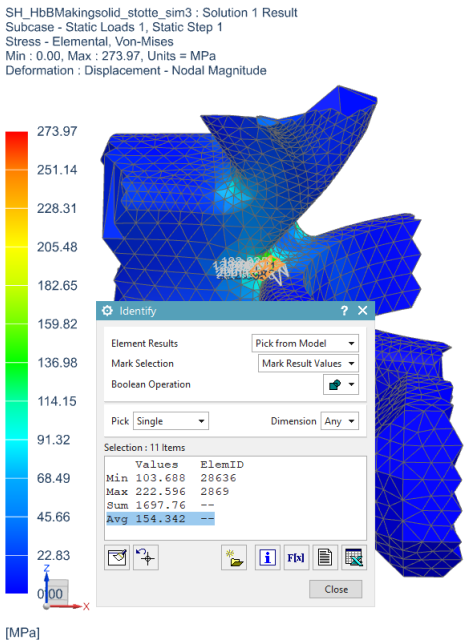

Figure 4.19 - FEA-4 average stress

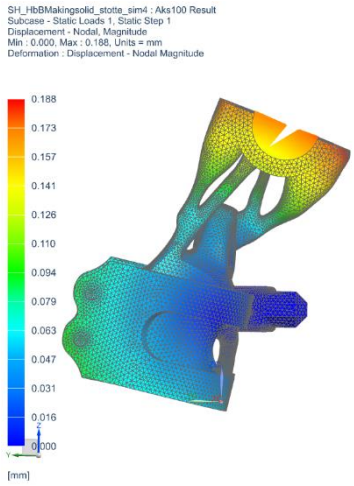

Figure 4.20 - FEA-4 displacement. Visually exaggerated 10 %.

4.3 Manufacturing Process

During the process of modeling and optimizing the SHB, AM has been kept in mind. Meaning that overhangs are minimized, self-supporting angles have been used as far as its possible. The model contains no voids to prevent that un-melted powder from the printer is trapped. The findings from the articles (Vandenbroucke and Kruth, 2007, Calignano, 2014, Han et al., 2018) in chapter 2.4.2 Design for Additive Manufacturing are the basis for the design.

SHB is fatigue calculated based on the "*after stress relief, machined and polished*" S-N curve from (Uzan et al., 2017). Therefore it is necessary to add some extra material in critical areas when 3D-printing so that after post-processing,[10] there is enough material. These areas are primarily in the clamps, the handlebar holder, headstock connection ring, and in the high stressed region in the transition between the struts and the headstock connection ring.

It will be printed without the bolt holes, these will be drilled out afterward.

The flowchart in Figure 2.10 has been followed to get the best supports. AutoDesk Netfabb has been used to build and calculate the necessary amount of support, see Figure 4.21. The volume of the SHB is 275.98 $cm^{3,}$ and the support volume is 19.78 cm^3. The printing time is estimated to take 66 hours and 25 minutes.

The HBU are designed with the intention that it shall be milled.

[10] Grinding, sandblasting and polishing.

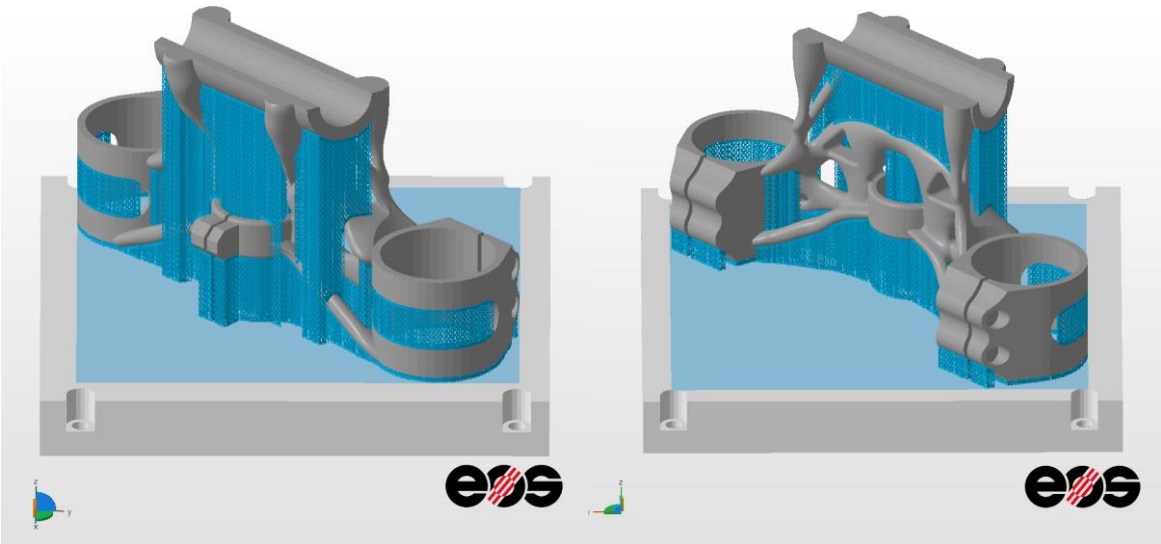

Figure 4.21 - Illustration of SHB in EOSINT M280 with support

4.4 Final Design

The final design of SHB and HBU is 474 g lighter than the original. The original design where 1 304 g, and the new design is 830 g. In Table 14, the weight on each part is listed. Figure 4.22 shows the original design, and Figure 4.23, Figure 4.24, Figure 4.25 and Figure 4.26 shows the new design. It is a lot slender without too much compromise on the strength and stiffness. The maximum displacement during maximum deceleration is 0.41 mm compared to 0.15 mm for the original design. The maximum displacement caused by the bump loads was on the other hand, smallest for SHB, with 0.46 mm compared to 1.3 mm in the suspension clamp. The new design contains fewer parts, 2x sleeve, 2x M10x70 screws, 2x washer are no longer needed. Steering head and HHL are now one part, but HBU has become two parts. This will result in less storage. The estimated life of the SHB is 1.052.630 km based on the calculation done in Appendix D .

SHB will be 3D-printed in AlSi10Mg in an EOSINT M-280 machine.

HBU has been split into two identical mirrored parts to save weight. The shape perfectly fits the edge of SHB. They are made of such size that the efficient area between the HBU, handlebar, and the handlebar holder remain somewhat the same as the original to maintain the pressure allowance. The HBUs are to be made in Al 6061-T6 and have been designed so they can easily be milled. The height is 1.5 mm higher on one side of the bracket, so it possible to accomplish enough pressure in between the handlebar and bracket to prevent the handlebar from taking an unwanted axial rotation.

Table 14 - Weight comparing OEM and new design

Steering head OEM	*HHL OEM*	*HBU OEM*	*SHB new**	*2x HBU new**
788 g	299 g	217 g	719 g	111 g

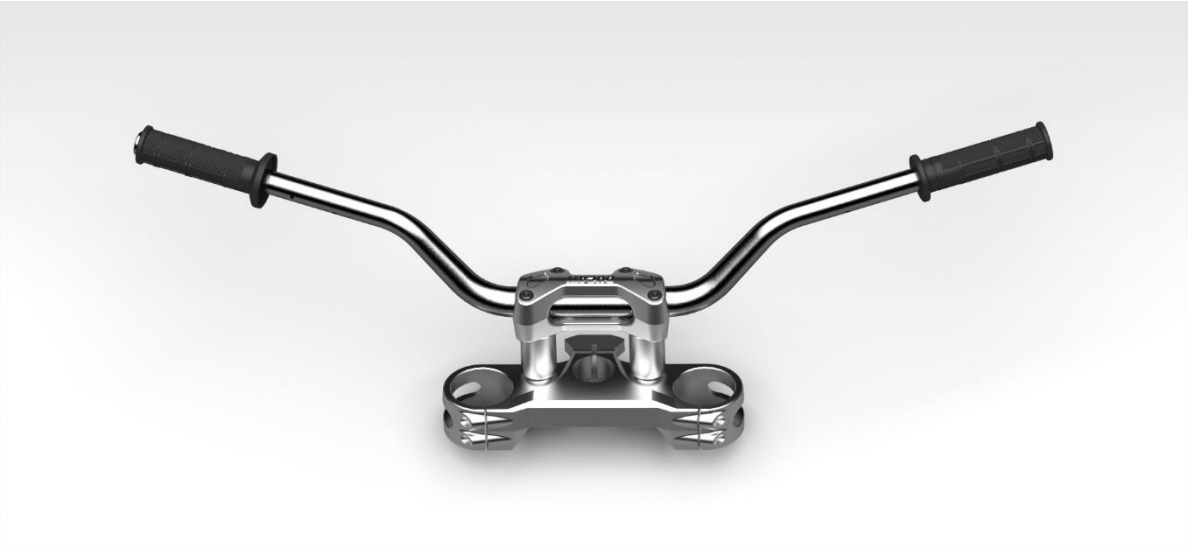

Figure 4.22 - Original design.

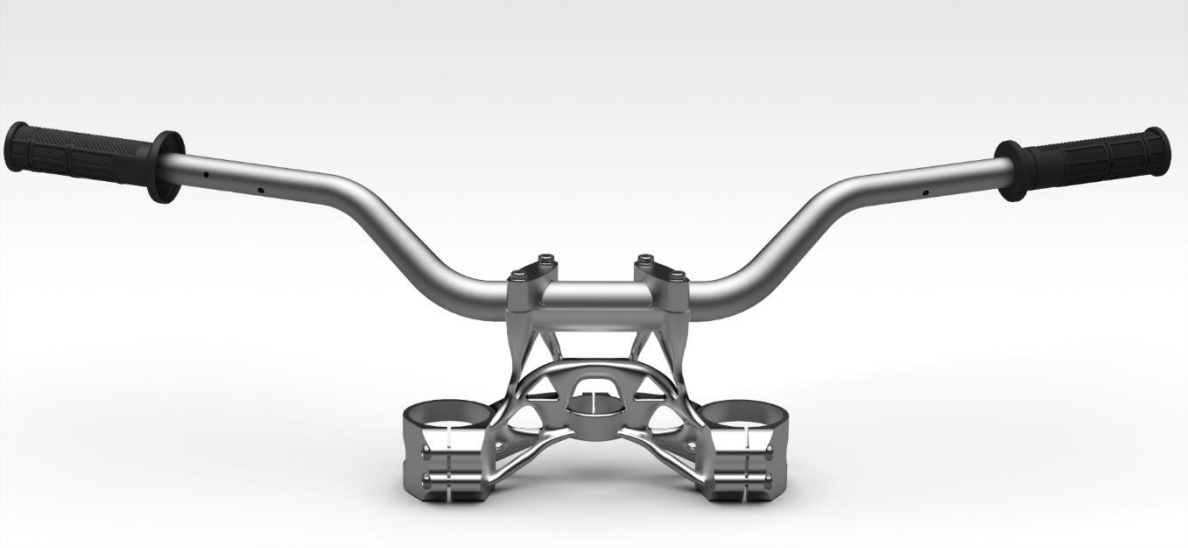

Figure 4.23 - New design seen from the front.

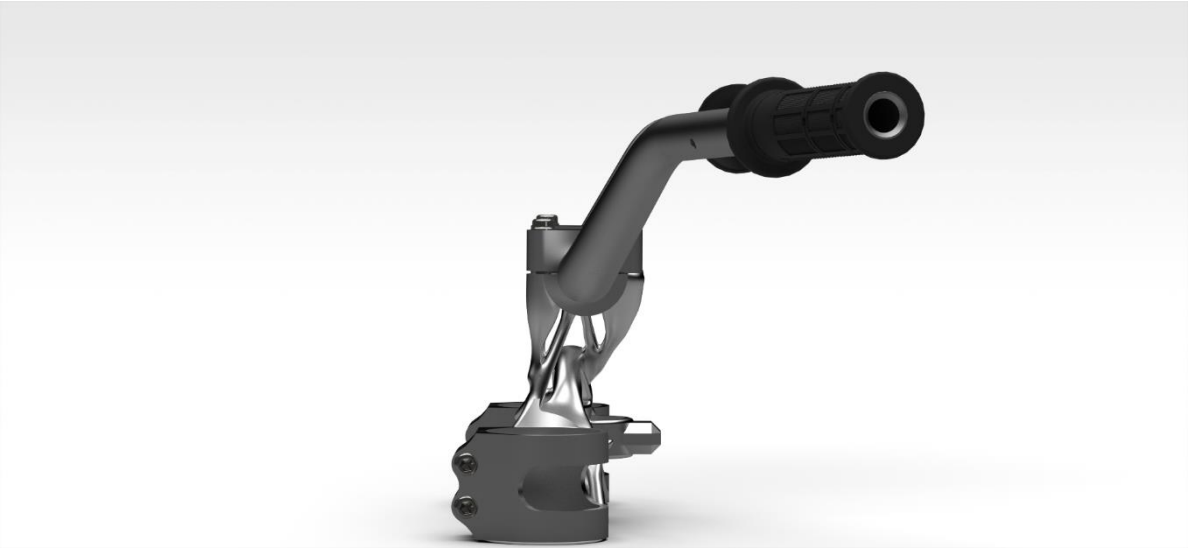

Figure 4.24 - New design seen from the side.

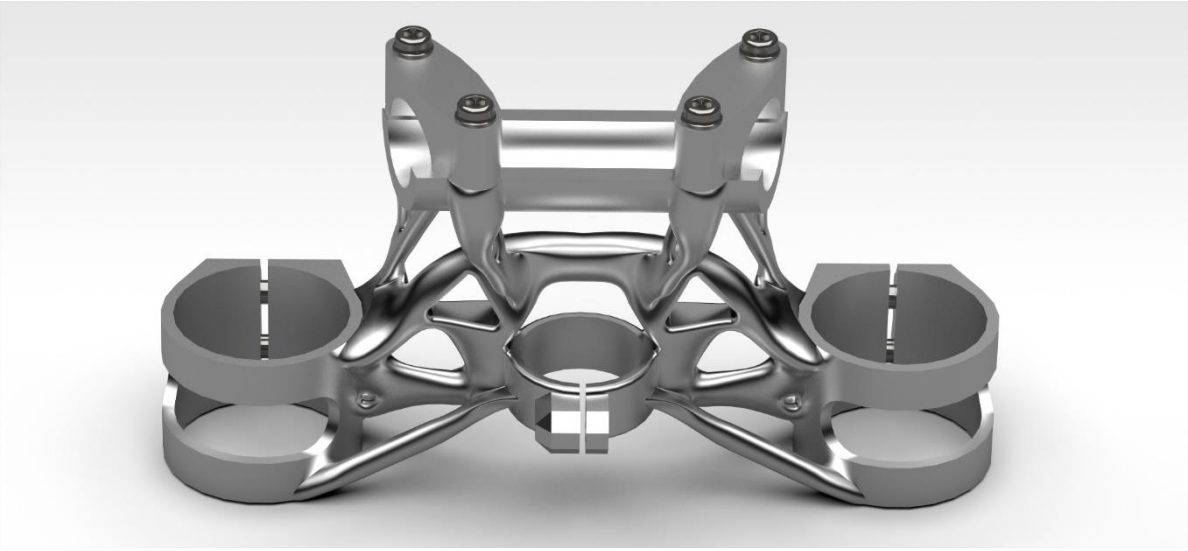

Figure 4.25 - SHB and HBU seen from behind.

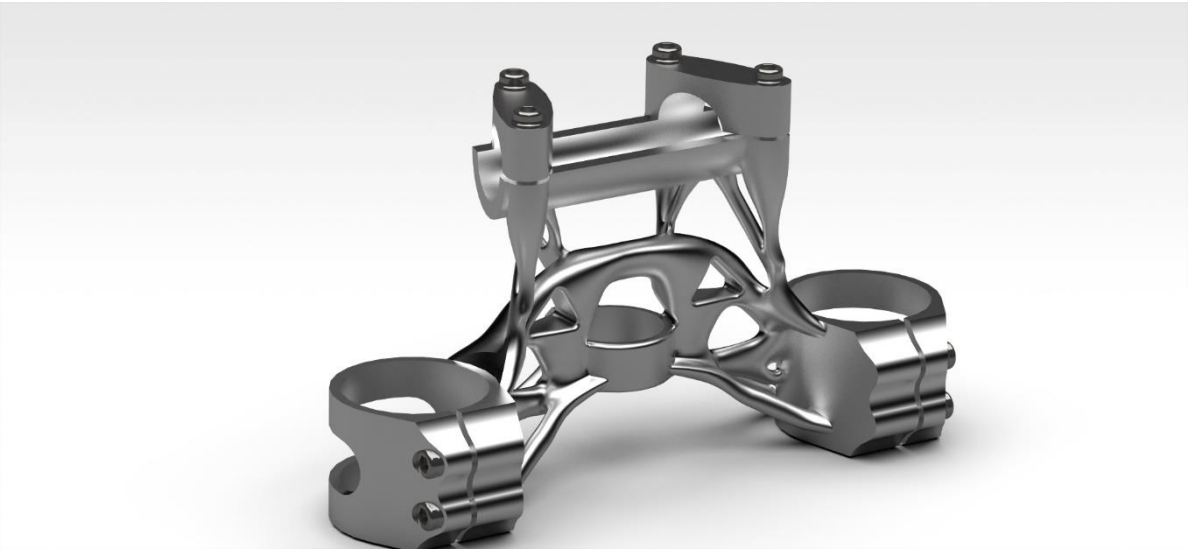

Figure 4.26 - SHB and HBU seen from the front.

5 Discussion and Conclusion

Ducati wanted to get a better overview of the possibilities to produces the steering arrangement with AM. A huge benefit with AM is that organic and unconventional forms can be produced. With the help of TO, it is possible to find the optimal material distribution to minimize the mass and maintain the stiffness. In this master's thesis, it is presented a solution that reduces the mass by 36 % without a notable decrease in stiffness.

5.1 Tools and Methods

There are pros and cons for all the software tested, and some were better than others in this situation. If it would have turned out different with another part and another load scenario can be discussed. SW had problem meeting the requirements, it failed to place material in regions that are critical to maintaining the structural stiffness in part. In Figure 3.6, a different load scenario and design space were used in SW, and then the outcome seemed reasonable. That part was not further investigated because it turned out that the load scenario was wrong. In Fusion360 Generative Design, all outcomes were made in such a matter that it did not allow support structure upon the model. Then the whole model got floating transitions that made the design look strange. Displacement and stresses in the TO result were higher than the displacement and stresses in the re-constructed model analysis. AlSi10Mg properties in Fusion360 were different from the properties used in the others TO tools. This is an essential factor that makes it problematic to compare this software with the others. Abaqus TO result showed far lower stress then what the re-constructed model showed. It was also heavier than what the TO result estimated. Drastic modifications and adjustments must have been made to make the re-constructed model compatible with the load scenario. *NX Topology Optimization for Designers* is maybe what is sounds like, and optimization tool for designers, and not engineers? When it comes to realistic set-up for the case, the options are few, that applies as well for Fusion360 and SW. However, when it comes to options that steer the optimization toward a desired design, there are a lot of selections possible, compared to Fusion360 and SW. Even so, the stress and displacement values estimated in the TO result were close to the stress and displacement found in the re-constructed analysis. These TO tools are only compared in this one case. A different outcome in another TO-analysis cannot be guaranteed. Table 9 shows 24 fundamental factors that may help in the selection of a TO tool.

The CAD re-construction was utilized in both SW and NX. In SW, two different methods were tested, mesh prep wizard and mesh modeling. Within mesh prep wizard, there are two different methods to use, *automatic creation* and *guided creation*. Automatic creation creates surfaces on the STL face, and these must manually be adjusted, so it fits. For higher precision, more surfaces need to be created. Then there is guided creation, were STL surfaces are painted in color, and that is the new face. The face must be in such order that it can be wrapped, or simple geometry can be used. Afterward, the additional surfaces must be trimmed. Guided creation works best for simple geometry, and automatic creation is better for more complex geometry. In NX, realize shape was used. Here the STL is "filled" with a subdivision body that is uncomplicated to adjust and model with. The time used re-construct in NX was a lot less than in SW. Just to learn the methods in SW was time-consuming and demanding. In NX, the process was intuitive and effortless. On the other hand, the re-constructed model in NX was not that accurate as in SW. It exists other more advanced methods/add-ons that are maybe faster and more accurate, but they are not free.

5.2 Steering Head and Handlebar Bracket Upper

A part like SHB that experience several different load scenarios at different times is rather difficult to fully optimize for all the scenarios. It was only optimized for one of them. Although many changes to the TO were necessary to meet all requirements, it gives a good first draft that could be further developed. Without the TO and AM, it would have been challenging to find the design and develop SHB with these properties. It can be discussed rather if the load scenario utilized in the TO is the best one or not. Does it represent a realistic situation that needs to be considered? Is it too conservative? If so, the total mass could have been further reduced. Stress in the original part is too high when it is exposed to the extreme situation of FEA-1, the displacement is also enormous, see Appendix E . This may indicate that the bases for the TO is too strict and probably the load presumptions were too high, especially the bump load.

FEM verification load scenarios were presumed the worst case. Is it too conservative that SHB should hold the total weight of a person during acceleration? And that the bump occurs during maximum deceleration. Testing and measuring the different load scenarios would have been desirable.

More time preparing the re-constructed model for FE-analysis probably should have been done. Adding fillets and reduce the amount of sharp inner corner would probably have saved us from many of the singularities.

The only basis that underpinned the choice of load history utilized in the fatigue calculations was my own experiences and reason. The estimated life of SHB is thus necessarily not correct. To get a better approximation it should have been measured with strain gauge while driving. Then it would have been interesting to implement a digital twin and monitor the situation. From this it could be scaled up, and a much more precise fatigue prediction in FEDEM[11] could have been utilized.

The stiffness of SHB during deceleration has been slightly reduced, the effect of this is not known. However, the deflection caused by bump is reduced on the new design. Is it noticeable when driving at all? By doing real testing with the SHB on a Multistrada, the drivability could have been compared.

As mentioned before, the SHB is fatigue calculated based on the "*after stress relief, machined and polished*" S-N curve (Figure 0.32) from (Uzan et al., 2017). Therefore it is necessary to add some extra material in critical areas when 3D-printing so that after post-processing, there is enough material. This has not been included in the final design but is an important factor to consider. Screws directly in aluminum threads often cause problems where the bolt cuts the treads. It should therefore be used HELICOILS[12], which improves thread strength for aluminum (Springer India New, 2014). This means that the drilled hole needs to meet dimension requirements for HELICOIL holes for M8 bolts.

The prices calculated in chapter 2.4.1 are only used as a guideline and are probably way off from what prices Ducati could have arranged if it were to be made ten thousand parts. Yet AM is an expensive manufacturing method, and prices vs. needs must be considered.

It has been made many assumptions in this thesis, and all of them have been on the "safe side". This may result in an over-dimensioned SHB, yet the weight was reduced by 36 %. With experiments and measurements on a Multistrada, the load scenarios could have been more accurate, the center of gravity would have been correct, and the load history for the fatigue calculations would have been a lot more precise. Then outcome from this thesis would have been different, most likely an even lighter SHB. All these values are known for Ducati, and with the process and method from this thesis, they can achieve a more accurate, lighter and optimized design.

[11] A nonlinear finite element program
[12] Thread reinforcement for low-strength material

5.3 Conclusion

Four different TO tools capable of optimizing the steering arrangement for a motorcycle have been evaluated and compared in this thesis. By utilizing the same load scenario on closely the same design space, all four TO tools came up with different solutions. Not all TO tools showed that the result they presented was credible. When the TO result was compared to FE-analysis done on re-constructed models, it showed that NX came out on top. NX showed that the TO result was close to the result that the FE-analysis showed, and this proves that the TO results from NX are reliable. Chapter 3.2 and 4.1, Table 9, and Appendix C answer to the evaluation of TO tools.

Two different reversed engineering tools were evaluated. NX realize shape was both faster and easier to use. The necessary modification after the verification analysis was effortless and quick to perform compared to SW. However, it was not as accurate as SW, but it was fast, and by iterations the accuracy was enhanced. Chapter 3.3 answer to this evaluation.

The SHB shows that it is achievable to make lighter and strong enough components with a fatigue limit of at least 1 million km for the motorcycle industries with the help of AM and TO. Even AlSi10Mg with such low mechanical properties can be utilized in critical components.

Through chapters 3 and 4, Appendix B, Appendix C Appendix D Appendix E , all objectives from chapter 1.1 are satisfied.

Further work:

To be able to print this steering arrangement, more investigation in the LBM method is necessary. Scanning speed, scanning pattern, laser power, the support size. At least consult with a manufacturer. Find out how much more material is needed in the critical areas to be able to machine, grind, and polish the surface smooth and not compromising the strength of the component. If the desired dimensions lay at least on the lower tolerance band in Figure 0.1 (Appendix A), the post-processing only removes the sharp edges. This counts for regions with higher stresses.

To achieve 100 % correct result, it is recommended to do testing and measuring on a driving Multistrada and collect data to estimate maximum loads and load history for fatigue prediction. The fatigue prediction can be made in FEDEM.

Including the steering head base would have been interesting, then a lot more weight could have been reduced.

References

AMPOWER. 2019. *Estimate your AM part cost in a first screening phase* [Online]. AMPOWER. Available: am-power.de/calculator/ [Accessed 01.12 2019].

BAGHERIFARD, S., BERETTA, N., MONTI, S., RICCIO, M., BANDINI, M. & GUAGLIANO, M. 2018. On the fatigue strength enhancement of additive manufactured AlSi10Mg parts by mechanical and thermal post-processing. *Materials & Design,* 145**,** 28-41.

BANDYOPADHYAY, A. & BOSE, S. 2015. *Additive Manufacturing,* Hoboken, Taylor and Francis.

BHANAGE, A., KRISHNAN, P. & SUNDGE, R. 2015. Static and Fatigue Simulation of Telescopic Fork Suspension System Used For Motorcycle. *International Journal of Applied Engineering Research,* 10**,** 477.

CALIGNANO, F. 2014. Design optimization of supports for overhanging structures in aluminum and titanium alloys by selective laser melting. *Materials & Design,* 64**,** 203-213.

CHRISTENSEN, P. W., KLARBRING, A. & GLADWELL, G. M. L. 2008. *An Introduction to Structural Optimization,* Dordrecht, Dordrecht: Springer Netherlands.

CORNO, M., SAVARESI, S. M., TANELLI, M. & FABBRI, L. 2008. On optimal motorcycle braking. *Control Engineering Practice,* 16**,** 644-657.

COSSALTER, V. 2006a. *Motorcycle Dynamics* Vittore Cossalter.

COSSALTER, V. 2006b. *Motorcycle Dynamics Ch. 5.2.1*, Vittore Cossalter.

DAHLVIG, G. & CHRISTENSEN, S. 1984. *Konstruksjonselementer,* [Oslo], Yrkesopplæring.

DEBROY, T., WEI, H. L., ZUBACK, J. S., MUKHERJEE, T., ELMER, J. W., MILEWSKI, J. O., BEESE, A. M., WILSON-HEID, A., DE, A. & ZHANG, W. 2018. Additive manufacturing of metallic components – Process, structure and properties. *Progress in Materials Science,* 92**,** 112-224.

DOWNLING, N. E. 2012. *Mechanical Behavior of Materials - Engineering Methods for Deformation, Fracture and Fatigue*, Pearson.

DUCATI. 2019. *Multistrada 1260 S* [Online]. Ducati. Available: https://www.ducati.com/ww/en/bikes/multistrada/multistrada-1260 [Accessed 12.09 2019].

DUCATI. 2020a. *Multistrada* [Online]. Ducati. Available: https://www.ducati.com/gb/en/bikes/multistrada/multistrada-1260 [Accessed 24. April 2020].

DUCATI, B. P. 2020b. *Bike Parts Ducati* [Online]. Available: https://www.bike-parts-ducati.com/ducati-motorcycle/Multistrada/2019/Multistrada_1260_S_ABS/Multistrada-1260-S-ABS/FRONT-FORK-STEM--TRIPLE-CLAMPS/394/2318/0/394 [Accessed 05.27 2020].

FOALE, T. 2006. *Motorcycle Handling and Chassis Design - The art and science*.

HAN, Q., GU, H., SOE, S., SETCHI, R., LACAN, F. & HILL, J. 2018. Manufacturability of AlSi10Mg overhang structures fabricated by laser powder bed fusion. *Materials & Design,* 160**,** 1080-1095.

HARTVIGSEN, H. 1994. *Verkstedhåndboka: mekaniske fag,* [Oslo], Yrkesopplæring i samarbeid med Norges standardiseringsforbund.

HERZOG, D., SEYDA, V., WYCISK, E. & EMMELMANN, C. 2016. Additive manufacturing of metals. *Acta Materialia,* 117**,** 371-392.

HUANG, R., RIDDLE, M., GRAZIANO, D., WARREN, J., DAS, S., NIMBALKAR, S., CRESKO, J. & MASANET, E. 2016. Energy and emissions saving potential of additive

manufacturing: the case of lightweight aircraft components. *Journal of Cleaner Production,* 135**,** 1559-1570.
HÄLLGREN, S., PEJRYD, L. & EKENGREN, J. 2016. (Re)Design for Additive Manufacturing. *Procedia CIRP,* 50**,** 246-251.
INSIGHTS, A. 2017. Additive Maufacturing MAKE og BUY? *An overview of todays's supplier market and cost structure for metal AM parts.* AMPOWER.
MALEKIPOUR, E. & EL-MOUNAYRI, H. 2018. Common defects and contributing parameters in powder bed fusion AM process and their classification for online monitoring and control: a review. *The International Journal of Advanced Manufacturing Technology,* 95**,** 527-550.
MASKERY, I., ABOULKHAIR, N., TUCK, C., WILDMAN, R., ASHCROFT, I., EVERITT, N. & HAGUE, R. 2015. *Fatigue Performance Enhancement of Selectively Laser Melted Aluminium Alloy by Heat Treatment*.
MATTHEW, M. 2017. Generative Design: What it is? How is it being used? Why it's a game changer. *KnE Engineering,* 2.
MILEWSKI, J. O. 2017. *Additive Manufacturing of Metals: From Fundamental Technology to Rocket Nozzles, Medical Implants, and Custom Jewelry,* Cham, Springer International Publishing, Cham.
SAMES, W. J., LIST, F. A., PANNALA, S., DEHOFF, R. R. & BABU, S. S. 2016. The metallurgy and processing science of metal additive manufacturing. *International Materials Reviews,* 61**,** 315-360.
SCHMIDT, M., MERKLEIN, M., BOURELL, D., DIMITROV, D., HAUSOTTE, T., WEGENER, K., OVERMEYER, L., VOLLERTSEN, F. & LEVY, G. N. 2017. Laser based additive manufacturing in industry and academia. *CIRP Annals,* 66**,** 561-583.
SINCLAIR, G. B., J. R. BEISHEIM, AND S. SEZER. 2006. Practical convergence-divergence checks for stresses from FEA.
SPRINGER INDIA NEW, D. 2014. Bollhoff Fastenings — Value-Based Engineering. *Auto Tech Review,* 3**,** 56-59.
TINGSTAD 1998. Teknisk katalog.
TOOLBOX, E. 2004. *Friction and Friction Coefficients* [Online]. Available: https://www.engineeringtoolbox.com/friction-coefficients-d_778.html [Accessed].
UHLMANN, E., KERSTING, R., KLEIN, T. B., CRUZ, M. F. & BORILLE, A. V. 2015. Additive Manufacturing of Titanium Alloy for Aircraft Components. *Procedia CIRP,* 35**,** 55-60.
UZAN, N. E., SHNECK, R., YEHESKEL, O. & FRAGE, N. 2017. Fatigue of AlSi10Mg specimens fabricated by additive manufacturing selective laser melting (AM-SLM). *Materials Science and Engineering: A,* 704**,** 229-237.
VANDENBROUCKE, B. & KRUTH, J. P. 2007. Selective laser melting of biocompatible metals for rapid manufacturing of medical parts. Bradford, England :.

Appendix

Appendix A : Common defects for LBM and EBM

Appendix B : Load scenarios for TO and FE-analysis

Appendix C : Result from TO compared with FE- analysis

Appendix D : Life prediction

Appendix E : FE-analysis on OEM part

Appendix F : Material Datasheet for AlSi10Mg and Al 6061-T6

Appendix A – Common defects for LBM and EBM

Geometric inaccuracy

Staircase effect is an example of what could lead to geometric inaccuracy defects. The curve of the surface results in staircase. Ticker layers cause a larger staircase effect. Staircase, results in sharp edges that could lead to a crack initiation point. Figure 0.1 shows how geometric defects could be (Malekipour and El-Mounayri, 2018).

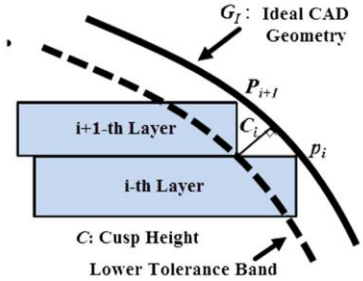

Figure 0.1 - Staircase effect

Dimensional inaccuracy

There are a lot of contributing parameters that lead to dimensional inaccuracy. Thermal shrinkage and sintering shrinkage are two of them. Sintering shrinkage is caused by densification, and thermal shrinkage is caused by cyclic heating from the next layer (Malekipour and El-Mounayri, 2018). Slumping can also occur with unsuitable dimensions. Slumping is a defect caused by gravity when the molten pool is too large for the position and the molten pool sags. This can happen on design features such as thin walls, downward facing surfaces, or overhangs. Undercutting is also a flaw that is caused by gravity. This is when molten metal is drawn away from the edge of the pool surface, leaving an underfilled region that has sharp edges that may act as a stress riser or crack initiation point (Milewski, 2017).

Surface roughness

Many parameters can cause a rough surface, some reason is powder depositions, pits, cracks, fracture, and staircase effect (Malekipour and El-Mounayri, 2018).

Balling

Balling is caused by energy density, contained gas of chamber, the rate of cooling, powder effect, plateaus' coefficient, and poor wetting (Malekipour and El-Mounayri, 2018). Balling is when balls are created on the surface, see Figure 0.2 (Sames et al., 2016).

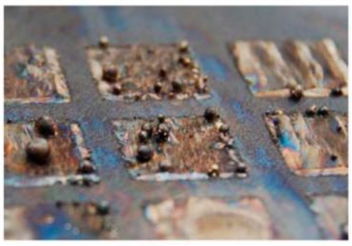

Figure 0.2 - Close up picture of balling

Surface deformation

Distortion and warping are types of surface deformation caused by heat. Warping means that the form is bending, and the result is deformed. Distortion are other types of changes, not necessarily on the form (Malekipour and El-Mounayri, 2018).

Surface oxidation

Surface oxidation is caused by contaminated powder or printing chamber. The use of gasses such as Argon, is used to prevent this (Malekipour and El-Mounayri, 2018).

Anisotropy and Heterogeneity

The mechanical properties of 3D printed parts are not necessarily isotropic. The tracing direction and layer orientation affect the strength, elongation, and other mechanical properties. Moreover, this can cause defects. The powder quality is vital for the density homogeneity (Malekipour and El-Mounayri, 2018).

Porosity (poor density)

Porosity or poor density is when not all the desired powder is melted, and it causes cavity. It can also happen when gases such as hydrogen are being entrapped underneath the molten pool and cause a pocket with no material. Several things cause porosity, laser power, scan speed, spot size, scan strategy, entrapped gas, and powder size are some of them (Malekipour and El-Mounayri, 2018).

Fracture/cracks and holes

These are defects that lead to weaker mechanical properties. Caused by the design or other defects (Malekipour and El-Mounayri, 2018).

Bonding between layers

Delamination and lack of fusion are common defects where the deposit does not fully melt into the former layers; these are shown in Figure 0.3 (Milewski, 2017). The layer thickness is one of the reasons that this could happen. Smaller layers will increase the re-melted substrate between the layers, which results in higher bonding (Malekipour and El-Mounayri, 2018).

Low strength

Several defects affect the strengthening of the 3D print. Some are the powder specification, trace pattern, and gas flow. The powder specification is directly connected to the grain size, which again is connected to the hardness of the material.

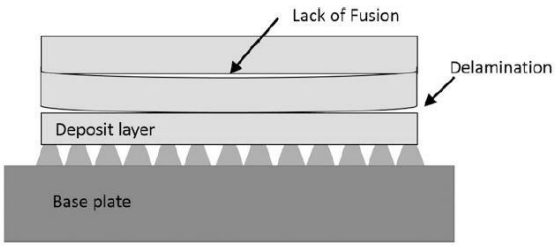

Figure 0.3 – Defects, delamination and lack of fusion in AM (Milewski, 2017)

Appendix B – Load Scenarios for TO and FE-analysis

In this appendix, all loads are described. External load from maximum braking and lateral displacement in the steering arrangement are the main forces and are used in the TO. Other load scenarios described in this appendix are used in FEM-analysis and fatigue prediction.

External Load from Braking and Lateral Displacement

From Motorcycle Dynamics by Vittore Cossalter, we have eq.(8): *"The maximum deceleration, expressed in g's, is proportional to the longitudinal distance from the center of the gravity to the contact point of the front wheel and is inversely proportional to the height of the center of the gravity"(Cossalter, 2006a).*

$$\frac{\ddot{x}_{max}}{g} \leq -\frac{(p-b)}{h} \tag{8}$$

It is also necessary to take aerodynamic resistance force F_D into account, to have a more conservative solution. F_D is given by eq. (9), and the equilibrium equation of the horizontal forces is given by eq. (10) where F is the total braking force.

$$F_D = \frac{1}{2}\rho A C_D V^2 \tag{9}$$

$$m\ddot{x} = -F - F_D \tag{10}$$

Then the maximum deceleration depends on both the mass and the velocity.

$$\frac{\ddot{x}_{max}}{g} \leq -\frac{(p-b)}{h} - \frac{\frac{1}{2}\rho A C_D V^2}{mg} \tag{11}$$

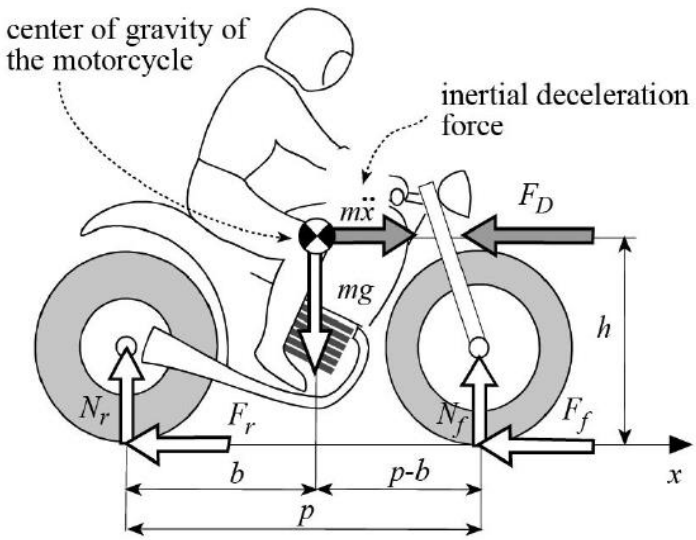

Figure 0.4 - Motorcycle under braking, from Motorcycle dynamics

The wheelbase is 1 585 mm and with a 50/50 weight distribution.

Table 15 - Values that are crucial for maximum deceleration and acceleration

(p-b) *	792.5 mm
h *	792.5 mm
m	235 kg
ρ	1.167 kg/m^3
V	200 km/h = 55.5 m/s
C_DA **	0.5 m^2

*: Presumed values, **: Value from Motorcycle Dynamics

$$\frac{\ddot{x}_{max}}{g} \leq -\frac{792.5\ mm}{792.5\ mm} - \frac{\frac{1}{2} * 1.167\frac{kg}{m^3} * 0.5\ m^2 \left(55.55\frac{m}{s}\right)^2}{235\ kg * 9.81\frac{m}{s^2}} = -1.39 \tag{12}$$

This means that the maximum deceleration possible from 200 km/h is 1.39 G; this is the flip over limit with zero loads on the rear wheel and is set to be the dimensioning factor. Even the best drivers will find it hard to brake at the limit point at this speed.

With a driver and passenger of 75 kg each, the total mass on the motorcycle is 150 kg. Because of the instability and wobbling caused by braking with straight arms, drivers keep most of their own mass of pinching their legs against the fuel tank. Almost nothing will go through the handlebar. However, to be conservative, 75 % of the mass has been estimated to go through the handlebar. Then the dimensional load will be

$$F_H = 0.75 * 150\ kg * 9.81\frac{m}{s^2} * 1.39\ g = 1\ 534\ N \tag{13}$$

For forces caused by lateral displacement, the weight distribution presumed to be 50/50. The total weight on the front wheel is given by

$$m_{t.f} = \frac{235\ kg\ +\ 75\ kg}{2}\ =\ 155\ kg \tag{14}$$

From *Motorcycle Handling and Chassis Design* (Foale, 2006), a simulation case is done, and a graph (Figure 0.5) is made. A motorcycle in 100 km/h hits a 25 mm bump. The graph in Figure 0.5 shows that this case will result in an acceleration of approximately 18 Gs with normal tire and suspension.

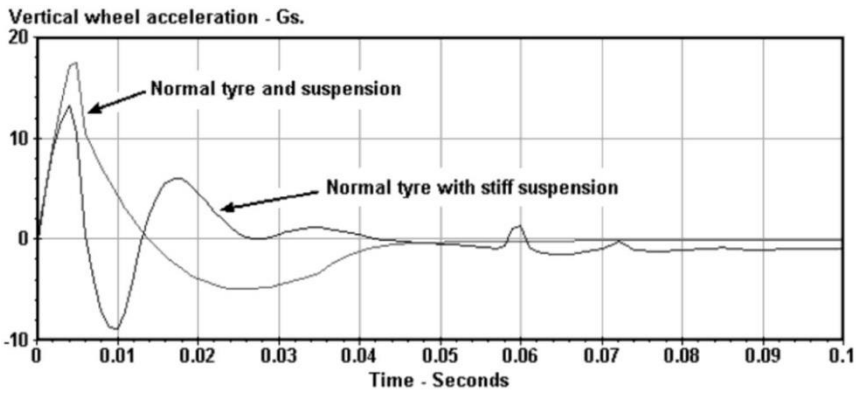

Figure 0.5 - Front-wheel vertical acceleration

In the calculation of the force exerted on the suspension, this is rounded up to 20 Gs since in the assumption, the bike hits the bump in a corner. Then the vertical acceleration is tilted as much as the roll angle of the

motorcycle, and that results in less force trough the suspension forks, which again results in a harder impact. Due to the lateral displacement, it is assumed that all loads end up in the suspension clamps.

With a triple tree steering arrangement, the suspensions are clamped four places. For simplicity, it is presumed that all four clamps take up the same amount of force. Then we have

$$\frac{155\ kg\ *\ 9.81\ {}^{m}/_{s^2}\ *\ 20}{4} =\ 7\ 602\ \ N \tag{15}$$

If the TO were to be completed with the asymmetric load scenario, which is the case from the lateral displacement, the result would also be asymmetric. The displacement can happen in two directions, and therefore if the asymmetric load scenario is chosen, two cases must be considered. Another approach is that the symmetric load scenario is considered, which results in a symmetric optimized solution. Then the asymmetric load scenario must be evaluated with FEM-analyses afterward.

To maintain the symmetry, both forks must be exposed to the force in the same direction. A quick model of the triple tree has been analyzed to see which case exposes the steering head with more significant stress. The results are shown in Figure 0.6. The maximum stress on both solutions are the same and located on the steering head base. The maximum stress in the steering head for the tension case is 41 MPa, and the compressed case is 44 MPa. It is a minimal difference, and since the triple tree model and the analysis was simplified, either one could be used for the TO. The compressed case was chosen.

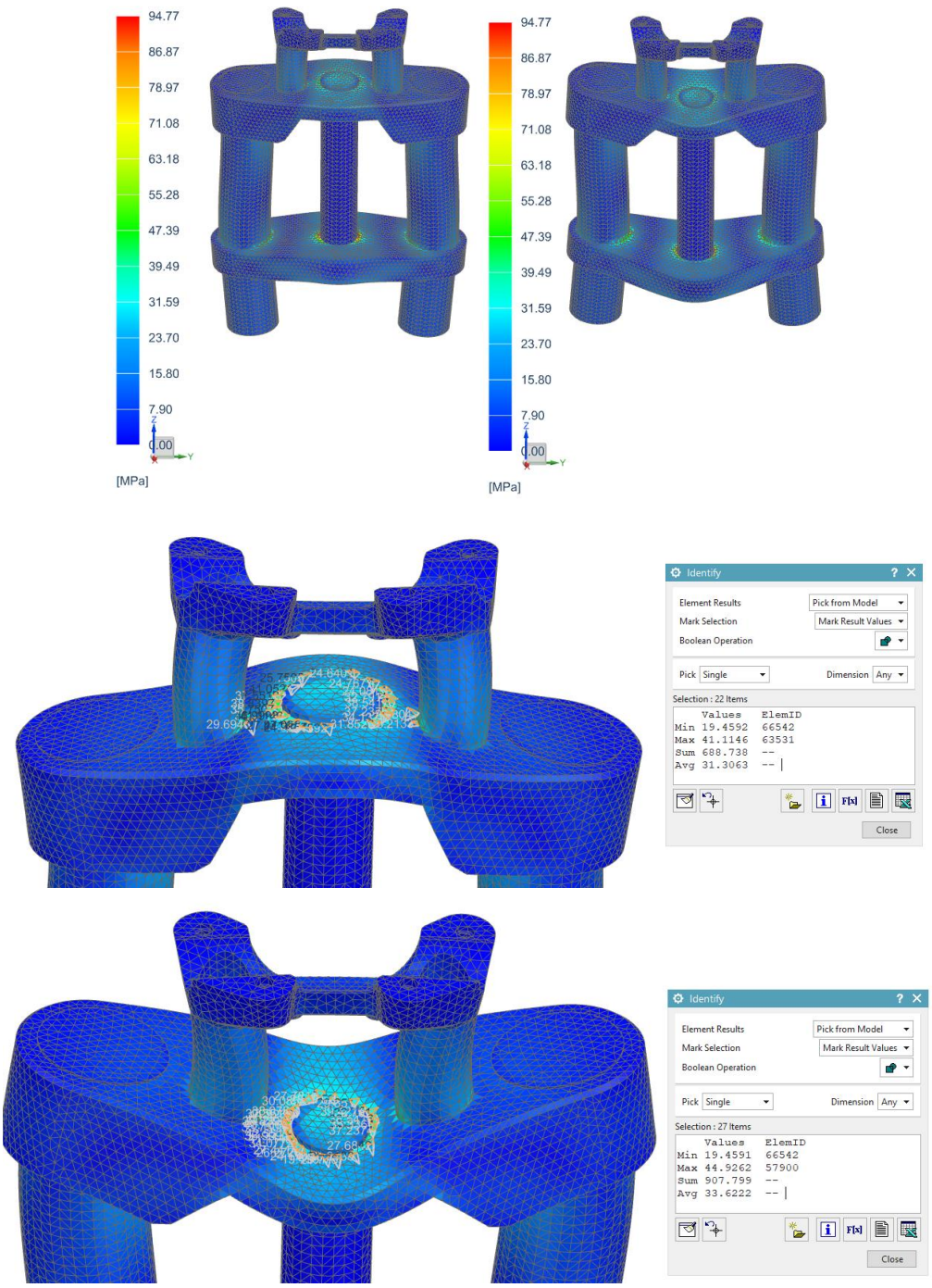

Figure 0.6 - Triple tree simulation

External Load from Acceleration

Wheeling-limited acceleration is achieved when the load on the front wheel N_f is equal to zero. See eq.(16) and Figure 0.7.

$$N_f = g * m * \frac{b}{p} - S * \frac{h}{p} = 0 \tag{16}$$

From which we have maximum acceleration:

$$\ddot{x}_{max} = g * \frac{b}{h} - \frac{F_D}{m} \tag{17}$$

With a velocity of 0 m/s, F_D in eq.(17) is equal zero, and that part of the equation is neglected. With the presumed dimensions in Table 15 insert in eq. (18) we have:

$$\ddot{x}_{max} = 9.81 \ {}^{m}/_{s^2} * \frac{792.5\ mm}{792.5\ mm} = 9.81 \ {}^{m}/_{s^2} \tag{18}$$

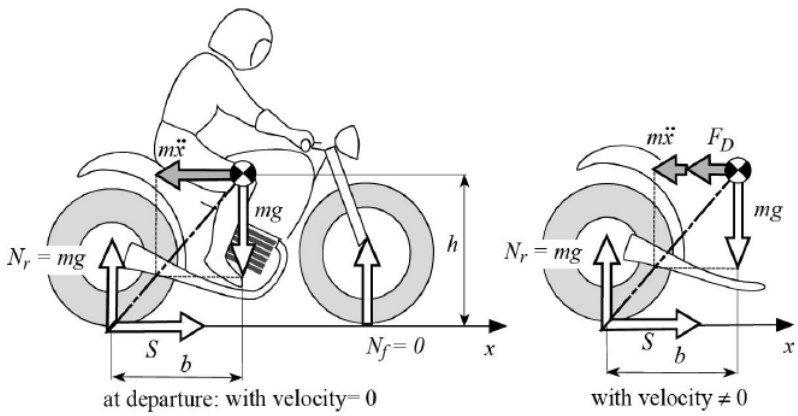

Figure 0.7 - Acceleration limited by wheelie, from motorcycle dynamics.

Under normal acceleration conditions, the contributed mass from the driver is only a fraction of the driver's whole mass. For a conservative solution, the load is set to the driver's weight multiplied with maximum acceleration. This gives:

$$F_a = 75\ kg * 9.81 \ {}^{m}/_{s^2} = 735.8\ N \approx 740\ N \tag{19}$$

Internal Loads

These bolts will be lubricated, which results in less friction, and the relation between tightening torque and tensile load will be stronger.

From Dahlvig and Christensen (Dahlvig and Christensen, 1984) we have

$$M = M_v + M_s \tag{20}$$

Where M is the total torque, M_v is the torque caused by the friction in the threads. M_v is described

$$M_v = F * r_m * tan(\varphi + \varepsilon_1) \tag{21}$$

where r_m is the threads mean radius, ε_1 and φ are described in eq. (22) and (23).

$$\varepsilon_1 = \frac{\mu}{cos(\alpha)} \tag{22}$$

$$tan(\varphi) = \frac{P}{\pi * d_2} \tag{23}$$

μ is the friction coefficient in the threads, and α is half the thread angel. P is the thread pitch, and d_2 is the threads mean diameter.

M_s is the torque caused by the friction on the contact surface under the bolt head and is described in eq. (24).

$$M_s = \mu' * F * r'_m \tag{24}$$

μ' is the friction coefficient between the bolt head and contact face, and r'_m are the radius that the friction force will occur, shown in eq.(25).

$$r'_m = \frac{Outer\ diameter\ bolt\ head\ +\ diameter\ hole}{4} \tag{25}$$

In Table 16, we find the value that has been used for the calculation. Values with * comes from "Verkstedshåndboka" (Hartvigsen, 1994), and ** comes from Tingstad Technical Catalog (Tingstad, 1998).

Table 16 - Values for the tensile load calculation

	Values	
d_2	7,19 mm	*
P	1,25 mm	*
α	30 °	*
r_m	3,595 mm	
r'_m	5,375 mm	
μ	0,1	**
μ'	0,1	**

Inserting eq. (21) and (24) into (20) and isolate F we have

$$F = \frac{M}{(tan(\varphi + \varepsilon_1) * r_m + \mu' * r'_m)} \tag{26}$$

which is the tensile load that will be the critical and dimensional load for this handlebar. The eq. (26) gives F = 22 740 N, and this will be used as pre-load in the bolts.

A certain pressure occurs between HBU, HHL, and the handlebar. This pressure lies on the surface between these parts. The area of this surface is essential so that the right pressure allowance is maintained.

Steering Torque

Figure 0.8 shows a variation in steering torque that the rider needs to apply to the handlebar. At low speed, the steering torque can be negative. This means that the rider must block the handlebar. At high speed and tight corners, the torque increase. In this figure, the highest torque is 12 Nm; we can imagine that the handlebar and SHB does not experience torque much higher than this. This toque is not included in any simulations or calculations, because it would not be decisive. This figure is obtained from Motorcycle Dynamics (Cossalter, 2006a).

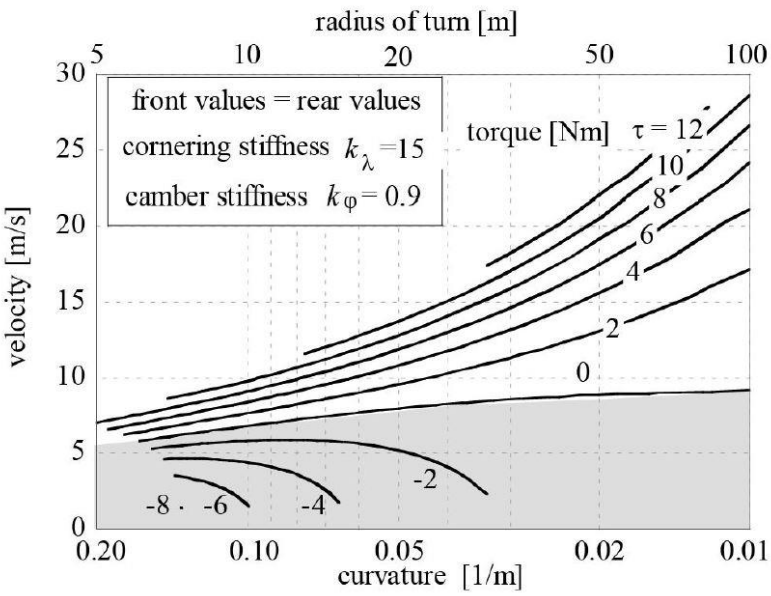

Figure 0.8 - Steering torque for a motorcycle in a turn

Appendix C – Result from TO compared with FE- analysis

The intention of this FE-analysis is to compare the results with the TO. The set-up from TO is not how the steering arrangement truly would experience these forces. The options in the TO set-up are minimal, and therefore some simplification was made. Simplification is done in all load and constraint regions. First, the load from the handlebar is acting on the whole handlebar surface in the handlebar holder. Realistically the force would only act on the region of the surface that is in the load exerted direction, meaning that the handlebar only pushes and does not drag. Inside the suspension clamp, the load is placed on the whole surface in positive Z-direction, and no other restriction is added. The correct way includes restriction in rotation about X and Y-axis because of the stiffness in the suspension forks in these directions.

NX Topology Optimization for Designers

As Figure 0.9 shows are the approximated mass from NX TOD is 0.515 kg, and the Nastran solid properties check in Figure 0.12 shows that the mass is 0.546 kg, a deviation of 31 gram. Maximum stresses from NX TOD is approximated to be 167 MPa and are located in two regions, one in the suspension clamp transition and the other one in the headstock connection transition. In Figure 0.13, all elements with a stress of 167 MPa or higher is red on the re-constructed model. Due to a smoother transition to the suspension clamp, there is no stress concentration there. The maximum stress is shown in Figure 0.14, and this is 287 MPa. If the surface curvature-based size variation is moved to the left[13], then the maximum stress is reduced to 212 MPa. Checking for convergence requires tree sizes of mesh (Sinclair, 2006). By refining the mesh in the vulnerable region, the stress goes toward infinite high values, this is a sign of singularities, see Figure 0.15 and Figure 0.16. The singularity is ignored. The average stress of the neighbor elements is calculated to be 166 MPa see Figure 0.17.

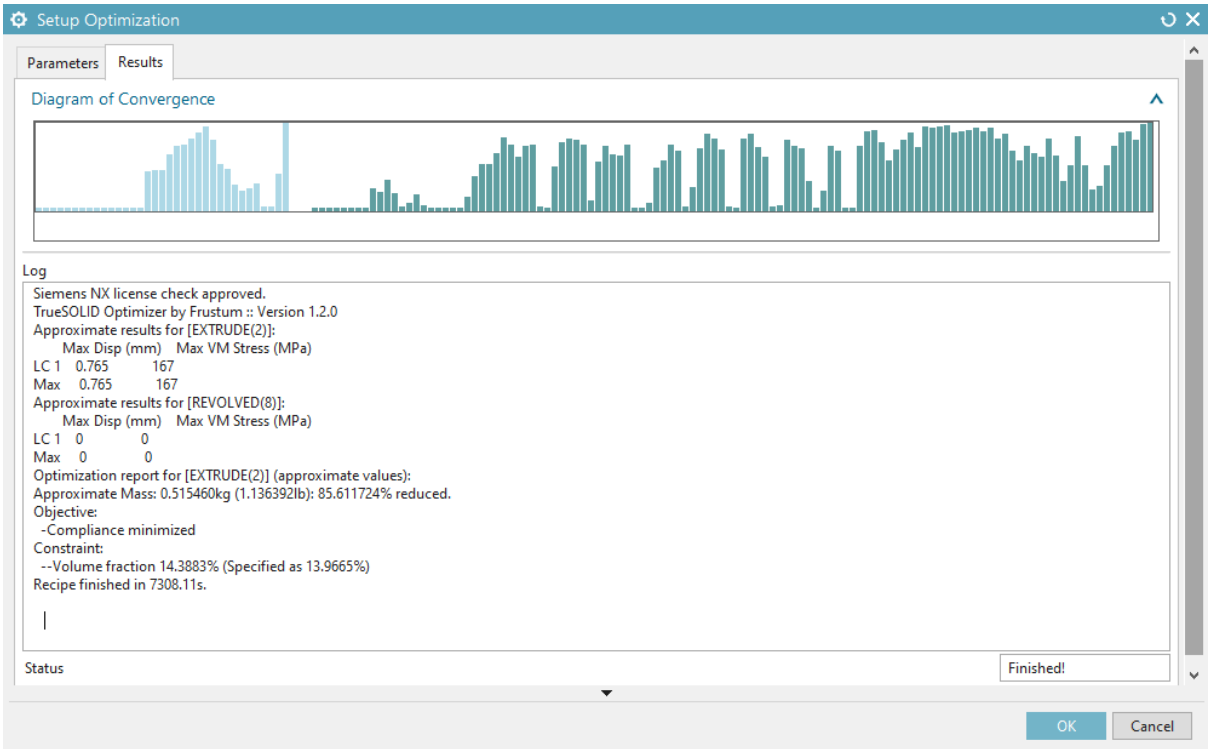

Figure 0.9 - NX TOD result and convergence diagram.

[13] Mesh setting in NX Nastran. Increases the size of elements in areas of surface with a high amount of curvature

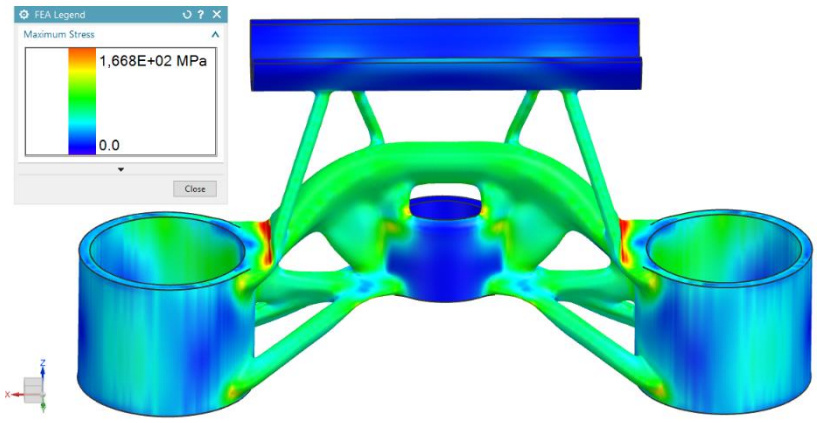

Figure 0.10 - Result NX TOD. The transition between the suspension clamp and struts are exposed. Hints of stresses in the transition between the headstock connection ring and struts.

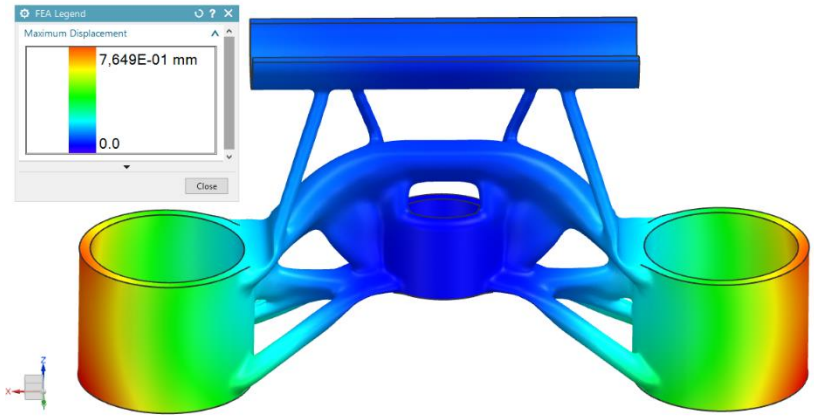

Figure 0.11 - Result NX TOD. Maximum displacement in the suspension clamps.

```
-------------------------------------------------------------

                    Simcenter Nastran SOLID PROPERTIES

-------------------------------------------------------------


Total Length (1D elements): 0.000000E+00 mm
Total Area (2D elements) : 0.000000E+00 mm²
Volume                   : 2.043623E+05 mm³


Total Mass               : 5.456474E-01 kg
```

Figure 0.12 – NX TOD. Solid properties check of the re-constructed CAD.

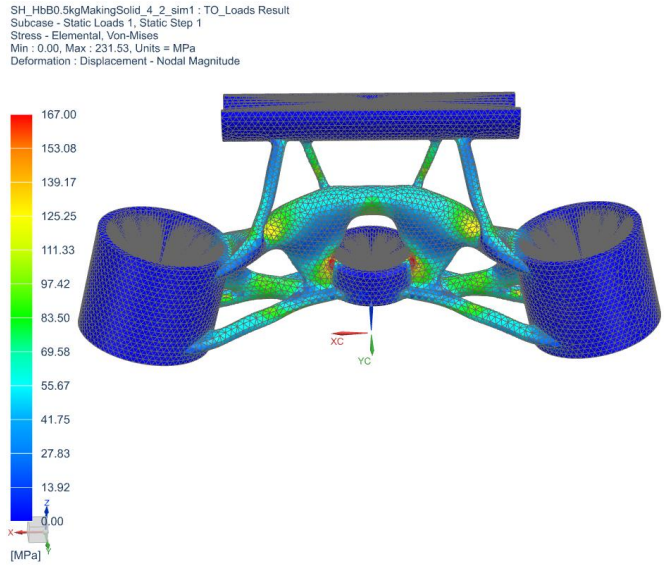

Figure 0.13 - NX TOD re-constructed model with 167 MPa legend limit

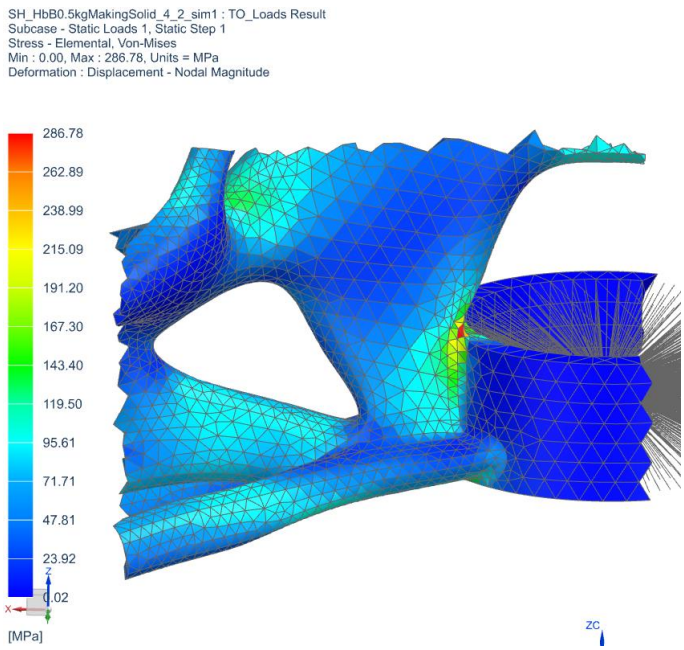

Figure 0.14 - NX TOD re-constructed model maximum stress.

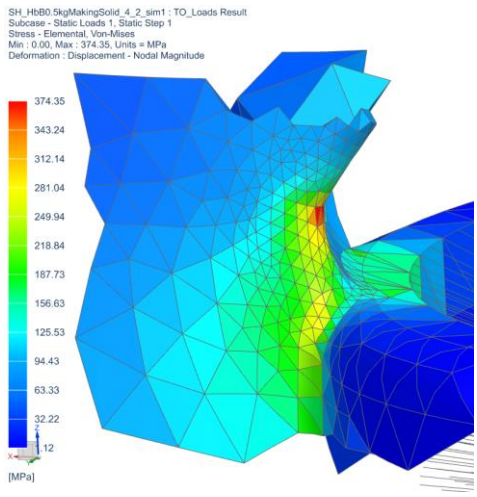

Figure 0.15 - NX TOD re-constructed model convergence check medium mesh.

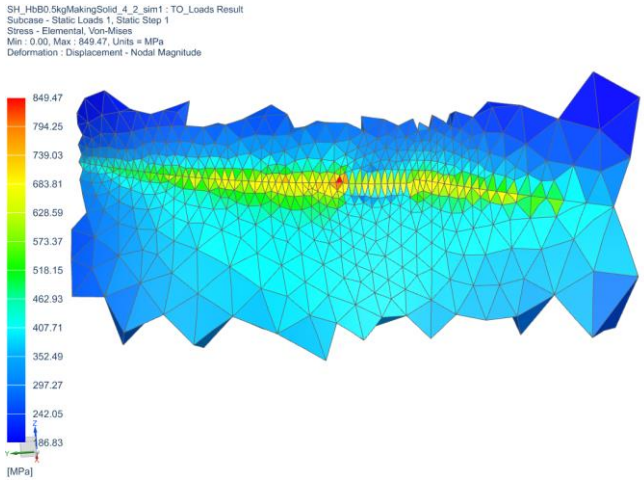

Figure 0.16 - NX TOD re-constructed model convergence check fine mesh.

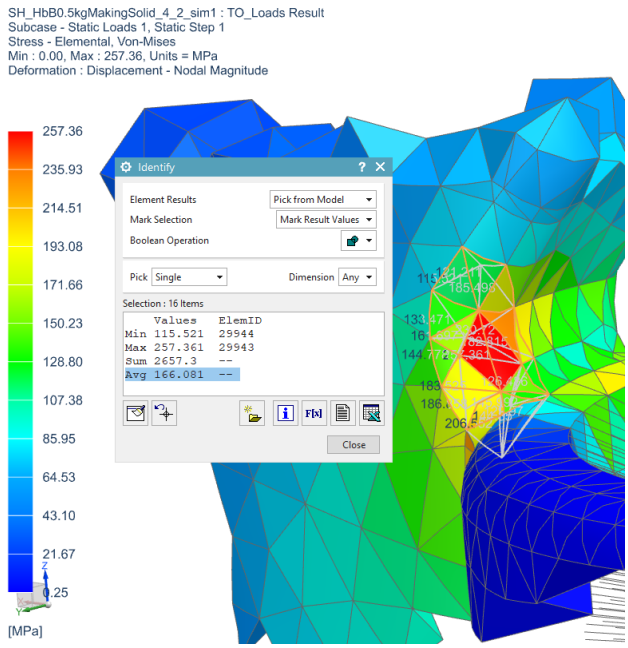

Figure 0.17 - NX TOD re-constructed model average stress.

Figure 0.11 and Figure 0.18 shows that the maximum displacement is located on the lower side of the suspension clamp. NX TOD approximates the maximum displacement to be 0.76 mm, Figure 0.18 shows that this displacement is calculated to be 0.47 mm.

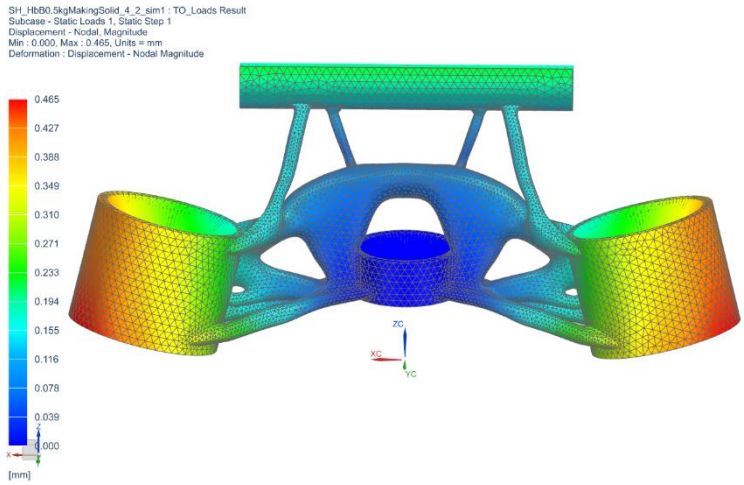

Figure 0.18 - NX TOD re-constructed model maximum displacement.

Fusion360

In Figure 0.19 is the details Fusion360 gives after the TO. The mass is 0.516 kg, the stress is 240 MPa, and the maximum displacement is 1.18 mm. In Figure 0.21, the solid properties check of the exported model is shown. Fusion360 does not have a clear and readable legend, it only indicates high, low, and ideal stresses, see Figure 0.20. Figure 0.22 shows the comprehensive situation with a maximum stress of 339 MPa, Figure 0.23 shows a close up of the maximum stressed element. A further investigation in this region was done, and the maximum element seems to be a singularity. This singularity is ignored, and the maximum stress is then concluded to be 228 MPa, see Figure 0.24. The maximum displacement is calculated to be 0.78 mm and are in the handlebar holder, see Figure 0.25. The stress and displacement seem to be lower than specified from the TO result.

Properties	
Status	Converged
Material	Aluminum AlSi10Mg
Orientation	Z+
Manufacturing method	Additive
Visual similarity	Ungrouped
Production volume (pcs.)	10000
Estimated manufacturing cost	
Range (USD)	247 - 363
Median (USD)	321
Volume (mm^3)	1.933e+5
Mass (kg)	0.516
Max von Mises stress (MPa)	240
Factor of safety limit	1
Min factor of safety	1
Max displacement global (mm)	1.18
Cost estimates powered by **äPriori**	

Figure 0.19 - Fusion360 TO result

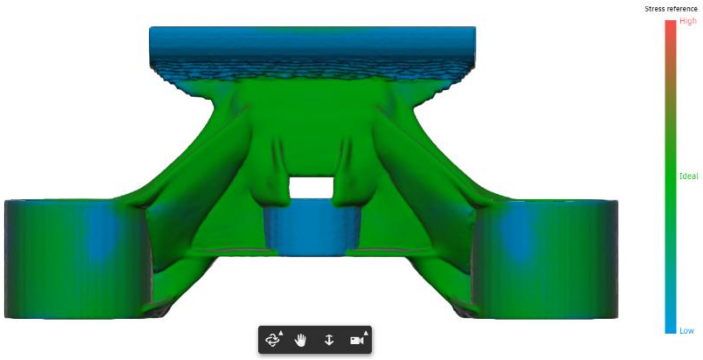

Figure 0.20 - Fusion360 Stress indication

```
------------------------------------------------------------

                    Simcenter Nastran SOLID PROPERTIES

------------------------------------------------------------


Total Length (1D elements): 0.000000E+00 mm
Total Area (2D elements) : 0.000000E+00 mm²
Volume                   : 1.872965E+05 mm³


Total Mass               : 5.000815E-01 kg
```

Figure 0.21 - Fusion360. Solid properties check for the exported CAD.

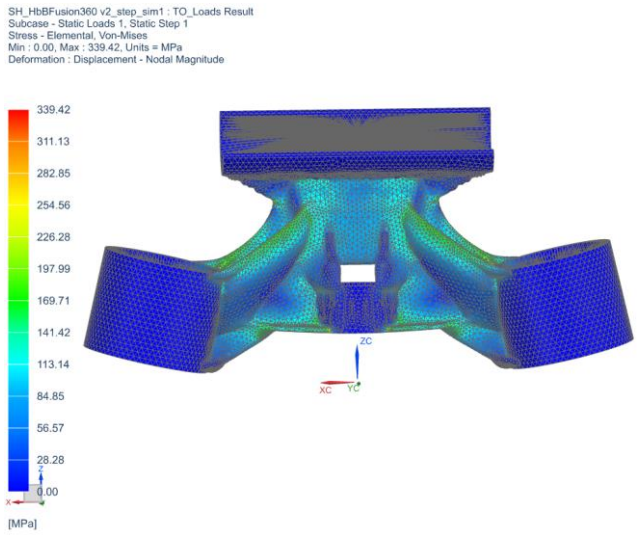

Figure 0.22 - Fusion360 Stress on the exported CAD.

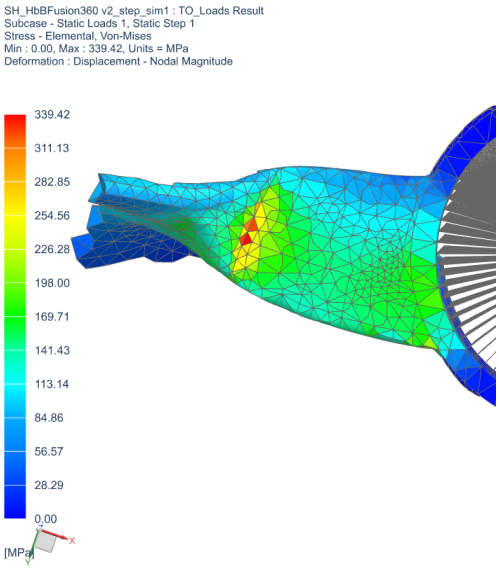

Figure 0.23 - Fusion 360 close up of stress

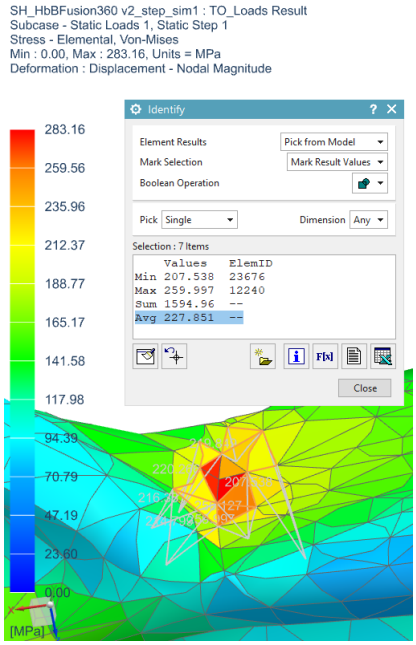

Figure 0.24 - Fusion360 average stress

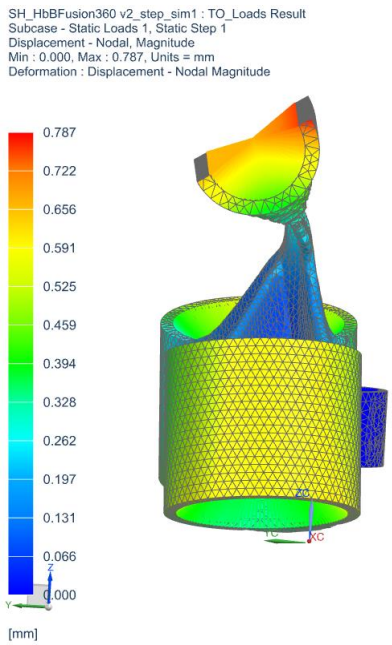

Figure 0.25 - Fusion360 maximum displacement.

SolidWorks

SW often removes material that is critical to maintaining the structural stiffness in the part. Figure 0.26 shows that the material between the handlebar holder and the steering head is missing. The SHB is fixed constrained in the headstock connection ring, forces in positive Z-direction in both suspension clamps, and the last force is in the handlebar holder points in Y-direction minus 25°. With this material missing, this part has no stiffness. The part will have infinite displacement. It was decided to do no further investigation on the SW result.

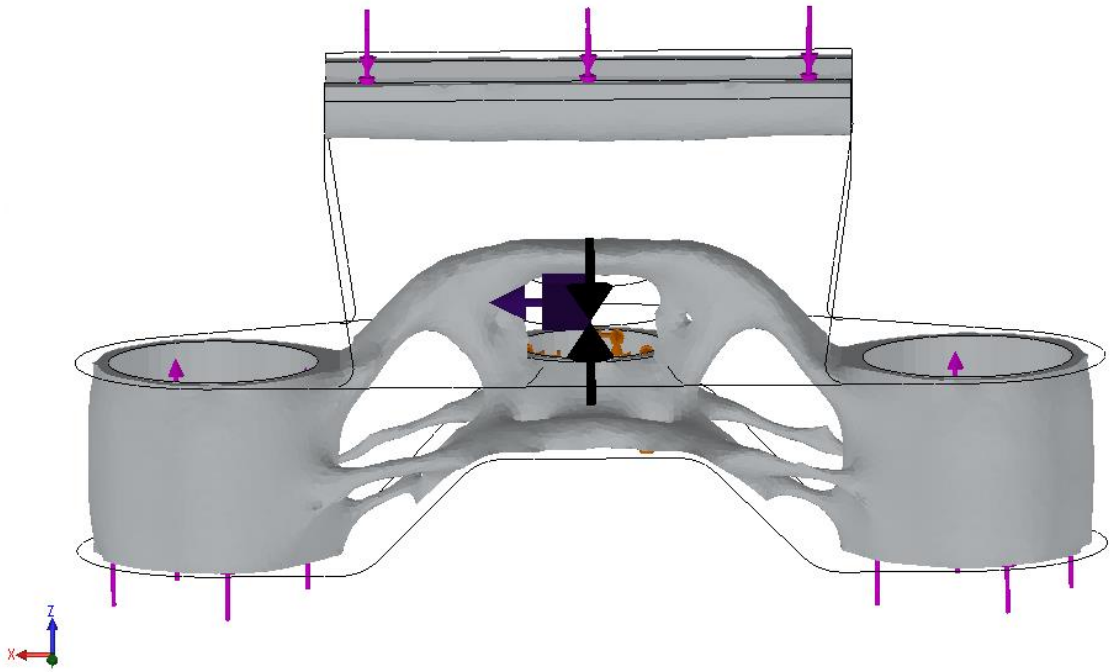

Figure 0.26 - Result from SW. Material missing between critical regions.

Abaqus

The design space in Abaqus was half the size, and a planar symmetry was utilized in the optimization. This was done to save time. Therefore, the weight goal was also roughly halved and was set to 0.26 kg. Figure 0.27 shows that the result of this optimization was close to 0.26 kg. When mirroring this, the total weight is 0.52 kg. The maximum stress of 637 MPa is shown in Figure 0.28 and Figure 0.29. This was investigated and concluded to be a singularity. Then the maximum stress is 385 MPa.

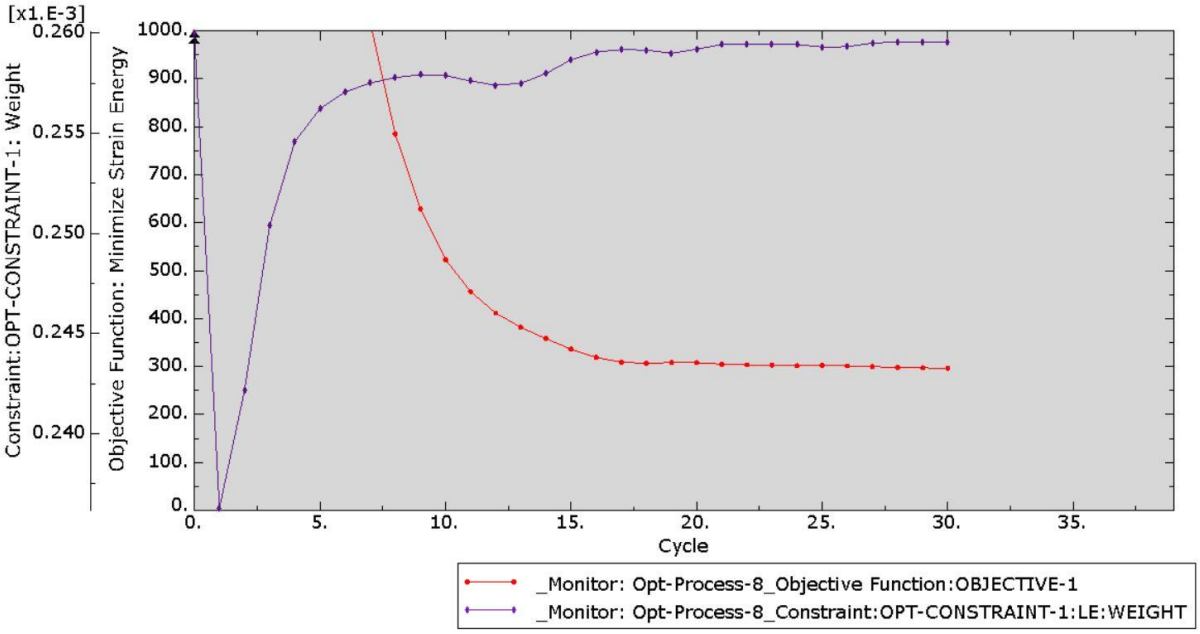

Figure 0.27 - Convergence diagram from Abaqus results

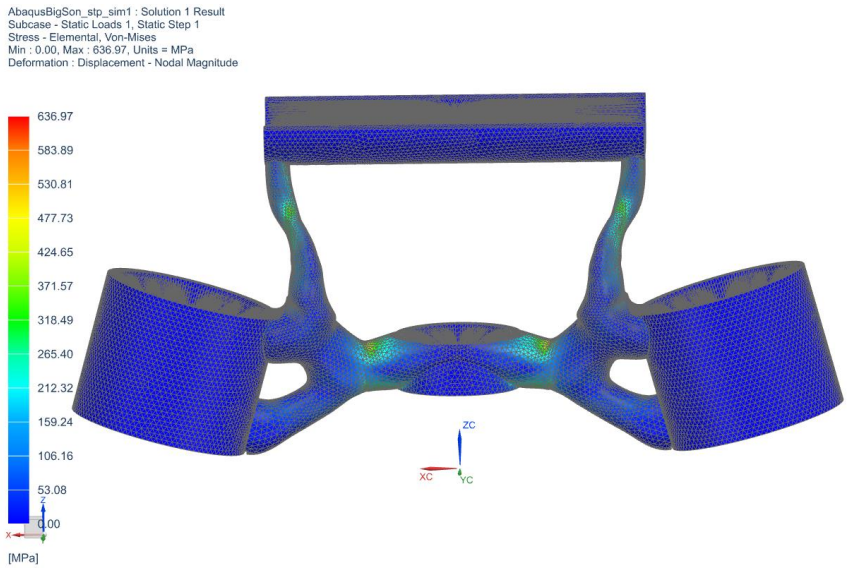

Figure 0.28 - Abaqus maximum stress re-constructed model.

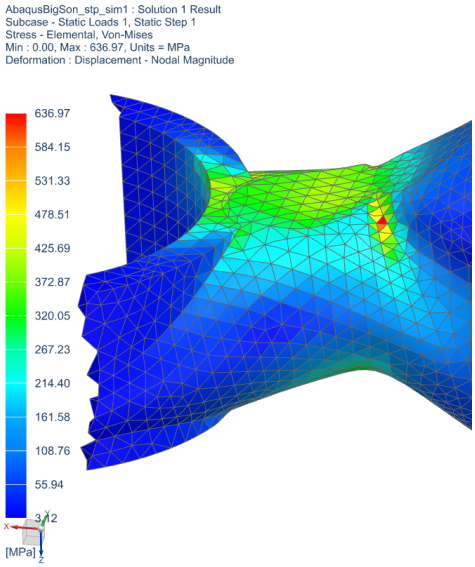

Figure 0.29 - Abaqus close up maximum stress re-constructed model.

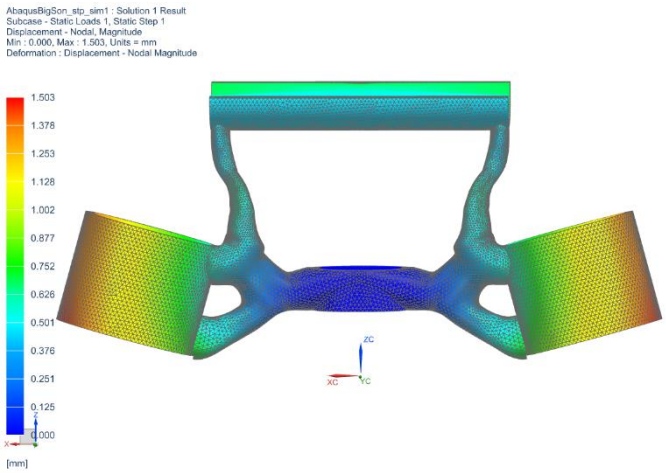

Figure 0.30 - Abaqus maximum displacement re-constructed model.

```
-------------------------------------------------------------

                    Simcenter Nastran SOLID PROPERTIES

-------------------------------------------------------------


Total Length (1D elements): 0.000000E+00 mm
Total Area (2D elements) : 0.000000E+00 mm²
Volume                   : 2.311078E+05 mm³


Total Mass               : 6.170578E-01 kg
```

Figure 0.31 - Solid properties check of re-constructed model from Abaqus

The maximum stress and displacement are too high. The weight goal was set to 0.520 kg, and the actual weight was 0.617 kg, see Figure 0.31, which is a deviation of 97 grams. Some of this deviation can be because of not 100 % correct CAD re-construction.

Short Summary

NX TOD gives reliable results from the TO. There is some small deviation in the maximum displacement. The deviation in weight is 31 grams. This difference can be a result of not 100 % correct re-build of the STL.

Fusion360 TO result does not indicate where the maximum displacement is located. It is rather difficult to see where the maximum stress is located as well. The maximum stress from the re-constructed model is close to the yield strength of the material. The weight deviation from TO result to NX solid properties check is 16 grams. This can be a result of the split and mirror operation of the exported solid.

SolidWorks was not investigated due to poor TO results.

For Abaqus, the stress was above the yield strength of the material.

Appendix D – Life Prediction

All equations used in this appendix comes from Mechanical Behavior of Materials[14](Downling, 2012).

From eq. (13) and (19) in Appendix B (Max. accel. load and max decel. load) loads from deceleration and acceleration are calculated for different fractions and are listed in Table 17.

Table 17 - Load caused by accelerations and decelerations from 10 to 100 %

	Acceleration		*Deceleration*	
	Load, [N]	Weight, [kg]	Load, [N]	Weight, [kg]
100 %	740	75.4	1534	156.4
80 %	592	60.3	1227	125.1
60 %	444	45.3	920	93.8
40 %	296	30.2	614	62.5
30 %	222	22.6	460	46.9
20 %	148	15.1	307	31.3
10 %	74	7.5	153	15.6

The highest stresses for acceleration and deceleration are in the transition corners between the headstock ring and the struts. Even if SHB and the load scenario are symmetric, there were some deviations on maximum stress around the part. In Table 18, stresses in all four corners for all acceleration and deceleration situations are listed. Left back corner seen from driver side has the average highest stress and is used to predict the life of SHB.

Table 18 - Stresses in the transition corner between the headstock ring and the struts during acceleration and deceleration. Positive stress for tension and negative stress for compression.

		Left back corner stress, [MPa]	*Right back corner stress, [MPa]*	*Left front corner stress, [MPa]*	*Right front corner stress, [MPa]*
Deceleration	100 %	184	180	-140	-145
	80 %	148	148	-115	-115
	60 %	110	115	-84	-87
	40 %	85	80	-56	-58
	30 %	60	57	-42	-44
	20 %	40	36	-28	-29
	10 %	21	20	-14	-14
Acceleration	100 %	-97	-96	66	67
	80 %	-80	-80	52	55
	60 %	-56	-59	39	39
	40 %	-39	-37	26	27
	30 %	-27	-29	19	20
	20 %	-19	-19	12	13
	10 %	-9	-10	6	7
	SUM	975	966	699	720

It is important to keep in mind that in eq. (13) 75 % of the drivers and passengers load goes through the handlebar. With average driving in a correct driving position, 10-15 % of only the driver's load goes through the handlebar. That is around 150 – 200 N compared to 1 534 N. When calculating the fatigue limit of the SHB, most load cycles due to deceleration are around 150 – 500 N, or 10-30 %. For simplicity, 30 % of maximum acceleration is used in every cycle. The complete load history is shown in Figure 0.34.

[14] Chapter 9. Fatigue of Materials: Introduction and Stress-Based Approach

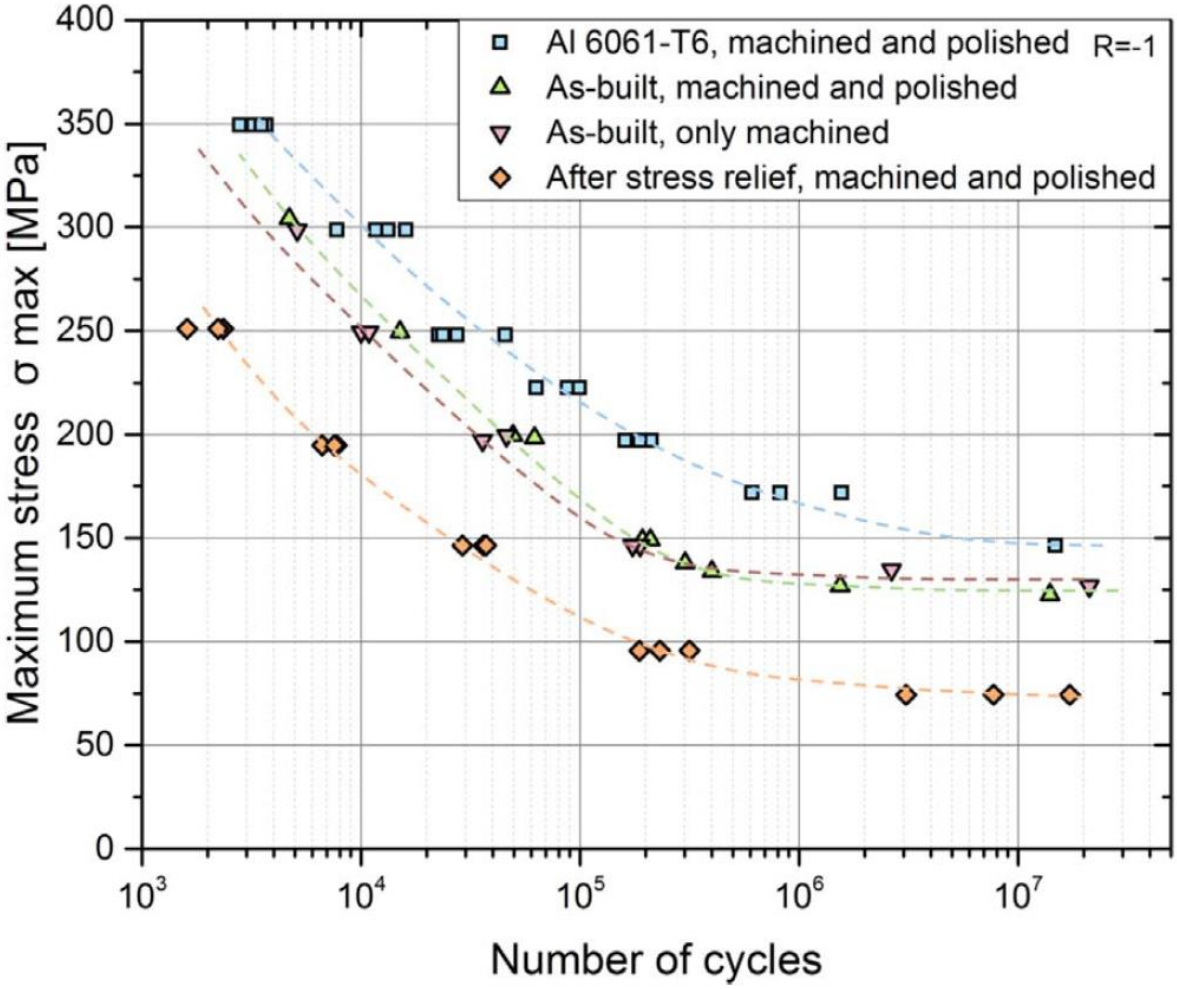

Figure 0.32 - S-N curve for AlSi10Mg printed with EOSINT M-280.

S-N curve is obtained from a Science Direct article (Uzan et al., 2017). A Moor rotating beam machine was used which means that the σ_m = 0, this gives:

$$\sigma_{max} = \sigma_m + \sigma_a \Rightarrow \sigma_{max} = \sigma_a \tag{27}$$

In Table 19, values from the diamond (orange) S-N curve in Figure 0.32 are listed, and in Figure 0.32, these are plotted on a log-log scale. The four first point seems to lay in a straight line and the most conservative one. Point 1 and 4 represents this line well and are used to calculate constant A and B from eq.(28).

Table 19 - Values from S-N curve

	σ_a – [MPa]	N_f - Cycles
1	250	2500
2	194	7000
3	150	25000
4	100	175000
5	80	3000000

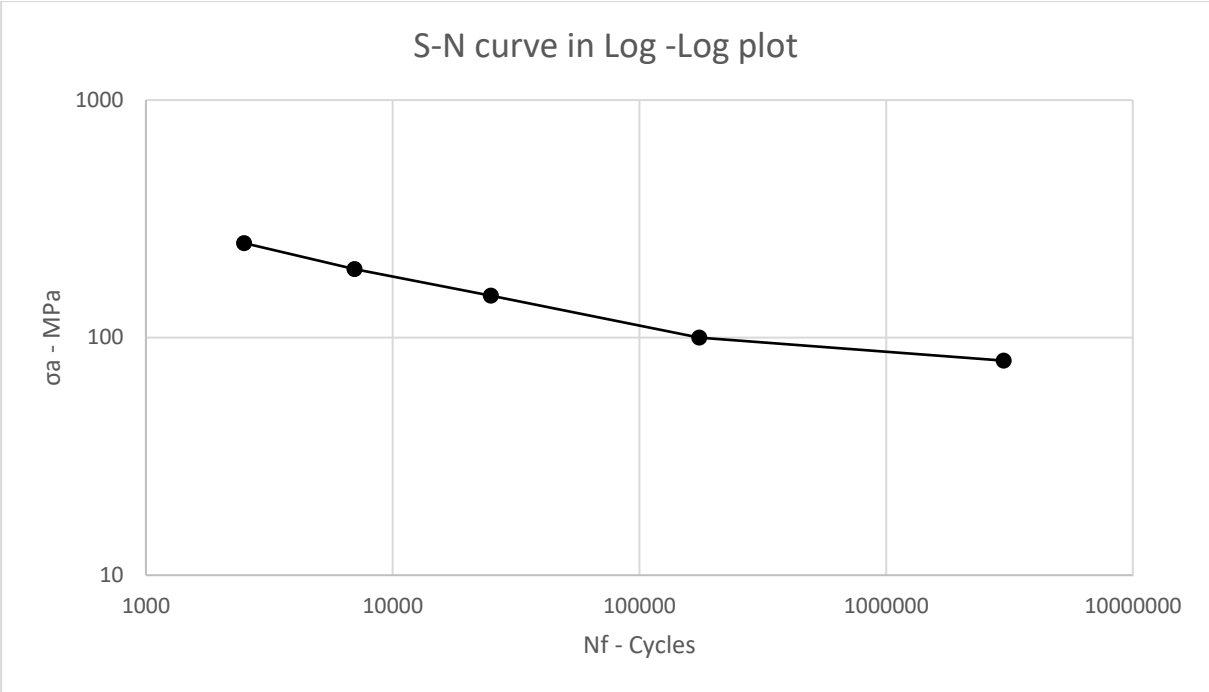

Figure 0.33 - S-N curve in log-log plot

$$\sigma_1 = AN_1^B \quad , \ \sigma_2 = AN_2^B \tag{28}$$

By dividing the second equation on the first and take logarithms of both sides, then solving for B, we have eq.(29).

$$B = \frac{log\sigma_1 - log\sigma_2}{logN_1 - logN_2} = \frac{log(250) - log(100)}{log(2500) - log(175000)} = -0.2157 \tag{29}$$

Now A is solved from eq.(28)

$$A = \frac{\sigma_1}{N_1^B} = \frac{250\ MPa}{2500^{-0.2157}} = 1351.7\ MPa \tag{30}$$

B is equal to b, and then from eq.(31) we have eq.(32)

$$\sigma_a = \sigma'_f\ (2N_f)^b \tag{31}$$

$$A = 2^b\sigma'_f \Rightarrow \sigma'_f = \frac{A}{2^b} = \frac{1351.7\ MPa}{2^{-0.2157}} = 1569.7\ MPa \tag{32}$$

Smith, Watson, and Topper (SWT) equation is a good fit for aluminum alloys (Downling, 2012), and by solving that for N_f, and substitute σ_{max} with $\sigma_m + \sigma_a$ we have

$$N_f = \frac{1}{2}\left(\frac{\sigma_m + \sigma_a}{\sigma'_f}\sqrt{\frac{1 - R}{2}}\right)^{\frac{1}{b}} \tag{33}$$

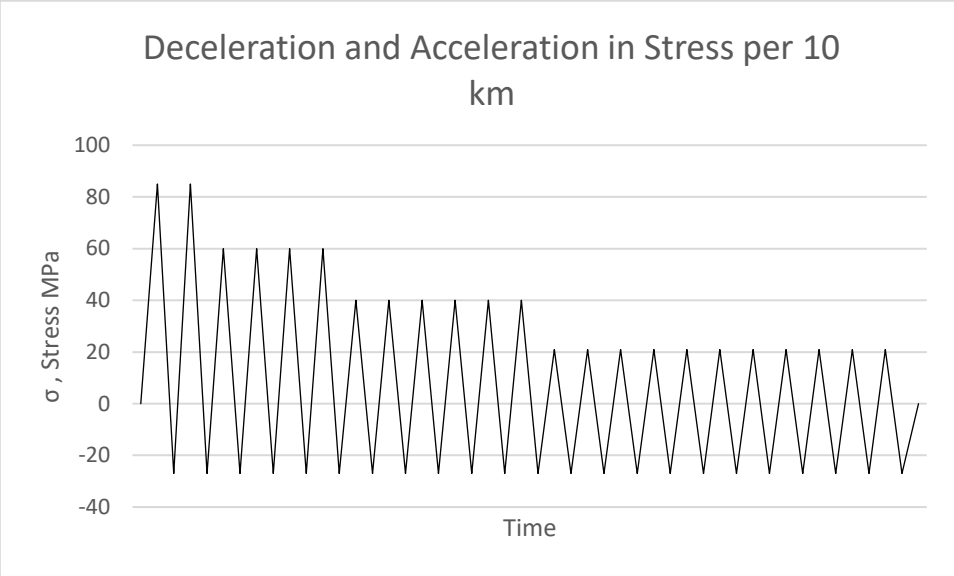

Figure 0.34 - A presumed stress history per 10 km.

Use Table 20 as an overview of the stresses and cycles.

Table 20 – Summary table of required values for Palmgren-Miner rule

j	N_j	σ_{min}	σ_{max}	σ_a	σ_m	N_{fj}	N_j / N_{fj}
100 %	0,002	-27	184	105,5	78,5	10.355	1,9E-07
80 %	0,01	-27	148	87,5	60,5	28.413	3,5E-07
60 %	0,1	-27	110	68,5	41,5	112.450	8,9E-07
40 %	2	-27	85	56	29	371.601	5,4E-06
30 %	4	-27	60	43,5	16,5	1.867.945	2,1E-06
20 %	6	-27	40	33,5	6,5	12.238.699	4,9E-07
10 %	10	-27	21	24	-3	242.714.619	4,1E-08
						Σ =	9,5E-06

By solving the repetitions to failure from eq.(7)(Palmgren-Miner rule) we have

$$B_f = \frac{1}{\sum\left(\frac{N_j}{N_{fj}}\right)} = \frac{1}{9{,}5E - 06} = 105.263 \tag{34}$$

This limit is for 10 km, which means that the fatigue limit for SHB is 1.052.630 km.

Appendix E - FE-analysis on OEM part

The same load scenarios as in FEM verification (chapter 4.2) on the SHB are used on OEM parts, except FEA-2.

Note: The global coordinate system does not follow the part, it follows the motorcycle. This means that the coordinate system is rotated the rake angle of 25° about the Y-axis. That means that X-direction points in the driving direction.

The material used in both parts is Al 6061-T6.

OEM FEA-1 - Maximum deceleration and bumps

CTETRA(10) elements with a size of 2 mm have been used on the steering head and HHL. In each suspension clamp, an RBE2 element is placed, the surface follows the master node. Such an element is also placed in the center of the handlebar holder and in the center of the headstock connection hole. For simplicity, there has not been established a bolted connection between these parts. Between the two parts, four RBE2 elements have been utilized (Yellow in Figure 0.35). Two on each connection point. Two RBE2 elements for HHL and two for the steering head. Between one HHL RBE2 element and one steering head RBE2 element, it has been established a third element. This simulates that there is no gap between these two parts. The gap will then be infinite stiff. Realistically the stiffness would have been the same as the in pipe, but this approach is close enough.

In Figure 0.35, the set-up of the OEM FEA-1 is illustrated. The load of 1 534 N on the HHL caused by maximum deceleration points in X-direction. In the left suspension clamp, the bump load of 7 602 N points in the positive Z-direction and the same load points in negative Z-directing for the right one. The RBE2 element in the headstock connection hole is fully fixed. The RBE2 elements in the suspension clamps are restricted to rotate about the X and Y -axis due to the stiffness in the suspension fork would not allow it.

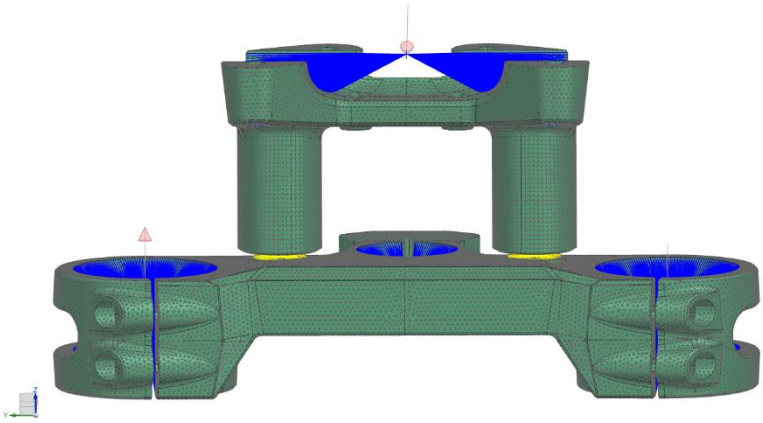

Figure 0.35 - OEM FEA-1 set-up

Result OEM FEA-1

Maximum stress is 603 MPa in one single element in an inside corner. The neighbor elements have an average stress of around 400 MPa. The maximum displacement was 1.3 mm in the suspension clamp. The stress result is shown in Figure 0.36 and displacement in Figure 0.37.

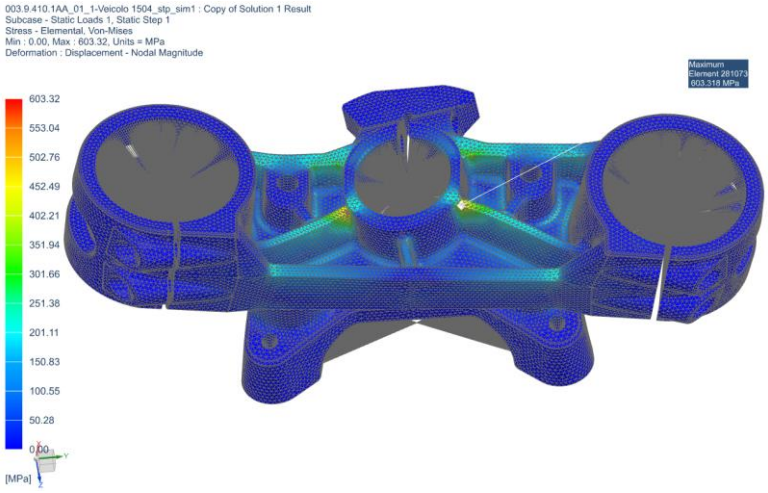

Figure 0.36 - Result OEM FEA-1

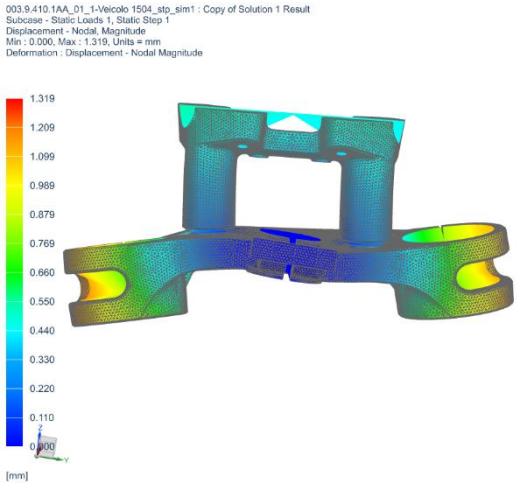

Figure 0.37 - Displacement OEM FEA-1. Visually exaggerated 10 %.

OEM FEA-3 – Maximum deceleration

This set-up is identical to OEM FEA-1 except for the bump loads in the suspension clamps.

Result OEM FEA-3

The highest stress with maximum deceleration is only 70 MPa, see Figure 0.38. Maximum displacement, as seen in Figure 0.39, was 0.15 mm on the edge of HHL.

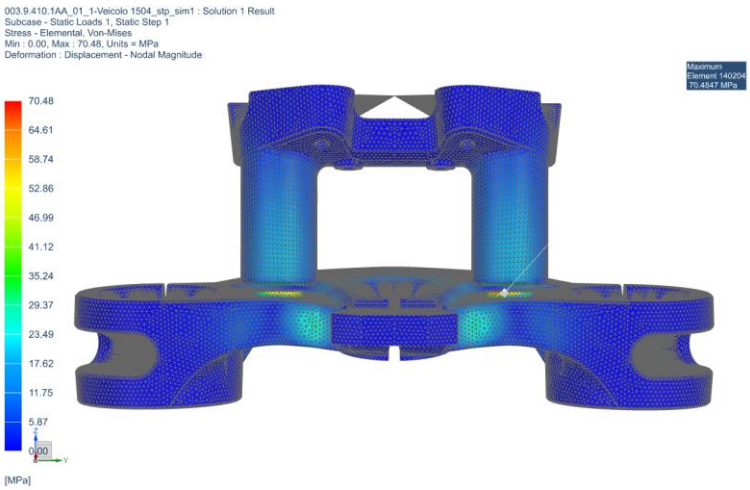

Figure 0.38 - Result OEM FEA-3

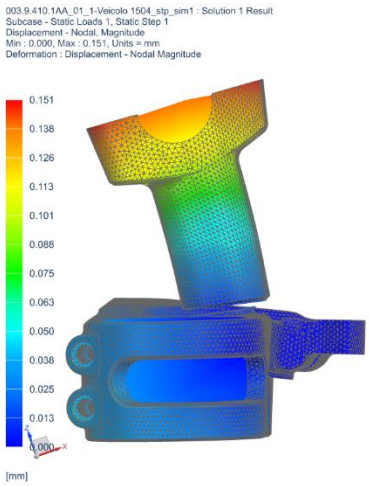

Figure 0.39 - Displacement OEM FEA-3. Visually exaggerated 10 %.

OEM FEA-4 – Maximum acceleration

The difference for this analysis compared to OEM FEA-3 is that the load is reduced to 740 N and points in the opposite direction.

Result OEM FEA-4

The maximum stress of 34 MPa is shown in Figure 0.40. The maximum displacement is 0.07 mm in the edge of HHL, see Figure 0.41.

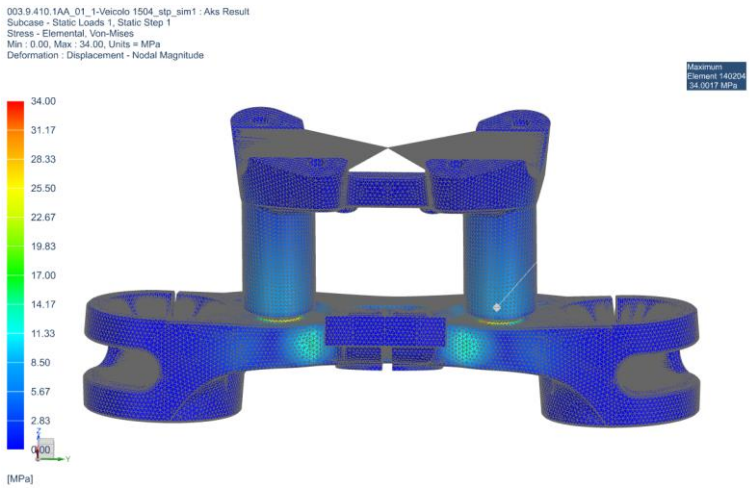

Figure 0.40 - Result OEM FEA-4

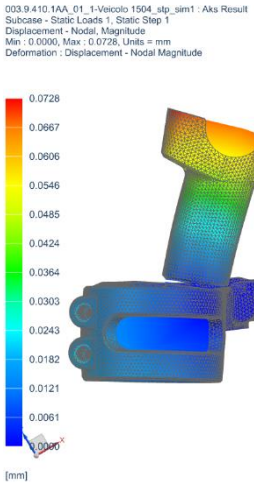

Figure 0.41 - Displacement OEM FEA-4. Visually exaggerated 10 %.

Appendix F - Material Datasheet for AlSi10Mg and Al 6061-T6

Material data sheet

EOS Aluminium AlSi10Mg

EOS Aluminium AlSi10Mg is an aluminium alloy in fine powder form which has been specially optimised for processing on EOSINT M systems

This document provides information and data for parts built using EOS Aluminium AlSi10Mg powder (EOS art.-no. 9011-0024) on the following system specifications:

- EOSINT M 280
  with PSW 3.6 and Original EOS Parameterset AlSi10Mg_Speed 1.0
- EOS M 290 400Watt
  with EOSPRINT 1.0 and Original EOS Parameterset AlSi10Mg_Speed 1.0

Description

AlSi10Mg is a typical casting alloy with good casting properties and is typically used for cast parts with thin walls and complex geometry. It offers good strength, hardness and dynamic properties and is therefore also used for parts subject to high loads. Parts in EOS Aluminium AlSi10Mg are ideal for applications which require a combination of good thermal properties and low weight. They can be machined, spark-eroded, welded, micro shot-peened, polished and coated if required.

Conventionally cast components in this type of aluminium alloy are often heat treated to improve the mechanical properties, for example using the T6 cycle of solution annealing, quenching and age hardening. The laser-sintering process is characterized by extremely rapid melting and re-solidification . This produces a metallurgy and corresponding mechanical properties in the as-built condition which is similar to T6 heat-treated cast parts. Therefore such hardening heat treatments are not recommended for laser-sintered parts, but rather a stress relieving cycle of 2 hours at 300 °C (572 °F). Due to the layerwise building method, the parts have a certain anisotropy, which can be reduced or removed by appropriate heat treatment - see Technical Data for examples.

EOS GmbH - Electro Optical Systems

Robert-Stirling-Ring 1
D-82152 Krailling / München

Telephone: +49 (0)89 / 893 36-0
Telefax: +49 (0)89 / 893 36-285
Internet: www.eos.info

Technical data

General process and geometrical data

Typical achievable part accuracy [1] [2]	± 100 µm
Smallest wall thickness [1] [3]	approx. 0.3 – 0.4 mm approx. 0.012 – 0.016 inch
Surface roughness, as built, cleaned [1] [4]	R_a 6 - 10 µm, R_z 30 - 40 µm R_a 0.24 - 0.39 x 10^{-3} inch R_z 1.18 - 1.57 x 10^{-3} inch
- after micro shot-peening	R_a 7 - 10 µm, R_z 50 - 60 µm R_a 0.28 - 0.39 x 10^{-3} inch R_z 1.97 - 2.36 x 10^{-3} inch
Volume rate [5]	7.4 mm^3/s (26.6 cm^3/h) 1.6 in^3/h

[1] These properties were determined on an EOSINT M 270.

[2] Based on users' experience of dimensional accuracy for typical geometries. Part accuracy is subject to appropriate data preparation and post-processing, in accordance with EOS training.

[3] Mechanical stability dependent on the geometry (wall height etc.) and application

[4] Due to the layerwise building, the surface structure depends strongly on the orientation of the surface, for example sloping and curved surfaces exhibit a stair-step effect. The values also depend on the measurement method used. The values quoted here given an indication of what can be expected for horizontal (up-facing) or vertical surfaces.

[5] The volume rate is a measure of the building speed during laser exposure. The overall building speed is dependent on the average volume rate, the time required for coating (depends on the number of layers) and other factors, e.g. DMLS settings.

EOS GmbH – Electro Optical Systems
Robert-Stirling-Ring 1
D-82152 Krailling / München

Physical and chemical properties of the parts

Material composition	Al (balance) Si (9.0 - 11.0 wt-%) Fe (≤ 0.55 wt-%) Cu (≤ 0.05 wt-%) Mn (≤ 0.45 wt-%) Mg (0.2 - 0.45 wt-%) Ni (≤ 0.05 wt-%) Zn (≤ 0.10 wt-%) Pb (≤ 0.05 wt-%) Sn (≤. 0.05 wt-%) Ti (≤ 0.15 wt-%)
Relative density	approx. 99.85 %
Density	2.67 g/cm³ 0.096 lb/in³

EOS GmbH - Electro Optical Systems
Robert-Stirling-Ring 1
D-82152 Krailling / München

Mechanical properties of the parts

	As built	Heat treated [9]
Tensile strength [6]		
- in horizontal direction (XY)	460 ± 20 MPa 66.7 ± 2.9 ksi	345 ± 10 MPA 50.0 ± 1.5 ksi
- in vertical direction (Z)	460 ± 20 MPa 66.7 ± 2.9 ksi	350 ± 10 MPa 50.8 ± 1.5 ksi
Yield strength (Rp 0.2 %) [6]		
- in horizontal direction (XY)	270 ± 10 MPa 39.2 ± 1.5 ksi	230 ± 15 MPa 33.4 ± 2.2 ksi
- in vertical direction (Z)	240 ± 10 MPa 34.8 ± 1.5 ksi	230 ± 15 MPa 33.4 ± 2.2 ksi
Modulus of elasticity		
- in horizontal direction (XY)	75 ± 10 GPa 10.9 ± 0.7 Msi	70 ± 10 GPa 10.2 ± 0.7 Msi
- in vertical direction (Z)	70 ± 10 GPa 10.2 ± 0.7 Msi	60 ± 10 GPa 8.7 ± 0.7 Msi
Elongation at break [6]		
- in horizontal direction (XY)	(9 ± 2) %	12 ± 2%
- in vertical direction (Z)	(6 ± 2) %	11 ± 2%
Hardness [7]	approx.119 ± 5 HBW	
Fatigue strength [1] [8]		
- in vertical direction (Z)	approx. 97 ± 7 MPa approx. 14.1 ± 1.0 ksi	

[6] Mechanical strength tested as per ISO 6892-1:2009 (B) annex D, proportional specimens, specimen diameter 5 mm, original gauge length 25 mm (1 inch).

[7] Hardness test in accordance with Brinell (HBW 2.5/62.5) as per DIN EN ISO 6506-1. Note that measured hardness can vary significantly depending on how the specimen has been prepared.

[8] Fatigue test with test frequency of 50 Hz, R = -1, measurement stopped on reaching 5 million cycles without fracture.

[9] Stress relieve: anneal for 2 h at 300 °C (572 °F).

[10] These properties were determined on an EOSINT M 280-400W. Test parts from following machine type EOS M 290-400W correspond with these data.

EOS GmbH - Electro Optical Systems
Robert-Stirling-Ring 1
D-82152 Krailling / München

Thermal properties of parts

	As built [1]	Heat treated [1] [9]
Thermal conductivity (at 20 °C)		
- in horizontal direction (XY)	approx. 103 ± 5 W/m°C	approx. 173 ± 10 W/m°C
- in vertical direction (Z)	approx. 119 ± 5 W/m°C	approx. 173 ± 10 W/m°C
Specific heat capacity		
- in horizontal direction (XY)	approx. 920 ± 50 J/kg°C	approx. 890 ± 50 J/kg°C
- in vertical direction (Z)	approx. 910 ± 50 J/kg°C	approx. 890 ± 50 J/kg°C

Abbreviations

approx. approximately
wt weight

Notes

The data are valid for the combinations of powder material, machine and parameter sets referred to on page 1, when used in accordance with the relevant Operating Instructions (including Installation Requirements and Maintenance) and Parameter Sheet. Part properties are measured using defined test procedures. Further details of the test procedures used by EOS are available on request.

The data correspond to our knowledge and experience at the time of publication. They do not on their own provide a sufficient basis for designing parts. Neither do they provide any agreement or guarantee about the specific properties of a part or the suitability of a part for a specific application. The producer or the purchaser of a part is responsible for checking the properties and the suitability of a part for a particular application. This also applies regarding any rights of protection as well as laws and regulations. The data are subject to change without notice as part of EOS' continuous development and improvement processes.

EOS®, EOSINT® and DMLS® are registered trademarks of EOS GmbH.

© 2014 EOS GmbH – Electro Optical Systems. All rights reserved.

EOS GmbH – Electro Optical Systems
Robert-Stirling-Ring 1
D-82152 Krailling / München

Aluminum 6061-T6; 6061-T651 (Unverified Data**)

Categories: Metal; Nonferrous Metal; Aluminum Alloy; 6000 Series Aluminum Alloy

Material Notes: General 6061 characteristics and uses: Excellent joining characteristics, good acceptance of applied coatings. Combines relatively high strength, good workability, and high resistance to corrosion; widely available. The T8 and T9 tempers offer better chipping characteristics over the T6 temper.

Applications: Aircraft fittings, camera lens mounts, couplings, marines fittings and hardware, electrical fittings and connectors, decorative or misc. hardware, hinge pins, magneto parts, brake pistons, hydraulic pistons, appliance fittings, valves and valve parts; bike frames.

Data points with the AA note have been provided by the Aluminum Association, Inc. and are NOT FOR DESIGN.

Composition Notes:
Composition information provided by the Aluminum Association and is not for design.

Key Words: al6061, UNS A96061; ISO AlMg1SiCu; Aluminium 6061-T6, AD-33 (Russia); AA6061-T6; 6061T6, ISO AlMg1SiCu; Aluminium 6061-T651, AD-33 (Russia); AA6061-T651; Al6061-T6

Vendors: **Click here to view all available suppliers for this material.**

Please click here if you are a supplier and would like information on how to add your listing to this material.

Physical Properties	Metric	English	Comments
Density	2.70 g/cc	0.0975 lb/in³	AA; Typical

Mechanical Properties	Metric	English	Comments
Hardness, Brinell	95	95	AA; Typical; 500 g load; 10 mm ball
Hardness, Knoop	120	120	Converted from Brinell Hardness Value
Hardness, Rockwell A	40	40	Converted from Brinell Hardness Value
Hardness, Rockwell B	60	60	Converted from Brinell Hardness Value
Hardness, Vickers	107	107	Converted from Brinell Hardness Value
Tensile Strength, Ultimate	310 MPa	45000 psi	AA; Typical
	24.0 MPa @Temperature 371 °C	3480 psi @Temperature 700 °F	
	32.0 MPa @Temperature 316 °C	4640 psi @Temperature 601 °F	
	51.0 MPa @Temperature 260 °C	7400 psi @Temperature 500 °F	
	131 MPa @Temperature 204 °C	19000 psi @Temperature 399 °F	
	234 MPa @Temperature 149 °C	33900 psi @Temperature 300 °F	
	290 MPa @Temperature 100 °C	42100 psi @Temperature 212 °F	
	310 MPa @Temperature 24.0 °C	45000 psi @Temperature 75.2 °F	
	324 MPa @Temperature -28.0 °C	47000 psi @Temperature -18.4 °F	
	338 MPa @Temperature -80.0 °C	49000 psi @Temperature -112 °F	
	414 MPa @Temperature -196 °C	60000 psi @Temperature -321 °F	
Tensile Strength, Yield	276 MPa	40000 psi	AA; Typical
	12.0 MPa @Strain 0.200 %, Temperature 371 °C	1740 psi @Strain 0.200 %, Temperature 700 °F	
	19.0 MPa @Strain 0.200 %, Temperature 316 °C	2760 psi @Strain 0.200 %, Temperature 601 °F	
	34.0 MPa @Strain 0.200 %, Temperature 260 °C	4930 psi @Strain 0.200 %, Temperature 500 °F	
	103 MPa @Strain 0.200 %, Temperature 204 °C	14900 psi @Strain 0.200 %, Temperature 399 °F	
	214 MPa @Strain 0.200 %, Temperature 149 °C	31000 psi @Strain 0.200 %, Temperature 300 °F	
	262 MPa @Strain 0.200 %, Temperature 100 °C	38000 psi @Strain 0.200 %, Temperature 212 °F	
	276 MPa @Strain 0.200 %, Temperature 24.0 °C	40000 psi @Strain 0.200 %, Temperature 75.2 °F	

	283 MPa @Strain 0.200 %, Temperature -28.0 °C	41000 psi @Strain 0.200 %, Temperature -18.4 °F	
	290 MPa @Strain 0.200 %, Temperature -80.0 °C	42100 psi @Strain 0.200 %, Temperature -112 °F	
	324 MPa @Strain 0.200 %, Temperature -196 °C	47000 psi @Strain 0.200 %, Temperature -321 °F	
Elongation at Break	17 % @Temperature -28.0 °C	17 % @Temperature -18.4 °F	
	17 % @Temperature 24.0 °C	17 % @Temperature 75.2 °F	
	18 % @Temperature -80.0 °C	18 % @Temperature -112 °F	
	18 % @Temperature 100 °C	18 % @Temperature 212 °F	
	20 % @Temperature 149 °C	20 % @Temperature 300 °F	
	22 % @Temperature -196 °C	22 % @Temperature -321 °F	
	28 % @Temperature 204 °C	28 % @Temperature 399 °F	
	60 % @Temperature 260 °C	60 % @Temperature 500 °F	
	85 % @Temperature 316 °C	85 % @Temperature 601 °F	
	95 % @Temperature 371 °C	95 % @Temperature 700 °F	
	12 % @Thickness 1.59 mm	12 % @Thickness 0.0625 in	AA; Typical
	17 % @Diameter 12.7 mm	17 % @Diameter 0.500 in	AA; Typical
Modulus of Elasticity	68.9 GPa	10000 ksi	AA; Typical; Average of tension and compression. Compression modulus is about 2% greater than tensile modulus.
Notched Tensile Strength	324 MPa	47000 psi	2.5 cm width x 0.16 cm thick side-notched specimen, K_t = 17.
Ultimate Bearing Strength	607 MPa	88000 psi	Edge distance/pin diameter = 2.0
Bearing Yield Strength	386 MPa	56000 psi	Edge distance/pin diameter = 2.0
Poissons Ratio	0.33	0.33	Estimated from trends in similar Al alloys.
Fatigue Strength	96.5 MPa @# of Cycles 5.00e+8	14000 psi @# of Cycles 5.00e+8	completely reversed stress; RR Moore machine/specimen
Fracture Toughness	29.0 MPa-m½	26.4 ksi-in½	K_{IC}; TL orientation.
Machinability	50 %	50 %	0-100 Scale of Aluminum Alloys
Shear Modulus	26.0 GPa	3770 ksi	Estimated from similar Al alloys.
Shear Strength	207 MPa	30000 psi	AA; Typical

Electrical Properties	**Metric**	**English**	**Comments**
Electrical Resistivity	0.00000399 ohm-cm @Temperature 20.0 °C	0.00000399 ohm-cm @Temperature 68.0 °F	AA; Typical

Thermal Properties	**Metric**	**English**	**Comments**
CTE, linear	23.6 µm/m-°C @Temperature 20.0 - 100 °C	13.1 µin/in-°F @Temperature 68.0 - 212 °F	AA; Typical; average over range
	25.2 µm/m-°C @Temperature 20.0 - 300 °C	14.0 µin/in-°F @Temperature 68.0 - 572 °F	
Specific Heat Capacity	0.896 J/g-°C	0.214 BTU/lb-°F	
Thermal Conductivity	167 W/m-K	1160 BTU-in/hr-ft²-°F	AA; Typical at 77°F
Melting Point	582 - 651.7 °C	1080 - 1205 °F	AA; Typical range based on typical composition for wrought products >= 1/4 in. thickness. Eutectic melting can be eliminated by homogenization.
Solidus	582 °C	1080 °F	AA; Typical
Liquidus	651.7 °C	1205 °F	AA; Typical

Processing Properties	**Metric**	**English**	**Comments**
Solution Temperature	529 °C	985 °F	
Aging Temperature	160 °C	320 °F	Rolled or drawn products; hold at temperature for 18 hr
	177 °C	350 °F	Extrusions or forgings; hold at temperature for 8 hr

Component Elements Properties	**Metric**	**English**	**Comments**
Aluminum, Al	95.8 - 98.6 %	95.8 - 98.6 %	As remainder
Chromium, Cr	0.04 - 0.35 %	0.04 - 0.35 %	

Copper, Cu	0.15 - 0.40 %	0.15 - 0.40 %	
Iron, Fe	<= 0.70 %	<= 0.70 %	
Magnesium, Mg	0.80 - 1.2 %	0.80 - 1.2 %	
Manganese, Mn	<= 0.15 %	<= 0.15 %	
Other, each	<= 0.05 %	<= 0.05 %	
Other, total	<= 0.15 %	<= 0.15 %	
Silicon, Si	0.40 - 0.80 %	0.40 - 0.80 %	
Titanium, Ti	<= 0.15 %	<= 0.15 %	
Zinc, Zn	<= 0.25 %	<= 0.25 %	

References for this datasheet.

**
This data sheet is not an active part of MatWeb and the information on it should not be considered reliable.
Inactive data sheets have usually been replaced with newer information on the same material. If this is the case, you can find the active data sheet by using any of our search tools, including the Quick Search box in the upper part of this page.
If you are unable to locate an active data sheet for this material, then this material is likely discontinued, although various other reasons may be behind its removal. In any event, do not rely on the information on this page to be accurate or maintained.
You may have reached this data sheet through an outdated bookmark or link. Please update your bookmark accordingly. We apologize if you have accessed this page through MatWeb's usual search tools.

Some of the values displayed above may have been converted from their original units and/or rounded in order to display the information in a consistent format. Users requiring more precise data for scientific or engineering calculations can click on the property value to see the original value as well as raw conversions to equivalent units. We advise that you only use the original value or one of its raw conversions in your calculations to minimize rounding error. We also ask that you refer to MatWeb's terms of use regarding this information. Click here to view all the property values for this datasheet as they were originally entered into MatWeb.